University of South Bohemia in České Budějovice

Faculty of Science

Biomolecular simulations in non-aqueous media

Ph.D. Thesis

Fatemeh Fadaei

Supervisor: Dr. Babak Minofar

České Budějovice 2023

This thesis should be cited as:

Fadaei, F., 2023: Biomolecular simulations in non-aqueous media. University of South Bohemia, Faculty of Science, České Budějovice, Czech Republic.

Annotation

The behavior of biomolecules is affected by solvation. In the solution, water, the most common solvent for biomolecules, surrounds and interacts with biomolecules. In consequence, water exerts influence on the structural stability, conformational flexibility, and functionality of the biomolecules. The interaction of water molecules with biomolecules could be altered by the addition of other components such as salts and co-solvents. Indeed, salts and co-solvents can directly or indirectly influence the behavior of biomolecules in the solution, which plays a crucial role in many applications.

During my Ph.D. study, the effect of different salts and co-solvents (ionic liquids and deep eutectic solvents) on the structural stability and activity of DNA and enzymes have been investigated by molecular dynamics simulations to understand the details of solvation processes at molecular levels. In addition, the effect of ions (Hofmeister series) on the structure, stability and, reactivity of biomolecules has been studied where these ions can be counter ions in the structure of ionic liquids. It should be mentioned that this thesis mainly focuses on understanding the behavior of biomolecules on hydrated ILs, which is completely related to the subject.

Declaration

I hereby declare that I am the author of this dissertation and that I have used only those sources and literature detailed in the list of references.

České Budějovice, date

.........03/03/2023.................................   .... Fatemeh Fadaei.........

                                                                        name and surename

………..…………

    signature

This thesis originated from a partnership of **Faculty of Science, University of South Bohemia**.

.

Přírodovědecká
fakulta
Faculty
of Science

Acknowledgments

Dedication

This thesis is dedicated to my loving husband, Mostafa, who has been a constant source of support and encouragement throughout my Ph.D. period and life. I would not be at this point in my life without his assistance. I am truly thankful for having him in my life. Also, I am dedicating this thesis to my parents, Mohammad Ali and Parvin Dookht, who have always loved me unconditionally and motivated me to work hard for the things that I would like to achieve. In addition, I am dedicating this thesis to my sister, Foroogh, and my brother, Mohammad Reza, as well as to my family-in-law who encouraged me to pursue my dreams and finish my dissertation.

List of papers and author's contribution

The thesis is based on the following papers (listed chronologically):

I. **Fadaei, F**., Tortora, M., Gessini, A., Masciovecchio, C., Catalini, S., Vigna, J., Mancini, I., Mele, A., Vacek, J., Reha, D. and Minofar, B., 2022. Structural specificity of groove binding mechanism between imidazolium-based ionic liquids and DNA revealed by synchrotron-UV Resonance Raman spectroscopy and molecular dynamics simulations. *Journal of Molecular Liquids*, *347*, p.118350. (IF=6.633). Her contribution was performing all computational parts of the project with 80. %. involvement

II. **Fadaei, F**., Seifert, M., Raymond, J.R., Řeha, D., Kulik, N., Minofar, B. and Heitz, M.P., 2022. Interactions between a dsDNA Oligonucleotide and Imidazolium Chloride Ionic Liquids: Effect of Alkyl Chain Length, Part I. *Molecules*, *27*(1), p.116. (IF=4.927). Her contribution was performing all computational parts of the project with 80 %. involvement

III. Zara, Z., Mishra, D., Pandey, S.K., Csefalvay, E., **Fadaei, F**., Minofar, B. and Řeha, D., 2022. Surface Interaction of Ionic Liquids: Stabilization of Polyethylene Terephthalate-Degrading Enzymes in Solution. *Molecules*, *27*(1), p.119. (IF=4.927). Her contribution was performing some analysis of the computational parts with 10 % involvement.

Co-author agreement

Dr. Babak Minofar, the supervisor of this Ph.D. thesis and co-author of the following papers [1-3], fully acknowledges the stated contribution of „Fatemeh Fadaei" to these manuscripts.

MINOFAR

....

Name Dr. Babak Minofar

The papers:

1. **Fadaei, F**., Tortora, M., Gessini, A., Masciovecchio, C., Catalini, S., Vigna, J., Mancini, I., Mele, A., Vacek, J., Reha, D. and Minofar, B., 2022. Structural specificity of groove binding mechanism between imidazolium-based ionic liquids and DNA revealed by synchrotron-UV Resonance Raman spectroscopy and molecular dynamics simulations. *Journal of Molecular Liquids*, *347*, p.118350. (IF=6.633).
2. **Fadaei, F**., Seifert, M., Raymond, J.R., Řeha, D., Kulik, N., Minofar, B. and Heitz, M.P., 2022. Interactions between a dsDNA Oligonucleotide and Imidazolium Chloride Ionic Liquids: Effect of Alkyl Chain Length, Part I. *Molecules*, *27*(1), p.116. (IF=4.927).
3. Zara, Z., Mishra, D., Pandey, S.K., Csefalvay, E., **Fadaei, F**., Minofar, B. and Řeha, D., 2022. Surface Interaction of Ionic Liquids: Stabilization of Polyethylene Terephthalate-Degrading Enzymes in Solution. *Molecules*, *27*(1), p.119. (IF=4.927).

Contents

List of abbreviations:

A	Adenine
AAILs	Amino Acids Ionic Liquids
AILs	Aprotic Ionic Liquids
AMBER	Assisted Model Building and Energy Refinement
C	Cytosine
CD	Circular Dichroism
CHARMM	Chemistry at HARvard Macromolecular Mechanics
DES	Deep Eutectic Solvent
DNA	Deoxyribonucleic acid
FCS	Fluorescence Correlation Spectroscopy
FDH	Formate DeHydrogenases
G	Gguanine
GAFF	Generalized Amber Force Field
GROMACS	GROningen Machine for Chemical Simulations
HBD	Hydrogen Bond Donor
HLDs	Haloalkane Dehalogenases
HRV	Human rhinovirus
ILs	Ionic Liquids
IR	Infrared
LINCS	linear constraint solver
LJ	Lennard-Jones
MD	Molecular Dynamics
MILs	Magnetic Ionic Liquids
OPLS	Optimized Potential for Liquid Simulations
PBC	Periodic Boundary Conditions
PILs	Protic Ionic Liquids
RDF	Radial Distribution Function
RMSD	Root Mean Square Deviation
RMSF	Root Mean Square Fluctuation
T	Thymine
VMD	Visual Molecular Dynamics

List of figures:

CHAPTER 1

General introduction

1. Motivation

The behavior of biomolecules is affected by solvation. In the solution, water, the most common solvent for biomolecules, surrounds and interacts with biomolecules. In consequence, water exerts influence on the structural stability, conformational flexibility, and functionality of the biomolecules [1]. The interaction of water molecules with biomolecules could be altered by the addition of other components such as salts and co-solvents. Indeed, salts and co-solvents can directly (binding to the proteins) or indirectly (changing the water network) influence the behavior of biomolecules.

Hofmeister studied for the first time the effect of salts on the solvent–protein interactions, and his findings are summarized in the Hofmeister series [2]. The Hofmeister series is characterized by the kosmotropic or chaotropic properties of the ions. As is known, the effect of anions is more obvious than that of cations in the series, and the position of cations in the series can be changed in different phenomena. Kosmotropic anions are known for being well-hydrated, and water structure makers tend to stabilize the native fold structure of proteins, resulting in salting-out behavior. However, chaotropic anions are poorly hydrated, and water structure breakers tend to facilitate protein denaturation and unfolding, leading to salting-in behavior [3, 4].

In the past years, several studies have been conducted to investigate the effect of salts on the structure, function, and properties of biomolecules. For instance, Dušekova and coworkers [5] used absorbance and circular dichroism (CD) spectroscopies to study the effect of Hofmeister sodium salts, sulfate, chloride, bromide, and perchlorate on the catalytic properties and stability of chymotrypsin. According to their results, the direct interaction of anions with protein surfaces leads to modulating enzyme properties. In another study, Garajová and coworkers [6] investigated the enzymatic activity and stability of lysozyme in the presence of salts by fluorescence spectroscopy and differential scanning calorimetry, respectively. Their results showed that lysozyme has different properties depending on the anion concentration and its position in the Hofmeister series. Based on their results, sulfate, and acetate anions (kosmotropic anions) increased stability and activated the enzyme, while bromide, thiocyanate, and perchlorate anions (chaotropic anions) decreased stability and inhibited the enzyme's activity. In another work, the

Hofmeister effects of a range of cations and anions on protein thermal stability were explored by Sedlak et al. [7]. They suggested that the direct interactions between ions and the protein are responsible for the Hofmeister effects of the ions on protein stability.

Apart from organic and inorganic solvents, a new category of solvents called ionic liquids (ILs) has been recently considered as co-solvents for biomolecules. In the last decade, several studies were conducted to determine the role of ILs on the biomolecules' properties in the solutions. It should be mentioned that the addition of ILs strengthens the stability of some proteins, whereas the same ILs weaken the stability of other proteins [8]. It is worth mentioning that ILs are often employed to stabilize biomolecules, though the bimolecular interactions of their stabilization-destabilization are still a hot topic of research. For instance, Micaêlo et al. [9] used molecular dynamics (MD) simulation to study the behavior of the serine protease cutinase from *Fusarium solani* pisi, in the presence of two different ILs (1-butyl-3-methylimidazolium hexafluorophosphate and 1-butyl-3-methylimidazolium nitrate). They considered the enzyme structure to be highly dependent on the amount of water present in the IL medium. 1-Butyl-3-methylimidazolium hexafluorophosphate had a significant influence on the stability of the protein. Their analysis also indicates that the ILs "strip off" most of the water from the enzyme surface. In another paper, Ghosh et al. [10] used fluorescence correlation spectroscopy (FCS) and MD simulation to understand the effect of 1-propyl-3-methylimidazolium bromide ([PMIM]Br) on the structure and dynamics of lysozyme. Their experimental work showed that the addition of the [PMIM][Br] results in a reduction in size and faster conformational dynamics of the protein, and the MD simulation results indicated that the addition of room temperature IL caused the replacement of interfacial water by the [PMIM]$^+$ cation from the first solvation layer of the protein, providing a comparatively dehydrated environment. In another study, fluorescence and CD spectroscopic studies were done to investigate the structural stability of heme proteins such as myoglobin and hemoglobin in a series of ammonium-based ILs (tetramethyl ammonium hydroxide [(CH$_3$)$_4$N]$^+$[OH]$^-$ (TMAH), tetraethyl ammonium hydroxide [(C$_2$H$_5$)$_4$N]$^+$[OH]$^-$ (TEAH), tetrapropyl ammonium hydroxide [(C$_3$H$_7$)$_4$N]$^+$[OH]$^-$ (TPAH) and tetrabutyl ammonium hydroxide [(C$_4$H$_9$)$_4$N]$^+$[OH]$^-$ (TBAH) [8]. the experimental results showed that less viscous ILs carrying smaller alkyl chains destabilize the heme proteins as compared to ILs carrying bulkier alkyl chains, which are more viscous ILs. Hence, the addition of these ILs to the heme proteins decreased their thermal stability and caused the protein to be in an unfolded state at lower

temperatures. Ajloo et al. [11] described the influence of 1-allyl 3-methyl-imidazolium and 1-octhyl 3-methyl-imidozolium chlorides on the structure and activity of adenosine deaminase. Their results illustrated that the inhibition of activity and reduction of enzyme tertiary structure is more for octhyl than allyl derivative because of its more hydrophobic property. In addition, their results showed that ILs reduce intermolecular hydrogen bonds and unfold enzyme structure. In another work, D'Oronzo et al. [12] experimentally and theoretically investigated the effect of the ILs/water mixture on the activity of wild type and a more thermally and chemically stable mutant (SM4) of a specific formate dehydrogenases (PseFDH). The selected ILs were [Mmim][Me$_2$PO$_4$], [Bmim][Br], [Bmim][CH$_3$SO$_3$], [Bmim][BF$_4$], [Bmim][AcO]. According to their results, the activity of the SM4 FDH increased (up to 42 %) at low concentrations (optimally 2.5 %) of some selected ILs.

It should be noted that the number of studies that explore the influence of ILs on the structure and function of proteins is greater than the number of studies that investigate the characteristics of DNA dissolved in pure or aqueous ILs solutions. Jumbri et. al. [13] used both computational and experimental techniques to explore the characteristics and influence of ILs on the structural properties of DNA. According to their report, DNA solvated by ILs preserved its duplex conformation at different temperatures up to 373.15 K. The. Also, they concluded that stronger hydration shells destabilize the DNA due to the reduction of the binding ability of ILs' cations to the DNA phosphate group. In another study, the interaction of DNA with a morpholinium-based IL was explored by Pabbathi et al. [14] by employing FCS, conventional steady-state and time-resolved fluorescence, CD, and molecular docking techniques. Their results showed the high thermal stability of DNA in the presence of morpholinium-based IL.

Furthermore, a new type of solvent, called the deep eutectic solvent (DES), was developed by Abbott and co-workers [15] and has attracted considerable attention owing to its special properties. Some DESs are eutectic mixtures that consist of an ammonium salt and a hydrogen-bond donor (HBD). DES shares many characteristics with ILs, though DES components are frequently less expensive and biodegradable [16]. Some studies have used DESs as media for biomolecules. For instance, Stepankova's group [17] compared the performance of three haloalkane dehalogenases (HLDs), catalyzed the hydrolytic cleavage of carbon-halogen bonds in diverse halogenated hydrocarbons, in aqueous solutions of the DES ethaline (its components ethylene glycol and

choline chloride) and two organic solvents, including methanol and acetone. They found out that each of the solvents had various impacts on the activity of each enzyme. In addition, their results showed that ethylene glycol and an ethylene glycol-based DES can have a positive impact on catalysis by haloalkane dehalogenases, broadening their usability in "green" biotechnologies. Huang et al. [18] studied the effect of 24 DESs on enzymatic performance. Their results revealed that DESs are viable solvents or co-solvents for lipase-catalyzed reactions, and both the activity and stability of the lipase are affected by the choice of DES components (salts and HBDs) and their molar ratios.

As mentioned above, various experimental methods, analytical techniques, and computational methods can be used to study the structure, dynamics, stability, and function of biomolecules in non-aqueous media. It is worth mentioning that among these methods, computer simulations can provide a deep understanding of the effects of non-aqueous solutions on the solvation structure and dynamics of biomolecules such as enzymes and DNA, where experimental studies might be difficult or impossible to perform. Among the various simulation techniques, MD simulation is one of the most powerful tools for understanding the details of solvation processes at molecular levels.

In my Ph.D. study, the effect of ILs [19,20,21], Hofmeister series [22, 23], and DES on the structural stability and activity of DNA and enzymes have been investigated by MD simulation to better understand the impact of different solvent media on the structural changes and binding properties of DNA and enzymes. As mentioned earlier, there are numerous publications on protein behavior and function in ionic liquid systems, but the literature on DNA stabilization in ionic liquid systems is limited [24]. This thesis mainly focuses on understanding the behavior of DNA in hydrated ILs, which is necessary for developing DNA material and better utilizing DNA in nanotechnology.

2. Molecular Dynamics Simulation

In the late 1950s, the first MD simulations of simple gasses were performed by Alder and Wainwright [25]. In the late 1970s, the first MD simulation of a protein was done [26,27]. Over

the past years, MD simulations have become substantially more popular in experimental structural biology papers, where they are employed to interpret and explain the atomic details of experimental results and to guide experimental work.

MD simulations use Newton's equations of motion for the individual particles (atoms, molecules, ions, etc.). Specifically, integrating Newton's laws of motion generates successive configurations of the system, resulting in a trajectory that specifies how the positions and velocities of the particles in the system change over time [28]. In fact, by solving the differential equations embodied in Newton's second law (f = ma), the trajectory is obtained by Eq. (1):

$$\frac{d^2x_i}{dt^2} = \frac{F_{x_i}}{m_i} \qquad\qquad i = 1\ldots N \qquad\qquad (1)$$

This equation is for a system of N interacting atoms and describes the motion of a particle of mass m_i along one coordinate (x_i) with f_{x_i} being the force on the particle in that direction [28].

There are some algorithms for integrating equations of motion. One method for integrating equations of motion in MD simulation is the velocity Verlet algorithm [29]. In the velocity Verlet algorithm, positions r and velocities v at time t are applied to integrate the equations of motion. It should be mentioned that velocities at the previous half step are not required in this algorithm (Eq. 2-4) [30].

$$v\left(t + \frac{1}{2}\Delta t\right) = v(t) + \frac{\Delta t}{2m}F(t) \qquad\qquad (2)$$

$$r(t + \Delta t) = r(t) + \Delta t\, v\left(t + \frac{1}{2}\Delta t\right) \qquad\qquad (3)$$

$$v(t + \Delta t) = v\left(t + \frac{1}{2}\Delta t\right) + \frac{\Delta t}{2m}F(t + \Delta t) \qquad\qquad (4)$$

Another algorithm for integrating equations of motion is the leap-frog algorithm [31]. In the algorithm, r and v are leaping like frogs over each other's backs (Figure 1). As a result, it is known as the leap-frog [30].
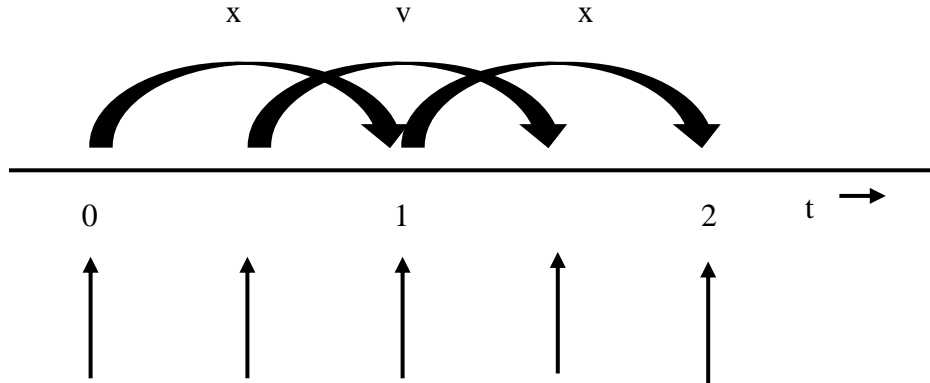

Figure 1: The Leap-Frog integration method [30].

This algorithm is made of two steps. In this algorithm, first, the velocities are measured at time $\left(t + \frac{1}{2}\Delta t\right)$. Then, this velocity is considered as an initial velocity and can be used to calculate the positions, r, at the time (r + Δt) (Eq. 5 and 6) [30, 32].

$$v\left(t + \frac{1}{2}\Delta t\right) = v\left(t - \frac{1}{2}\Delta t\right) + \frac{\Delta t}{m}F(t) \tag{5}$$

$$r(t + \Delta t) = r(t) + \Delta t v(t + \frac{1}{2}\Delta t) \tag{6}$$

It is important to note that it is necessary to establish an initial configuration of the system. The initial configuration may be obtained from experimental data, from a theoretical model, or from a combination of the two. Also, the initial velocity of the atoms must be assigned, which can be done by randomly selecting from a Maxwell-Boltzmann distribution at the temperature of interest (Eq. 7) [28].

$$p(v_{ix}) = \left(\frac{m_i}{2\pi k_B T}\right)^{1/2} \exp\left[-\frac{1}{2}\frac{m_i v_{ix}^2}{k_B T}\right] \tag{7}$$

The Maxwell-Boltzmann equation provides the probability that an atom i at mass m_i has a velocity v_{ix} in the x direction at the temperature T. It should be pointed out that the Maxwell-Boltzmann distribution is a Gaussian distribution, which can be obtained using a random number generator.

In MD simulations, the negative derivative of the potential energy called the force field allows for calculating the forces acting on each atom (Eq. 8). Force fields are parametrized using physical data from x-ray crystallography, infrared (IR), and Raman spectroscopy, and high-level quantum mechanical calculations with model compounds [33].

$$F_i = -\frac{\delta V}{\delta r_i} \tag{8}$$

The potential energy (V) can be calculated as bonded potential energy and non-bonded potential energy [34]. The bonded potential energy represents the interaction of bonded atoms, and it is divided into three types: valence angle potential, bond potential, and torsion (dihedral) angle potential. The non-bonded potential energy represents non-bonded interactions between atoms and is divided into two components: Lennard-Jones interaction energy, which reflects the van der Waals interaction between atoms, and Columbic interaction energy, which represents electrostatic charges (Eq. 9).

$$\begin{aligned}
V(r)^N = &\sum_{all\ bonds} k_l(l-l_0)^2 + \sum_{all\ angles} k_\theta\ (\theta - \theta_0)^2 \\
&+ \sum_{all\ torsions} \frac{1}{2}V_n[1 + \cos(n\omega - \gamma)] \\
&+ \sum_{j=1}^{N} \sum_{i=j+1}^{N} \left\{\varepsilon_{ij}\left[\left(\frac{r_{0ij}}{r_{ij}}\right)^{12} - 2\left(\frac{r_{0ij}}{r_{ij}}\right)^{6}\right] + \frac{q_j q_i}{4\pi\varepsilon_0 r_{ij}}\right\}
\end{aligned} \tag{9}$$

Where l is the stretching of bonds, θ is the bending of valence angles and ω is the rotation of torsional angles (Figure 2) and, k_l, k_θ and V_n are force constants. The torsion term illustrates a periodic rotation of a dihedral angle with periodicity n and phase γ. In the non-bonded energy, the

parameter ε is related to the well-depth of the Lennard-Jones (LJ) potential, and r is the distance at which the LJ potential has its minimum. q is the partial atomic charge, ε_0 is the vacuum permittivity, and r_{ij} is the distance between atoms i and j [34].
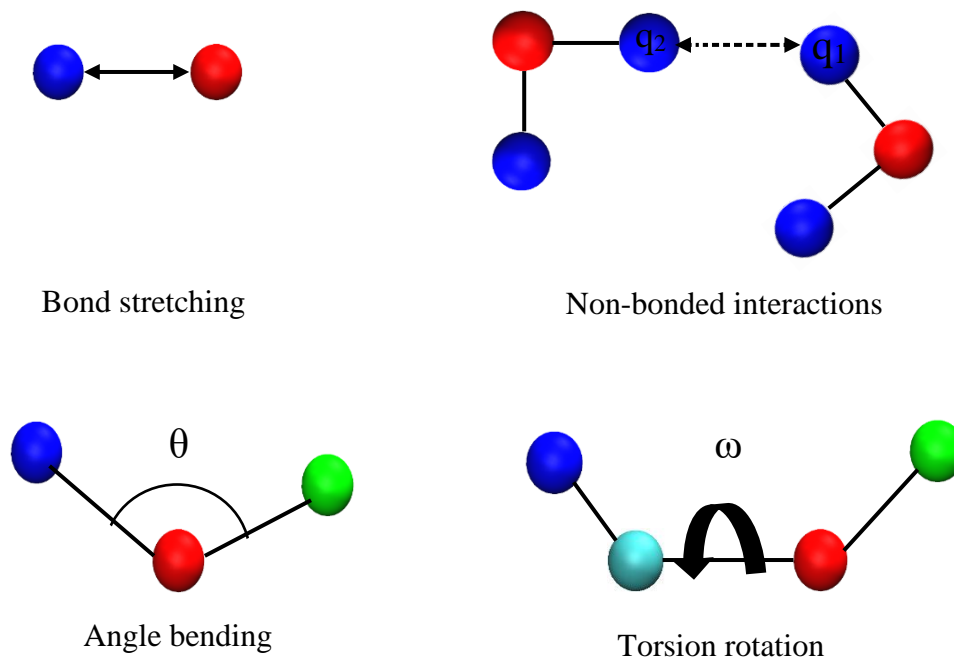

Figure 2: Graphic illustrations of energy terms described in the force-field terms.

It is worth noting that force fields have different degrees of complexity and can be used for different kinds of systems. For instance, AMBER (Assisted Model Building and Energy Refinement) [35,36,37] is suitable for the simulation of biomolecules. CHARMM (Chemistry at HARvard Macromolecular Mechanics) [38] is another force field that it primarily targets biological systems, including proteins, small molecule ligands, lipids, etc., as they occur in solution, crystals, and membrane environments. The next one is the OPLS (Optimized Potential for Liquid Simulations) force field [39] used to simulate condensed matters. GAFF (Generalized Amber Force Field) [40] is another AMBER-compatible force field designed to simulate small compounds and biomolecules [34].

It should be mentioned that the fastest motion in the simulation system limits the time step (typical value of 1 fs for atomistic simulation). In other words, the smallest oscillation period found in the

system limits the maximum time step in MD simulations. As the bond stretching vibrations are in their quantum-mechanical ground state, it is better to be represented by a constraint instead of a harmonic potential [30]. The time step can be increased by replacing the bond vibrations with holonomic constraints [41]. In fact, constraints are utilized to maintain bonds at constant lengths, which results in an increase in the time step of integration. In the MD simulation, a larger time step (typically 2 fs) can be used by restraining bonds lengths using constraint algorithms like SHAKE [42] and linear constraint solver (LINCE) [41].

It is worth noting that depending on the properties of the system, the timescale of MD simulations is different. Molecular mechanics, the method of choice for computational studies of biomolecular systems, makes it possible to implement MD simulations on biological systems that have tens of thousands to hundreds of thousands atoms for simulation times from nanoseconds to microseconds [43].

The general MD algorithm is shown in Figure 3. According to the algorithm, the following steps are carried out:

1) Input initial conditions. In the first step, all-atom positions r and velocities v, as well as potential interaction V as a function of atom positions, are included.

2) Compute forces. The force on any atom is measured by calculating the force between non-bonded atom pairs and the forces due to bonded interactions.

3) Update configuration. In this step, Newton's equations of motion are numerically solved, and the acceleration and velocity of each atom are obtained (Eq. 10 and 11). Hence, the movement of the atoms is simulated.

$$\frac{dv_i}{dt} = \frac{F_i}{m_i} \tag{10}$$

$$\frac{dr_i}{dt} = v_i \tag{11}$$

4) Output step (if required). The positions, velocities, energies, temperature, pressure, etc. are written.

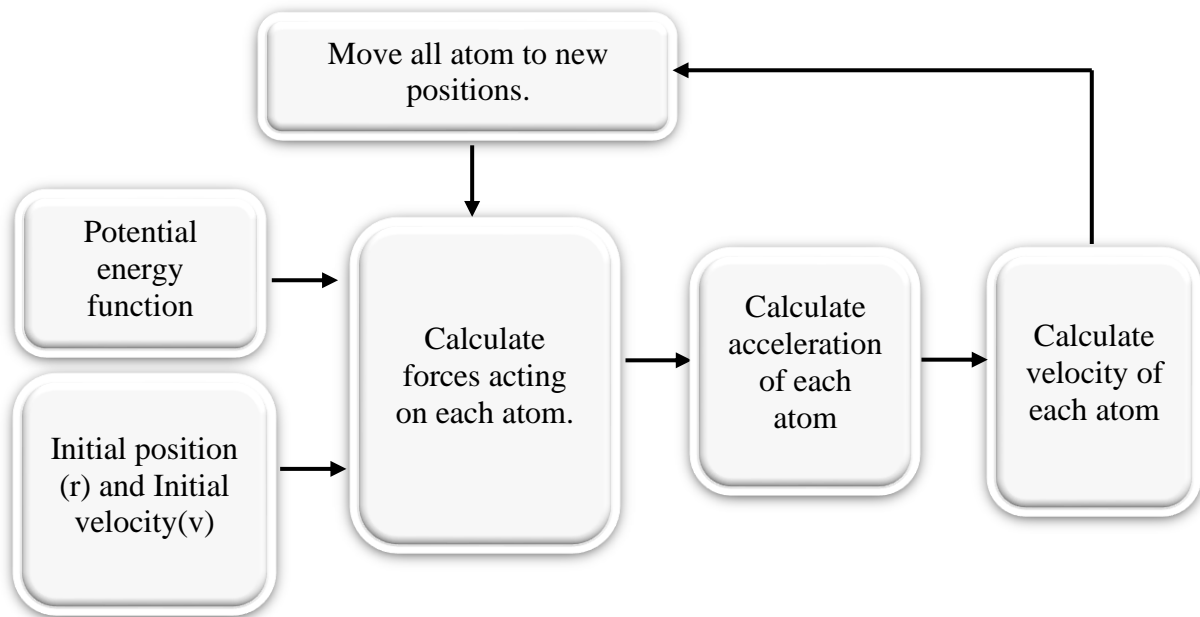Steps 2, 3, and 4 are repeated if it is required.

Figure 3: The flow chart of a MD simulation program.

2.1. Periodic Boundary Condition

Essentially all molecular dynamics simulations use periodic boundary conditions (PBC). The PBC enables the simulation of a very large system with a relatively small number of particles without the perturbing effect of hard walls [44]. In PBC, the primary cell is replicated in all directions, yielding an infinite lattice. During the simulation, when a molecule moves in the original box, its periodic image in each of the nearby boxes moves in exactly the same way. In other words, if an atom leaves the central box, it's images enter the central box from the other side and the number of atoms in the central box is conserved [45]. Figure 4 illustrates a two-dimensional version of such a periodic system.
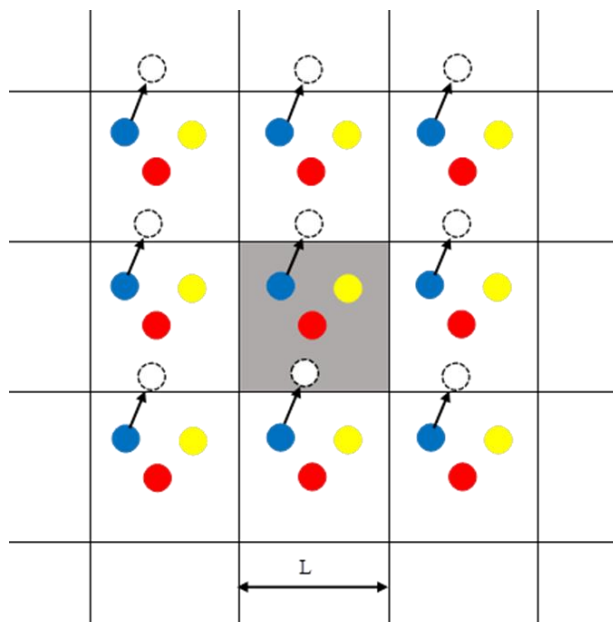
Figure 4: A two-dimensional periodic system. Molecules can enter and leave each box across each of the four edges [45].

It should be mentioned that the most important part of the MD program is the calculation of the forces acting on all molecules. In order to calculate the force on a particular molecule or those contributions to the potential energy involving the particular molecule, all interactions between the particular molecule and images in other cells lying in the surrounding boxes must be included. In detail, for N atoms in the central box, there are N^2 interactions. It is computationally too demanding and impossible to calculate in practice. Hence, this summation is restricted by making an approximation for a short-range potential energy function. In detail, a particular molecule at the center of a region that has the same size and shape as the basic simulation box interacts with all the molecules whose centers lie within this region that is, with the closest periodic images of the other N - 1 molecules (Figure 5). That is called the 'minimum image convention. As there may still be a very substantial calculation for a system of (say) 1000 particles in the minimum image convention. A further approximation can significantly improve the situation. Hence, a spherical cutoff is normally applied for short-range forces [45]. The circle in Fig. 4 shows a cutoff. Only interactions for $r \leq \frac{L}{2}$ contribute to the forces acting on the molecules and interactions for $r \geq \frac{L}{2}$ ignored. In this case, the number of interactions that need to be evaluated is reduced.
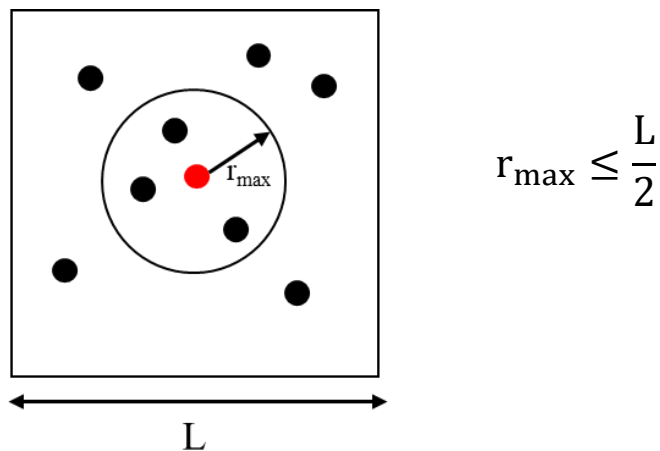
$$r_{max} \leq \frac{L}{2}$$

Figure 5: The minimum image convention in a two-dimensional system. The central 'box' constructed with a particular molecule at its center and nine molecules. The circle represents the cutoff.

2.2. Statistical Ensembles

A system's macroscopic state is characterized by macroscopic parameters such as temperature (T), pressure (P), and volume (V). An ensemble notion is created to relate the dynamics of particles characterized by their microscopic qualities to the overall macroscopic attributes of the system. Statistical ensembles enable calculations to be performed at constant values of virtually any of the thermodynamic control variables [46]. There are several types of ensembles with specific properties. For instance, the microcanonical NVE ensemble holds a fixed number of particles, the volume (V), and the energy (E). Another ensemble is the canonical NVT ensemble, in which volume is fixed and temperature is held constant by using various thermostats. The next example is the isobaric-isothermal NPT ensemble. In the NPT ensemble, the volume of the system can fluctuate, and pressure and temperature are maintained constant by using different barostats and thermostats.

The goal of a thermostat is to ensure that the average temperature of a system is correct. In simulations, the "instantaneous (kinetic) temperature" is usually measured by the kinetic energy of the system using the equipartition theorem. In fact, the temperature is measured using the system's total kinetic energy [30]. There are different thermostats including the Berendsen thermostat [47], the Andersen thermostat [48], the Nosé-Hoover thermostat [49,50], or a velocity

rescaling scheme [51]. These thermostats have parameters that affect the speed to control the temperature of the environment and enable the system to take to relax to the target temperature. Similarly, to temperature coupling, the system can also be coupled to a pressure bath. Hence, the algorithm (the Berendsen barostat [47], Parrinello-Rahman barostat [52, 53], the Martyna-Tuckerman-Tobias-Klein barostat [54]) is used to stabilize the pressure (and thus also the density) of the system.

2.3. Software and Steps

In this study, the GROMACS (GROningen Machine for Chemical Simulations) program package [30,55 ,56, 49, 57, 58,59] was used for performing MD simulations [55,60, 61, 62]. VMD (visual molecular dynamics) software is used for the visualization and analysis of molecular dynamics trajectories [63].

Several steps must be taken to do an MD simulation of a biomolecule in GROMACS (Figure 6). First, the structure of the biomolecule is prepared by downloading it from databases (like the Protein Data Bank [64, 65] or homology modeling. After preparing the structure, the topology for the molecule is generated. It should be mentioned that all the information required to define the molecule inside a simulation is contained in the topology file. This contains both nonbonded parameters (atom types and charges) and bonded parameters (bonds, angles, and dihedrals). In this step, the force field will be written to the topology file. It must be noted each force field should be read completely and decide which is most applicable to the situation. Then, the box is generated. the protein must be centered in the box and placed at least 1.0 nm from the box edge. The distance to the edge of the box is an important factor. As mentioned earlier, the periodic boundary conditions are used in most MD simulations, and the sufficient distance between any two periodic images of a protein must be satisfied. In other words, a protein should never view its periodic image; otherwise, the forces measured will be spurious. In this step, the type and size of the box used in the simulation are also determined. There are different types of boxes (triclinic, cubic, dodecahedron, and octahedron) in the GROMACS program package. In the next step, depending on the system, a water model (SPC, SPC/E, TIP3P, and TIP4P) will be chosen and the box will be filled with water. These models are different in structural features and parameters such as partial

14

charges [66,67]. After that, ions will be added to the system to neutralize the net charge on the protein. In this step, genion module replaces water molecules with the ions that the user specifies. Before beginning dynamics, the structure will be relaxed through a process called energy minimization to ensure that the system has no steric clashes or inappropriate geometry. In fact, energy minimization confirms that the initial structure is appropriate in terms of geometry and solvent orientation. It is important to note that the potential energy printed at the end of the energy minimization process should be negative to determine whether the energy minimization was successful. To begin real dynamics, the equilibration of the solvent and ions around the biomolecule must be done. Equilibration is often performed in two phases. We first arrive at the correct temperature based on kinetic energies. Then pressure will be applied to the system until it reaches the proper density. The first phase is done under an NVT ensemble (constant Number of particles, Volume, and Temperature). In order to analyze the temperature progression, the energy module can be used. From the resulting plot, if the system's temperature remains steady for the duration of the equilibration, it signifies that it has reached the desired value (300 K). The second phase is conducted under an NPT ensemble (constant Number of particles, Pressure, and Temperature). Again, the energy module can be used to investigate the pressure progression. The resulting plots can be used to illustrate the average pressure fluctuation value and the average density during equilibration. The stability of values over time shows that the system is well-equilibrated with respect to pressure and density. The time required for such procedures is dependent on the system's contents; normally, 50-100 ps should be sufficient. After the equilibration of the system at the desired temperature and pressure, an MD simulation can be run for data collection. The length of time required for the MD simulation depends on the system. Some approximations like using bond constraints are employed to run simulations between 50 and 100 ns [68]. Thereafter, depending on what types of data are required, some analysis on the system will be performed [30].
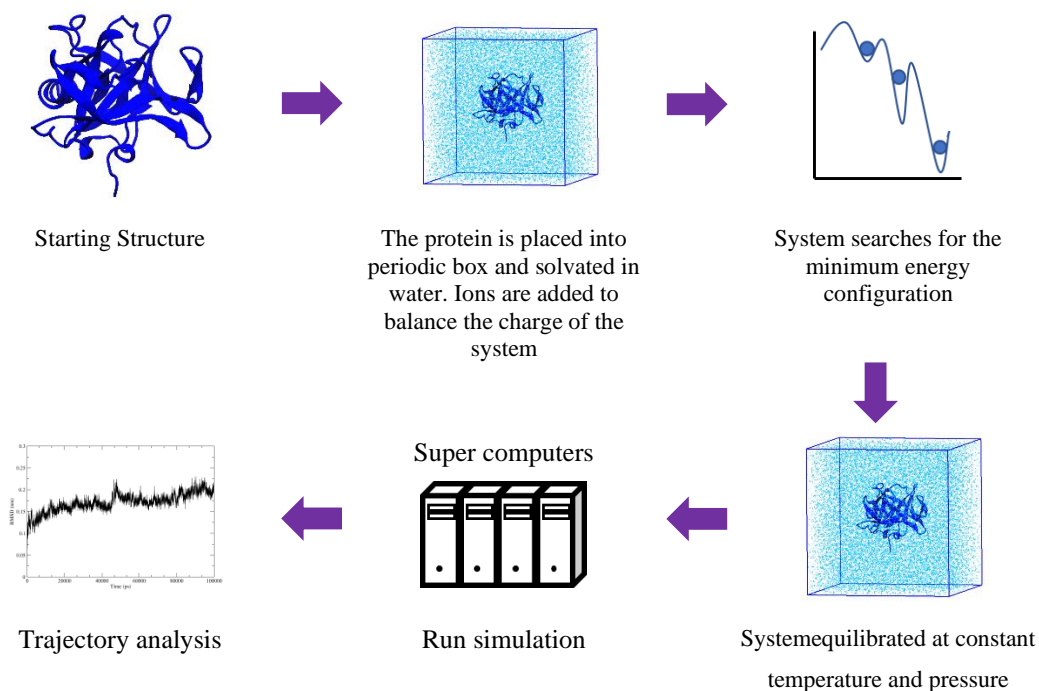
Figure 6: Molecular dynamics simulation process

2.4. Analyzing MD Simulations

After the simulation, some strategies based on the type of simulated system are implemented to extract relevant information about the system. Some of the most common methods used to analyze solute/solvent interactions are the radial distribution function (RDF), root mean square deviation (RMSD), and root mean square fluctuation (RMSF) [34], to mention but a few.

The RDF, g(r), defines the probability of finding a particle at a distance r from another tagged particle. The RDF is used to describe the distribution of solvent molecules around one specific molecule or atom. RDF can be calculated according to Eq. (11):

$$g(r) = \frac{1}{\rho N} \langle \sum_i \sum_j \delta[r - r_{ij}] \rangle \qquad (11)$$

16

Where N is the total number of atoms, $\rho = N/V$ is the number density, r_{ij} is the distance between atoms i and j, and the brackets indicate the ensemble average.

It must be noted that the analysis of structural mobility in molecular dynamics plays a vital role in data interpretation in the simulation of biomolecules. RMSD and RMSF are the most common measures of structural fluctuations, which are associated with biological function [69].

The RMSD is the average displacement of the atoms at a given moment of the simulation relative to a reference structure, which is either the first frame of the simulation or the crystallographic structure. The RMSD is computed to show the deviations of the backbone atoms of proteins from their initial structure and represents how structures and parts of structures alter over time as compared to the starting point. The RMSD is plotted vs. time, and monitoring the RMSD of the protein can provide insights into the structural conformations throughout the simulation. A flattening of the RMSD curve illustrates that the protein has equilibrated. The RMSD can be calculated according to Eq. (12):

$$\text{RMSD} = \sqrt{\frac{1}{N} \sum_{N} (r_i(t_0) - r_i(t))^2} \tag{12}$$

Where N is the number of atoms, and **r** (t) is the position of atom i, at time t.

Additionally, the RMSF computes the fluctuations of each subset of the structure (atom or residue) relative to the average structure of the simulation. Indeed, the RMSF measures the average deviation of a particle over time from a reference position. RMSF per residue is plotted vs. residue number and shows which residue in a protein leads the molecular motion and how much the residue moves and fluctuates during the simulation. The RMSF can be calculated according to Eq. (13):

$$\text{RMSF} = \frac{1}{T} \sum_T (r(t) - \bar{r})^2 \qquad\qquad (13)$$

Where T is the total time of the simulation and $\bar{r}$ is the average position.

3. Biomolecules

During my PhD program, MD simulations were implemented to investigate the solvation effects of salts and co-solvents on the behavior of biomolecules such as DNA, peptides, proteins, and enzymes in the aqueous solutions.

3.1. Deoxyribonucleic acid

Over the past 30 years, deoxyribonucleic acid (DNA) has been recognized as a versatile molecule in the field of nanotechnology. DNA is a good candidate for the construction of novel nanomaterials due to its unique features, including its miniature scale, sequence programmability, geometric properties, rigidity, and highly specific molecular recognition [70,71]. DNA nanotechnology, for example, can be utilized in biophysical techniques to enable single-molecule observations in biology [72]. Furthermore, DNA nanostructures can be used in the area of drug delivery due to their capacity to be programmed to any size, shape, and ligand patterning. They are also dynamic, allowing us to tailor their drug release to specific biological cues [72]. Since there is a great interest in the usage of DNA as an advanced material, understanding the structure and investigating the function of DNA in different media is important.

The DNA molecule is considered a polynucleotide or a polymer chain [73]. DNA is composed of four different types of nucleotide subunits. A nucleotide is composed of a sugar with five carbons, the phosphate group, and a nitrogen-containing base. The base can be either adenine (A), thymine (T), guanine (G), or cytosine (C). Sugars and phosphates link nucleotides covalently together in a chain. It should be noted that the nucleobases of the two strains follow base-pairing rules and form hydrogen bonds. In DNA, a bulkier two-ring base named purine is paired with a single-ring base

called a pyrimidine. In detail, G always pairs with C, and A with T (Figure 7) [74]. It is noteworthy that AT-rich DNA regions play an important role in molecular processes. In fact, AT-rich regions separate functional domains in eukaryotic DNA [75]. For instance, the yeast genome with long AT-rich sequences tends to be clustered [75]. In another example, 80.6% of the genome of the parasite Plasmodium falciparum, the causative agent of severe human malaria, is made up of A+T [76, 77].

The structure of the DNA molecule can vary depending on the base sequence and environment [78]. The right-handed double helical structure of the DNA, which was proposed by Watson and Crick in 1953, is the most commonly known DNA structure [73, 79]. Two linear sugar-phosphate backbones circling each other create two grooves in the double helix. Where the backbones are close together, minor grooves are generated, and where the backbones are far apart, major grooves are generated. Figure 7B shows two different grooves.

It should be mentioned that the B form of DNA is stable in water. However, DNA is not stable in an aqueous medium at room temperature for a long period of time. In detail, the stability of the DNA is mainly dependent on the water content, or more specifically, the properties of the hydration shells around the DNA. The hydration shells play a vital role in stabilizing or destabilizing DNA, and its conformational dynamics [13]. Furthermore, due to its large dependency on electrostatic interactions; DNA undergoes denaturation upon changing the pH, temperature, and ionic strength [24]. Hence, choosing a suitable medium for DNA extraction, purification, and storage is a key factor in biological experiments.

It must be made clear that the DNA melting temperature (Tm) value shows the stability of the double-helical structure of DNA in the solution. Hence, the Tm method can be used to investigate the impact of solution conditions, including buffers, pH, hydrophobicity, solutes, and analytes, on the stability of the double-helical structure of DNA in the solution [24].
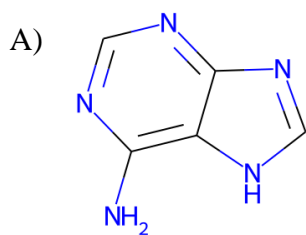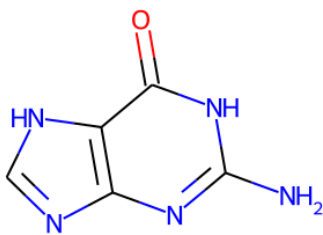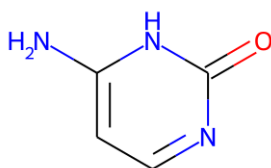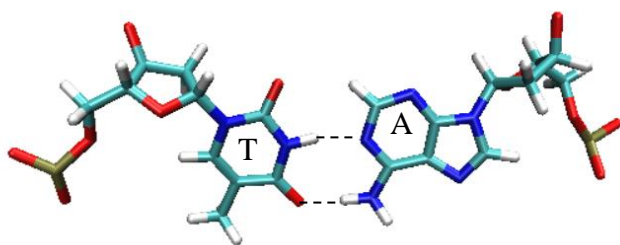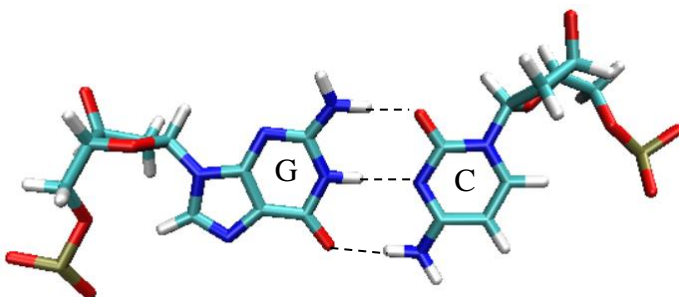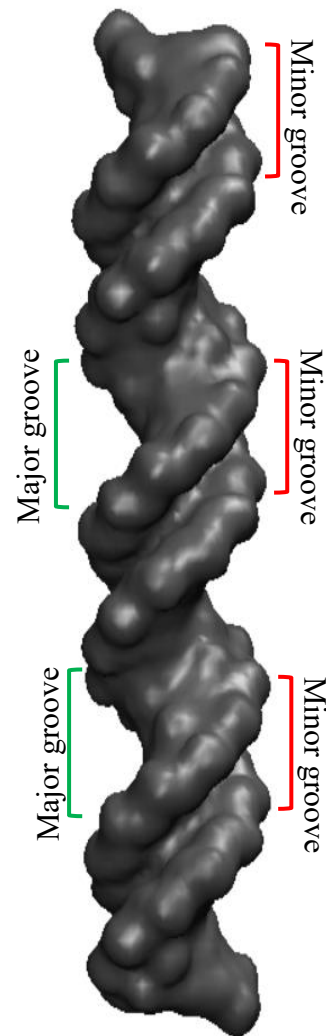
Figure 7: A) Chemical structure of DNA for adenine-thymine and guanine-cytosine base pairs. Dashed lines show hydrogen bonds. B) Structure of major grooves and minor grooves in DNA. Structures are drawn with the Python package RDKit. (http://www.rdkit.org) [80]. All code in Python [81] and Jupiter notebook [82] were implemented. The visualization of DNA is done by VMD software.

20

3.2. Proteins

Proteins are known as one of the most functionally sophisticated molecules. To understand the function of proteins, we need to understand their molecular structure.

Amino acids, the building blocks of proteins, are small organic molecules that consist of a central carbon atom (alpha) linked to an amino group ($-NH_2$), a carboxyl group (-COOH), a hydrogen atom, and a side chain (R group) that is a variable component (Figure 8). Amino acids differ from each other in their side chain R groups. There are only twenty amino acids in proteins; each has a unique side chain. Within a protein, multiple amino acids are linked together by peptide bonds to form a long chain [83].
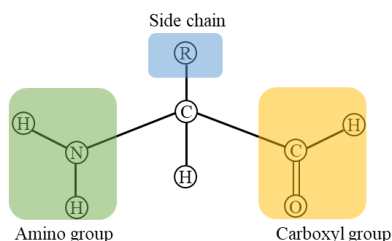

Figure 8: Structure of an amino acid containing the R side chain.

There are four protein structure levels: primary, secondary, tertiary, and quaternary. The primary structure of a protein is made of covalent peptide bonds between the carboxyl and amine groups of adjacent amino acids. The local packing of the polypeptide chain into α-helices and β-sheets forms the secondary structure. The α-helices and β-sheets are the results of hydrogen bonding between the amine and carboxyl groups of non-adjacent amino acids. If neither an alpha helix nor a β-sheet exists, a random coil is formed. A tertiary (3D) structure is made when the polypeptide chain coils and turns to form a complex molecular shape due to the interactions between R groups, including H-bonds, disulfide bridges, ionic bonds, and hydrophobic interactions. Quaternary

structure is defined by how multiple polypeptides interact to form a single, larger, biologically active protein.

4. Salts and co-solvents

Solvents have a direct and indirect role in the functioning of biological systems. In detail, solvents can actively participate in the biological processes or stabilize biologically active conformations of proteins and nucleic acids. Solvent interactions in biological environments can be changed by the presence of co-solvents such as ions and different small molecules. Non-aqueous environments are interesting in the context of industrial process biochemistry because they provide specific practical benefits.

Water is the most significant biomolecular solvent in almost all living habitats. Also, water is known as an excellent solvent due to its tiny size and its polar and polarizable nature. Its ability to act as both a hydrogen bond acceptor and donor enables it to form a range of structures that may readily adapt to changes in environmental conditions, particularly in the presence of biomolecules and other co-solutes [84]. Hence, water plays a key role in many biomolecular interactions and processes. The interaction of water with biomolecules is a complex subject. Several studies have been conducted to study the effect of salts on the structure, function, and properties of biomolecules in aqueous solutions during the past few years. For instance, Chandran et al. [85] tried to understand the binding characteristics and molecular mechanism of interactions of ILs with DNA in the mix ILs and water solution to investigate the stability of DNA in the long term. Their results showed that DNA maintains the native B-conformation in hydrated ILs and the interaction between IL cations and different parts of DNA has a great impact on the DNA stability. They also assumed the water cage around DNA was disrupted by the IL and partial dehydration occurred, which prevented the hydrolytic reactions that denatured DNA and helped stabilize DNA for the long term. In another work, Sakai et al. [4] investigate the effects of 32 Hofmeister salts on enzyme activity and stability of protein-glutaminase catalyzing the deamidation of only the side-chain amide group of glutamine residues in proteins. Their results revealed that the activation or stabilization of protein-glutaminase approximately followed the same order as the Hofmeister

series. They reported that the addition of Na_2CO_3 (1.0 M) increased the catalytic efficiency by 9.7-fold.

It should be emphasized that the explanation for the behavior of biomolecules in solutions in the presence of ions and co-solvents may not always follow a fixed pattern. As the subunits of different biomolecules interact with ions and co-solvents in different ways, predicting the general behavior of a given biomolecule dissolved in the mixed aqueous solution is very difficult. Furthermore, our knowledge about the solvent effects on biomolecule behavior at the molecular level is still poor. Thus, the effect of IL, inorganic salts, and DES on the biomolecule behavior in the aqueous solution was studied.

4.1. Ionic liquids

Ionic liquids (ILs) are a new class of solvents that has received a lot of attention as solvents in various areas of biochemistry due to their many advantages over volatile solvents [24]. Their valuable properties include negligible vapor pressure, high solvation ability, nonflammability, and good thermal stability, to mention but a few. It should be mentioned that ILs are ionic compounds and are typically liquid at room temperature (their melting temperatures are below 100 °C) [24].

ILs are divided into two main classes: protic ILs (PILs) and aprotic ILs (AILs). PILs with an available proton on the cation are a subset of ILs that are prepared through the stoichiometric neutralization reaction of certain Brønsted acids and Brønsted bases. AILs, the majority of ILs, are the result of substituting the acidic proton in a protic IL with a less labile cationic moiety, typically an alkyl group [86]. These two ILs are different in terms of the activity and strength of the forces between ions. PILs have a higher strength of Coulomb and hydrogen bonding interactions [24]. Furthermore, ILs can be derived from amino acids. As amino acids have a carboxylic acid residue in a single molecule, amino acids ILs (AAILs) can be used as the anions. It should be noted that it is easy to obtain pure AAILs in large quantities at a low cost. Also, AAILs can be used in the biological, medical, and pharmaceutical sciences, due to their great advantages, including biodegradability and biological activity [87]. Another class of ILs is magnetic ionic liquids (MILs), composed of organic ionic compounds in which the anion (usually) carries a net magnetic moment.

Examples of MIL anions include $[FeCl_4^-]$, $[MnBr_3^-]$, and $[CoCl_3^-]$. Structural formulas of representative ILs cations and anions are illustrated in Figure 9.

It is important to highlight that the physicochemical properties of ILs, namely solubility, polarity, viscosity, and acidity, can be altered by changing both cation and anion to meet specific requirements of applications in biochemistry, biotechnology, medicine, pharmacology, and bio-nanotechnology, etc. [88,86].

It has to be pointed out that most ILs readily dissolve in water. Water can change some of their properties (like viscosity) [89] and performances towards specific applications. It is also to be noted that, depending on the charge density of the anion and the length of the alkyl chain either on the cation or on the anion, ILs behave as hydrophilic or hydrophobic in water [24].
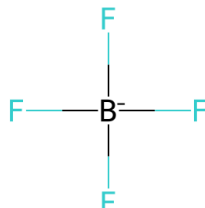
Based on the cation segment of ILs, they are categorized into four types: alkylammonium, dialkylimidazolium-, phosphonium- and N-alkylpyridinium based ILs [90]. As in this thesis, the behaviors of biomolecules in the aqueous solution of imidazolium-based ILs have been investigated; in the following paragraphs, the properties of this class of ILs will be explained more.

Imidazolium-based ILs are one of the most popularly investigated ILs that have been applied in many fields due to the unique structure of imidazolium and its attractive physicochemical features. Choosing the imidazolium ring as a cation (Figure 10) is often due to its stability within oxidative and reductive conditions, the low viscosity of imidazolium ILs, and their ease of synthesis [90]. The imidazolium ring is a five-membered heterocyclic structure that is planar, rigid, and π-conjugated [91]. It is to be noted that anions mostly have strong interactions with the imidazolium-ring. In this thesis, the interaction of an anion with the hydrogen atoms of the 1-butyl-3 methylimidazolium cation ring denoted H1, H2, and H3 (see Figure 10) was investigated. According to our investigation, the H1 atom of the imidazolium-ring has more affinity toward the anions with respect to other hydrogen atoms, due to its highest positive-charge density in comparison with two other hydrogen atoms in the imidazolium ring cation.
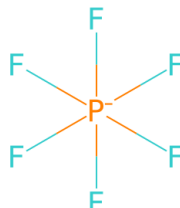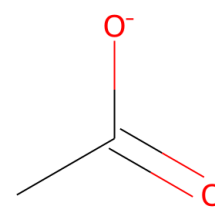
Anions
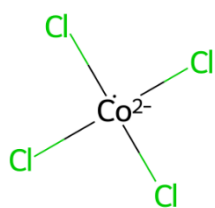
Tetrachlorocobaltate(2-)	Tetrafluoroborate	Hexafluorophosphate	Acetate
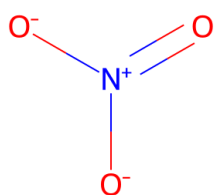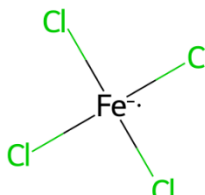
Nitrate	Tetrachloroferrate(1-)	Cystein	Mesylate
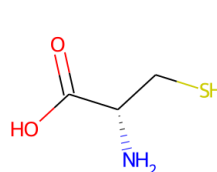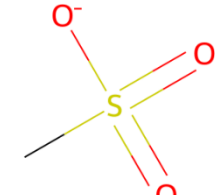
Cations
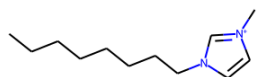
1-Octyl-3-methylimidazolium
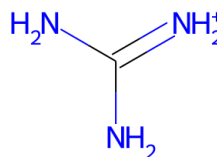
Guanidinium
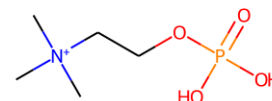
Phosphocholine
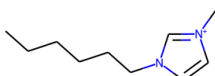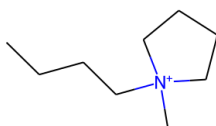
1-Hexyl-3-methylimidazolium	1-Butyl-1-methylpyrrolidinium	1-Butyl-3 methylimidazolium	Choline
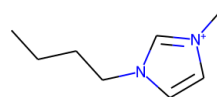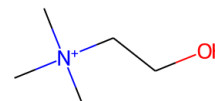
Figure 9: Structural formula of cations and anions from selected ILs [86]. Structures are drawn with the python package RDKit. (Available from: http://www.rdkit.org) [80]. All code in Python [81] and Jupiter notebook [82] were implemented.

H: Ring H-atom: H1
H: Ring H-atom: H2
H: Ring H-atom: H3
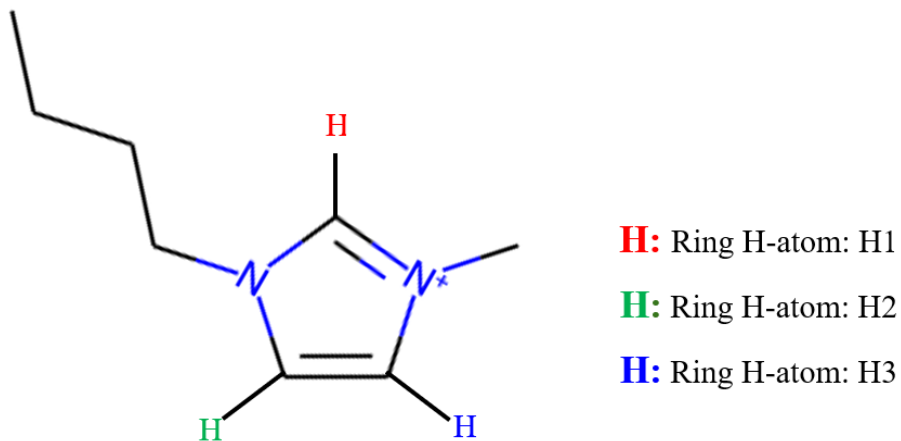
Figure 10: Chemical structure of the 1-butyl-3 methylimidazolium cation.

4.2. Deep Eutectic Solvent

Deep eutectic solvents (DESs) are considered a new class of ILs analogs due to their sharing many characteristics and properties with ILs. The physicochemical properties of DESs, including having low volatility, nonflammability, low vapor pressure, and chemical and thermal stability, are the main reasons behind researchers' rising interest in these solvents. DESs consist of large, nonsymmetric ions that have low lattice energy and hence low melting points. DESs are usually made of a quaternary ammonium salt with a metal salt or hydrogen bond donor (HBD) [92]. The general formula for DESs is:

$$Cat^+X^-zY \tag{14}$$
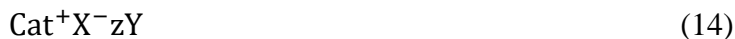
Where Cat^+ can be an ammonium, phosphonium, or sulfonium cation, and X is a Lewis base. The anionic species are formed between X and either a Lewis or Brønsted acid Y. z is the number of Y molecules that interact with the anion [92]. Figure 11 depicts some of the most used hydrogen bond acceptors and donors.

Hydrogen Bond Acceptors

Choline chloride   Ethylazanium;chloride   Proline   Choline acetate

Tetrabutylammonium bromide   Betaine hydrochloride   Alanine

Hydrogen Bond Donors

Urea   Thiourea   Acetamide   Ethylene Glycol

Glycerol   1,2-Propanediol   Oxalic Acid   Glycolic acid

Lactic Acid   Levulinic acid   Malic acid   Malonic acid
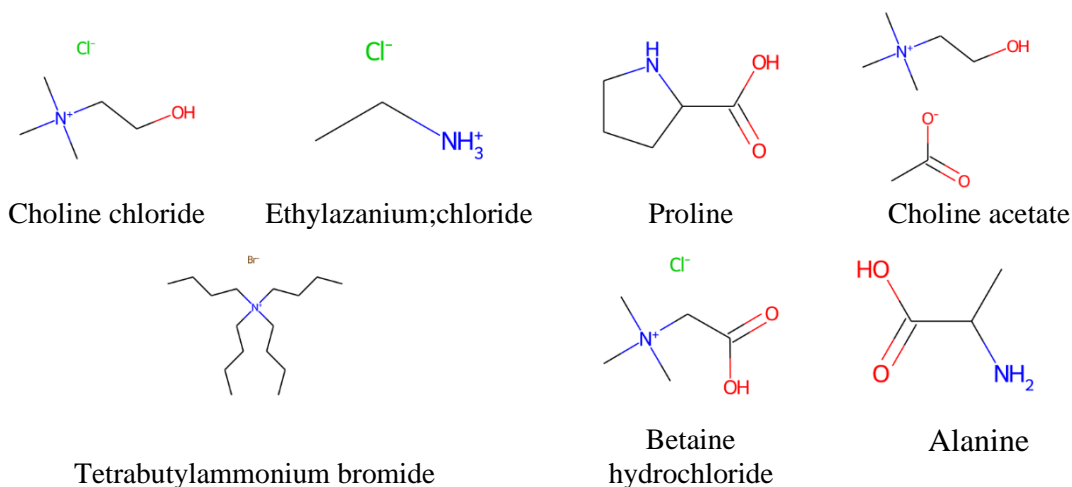
Figure 11: Common hydrogen bond acceptors and hydrogen bond donors used for preparation of deep eutectic solvents [93] Structures are drawn with the python package RDKit. (Available from: http://www.rdkit.org) [80]. All code in Python [81] and Jupiter notebook [82] were implemented.

4.3. Hofmeister series

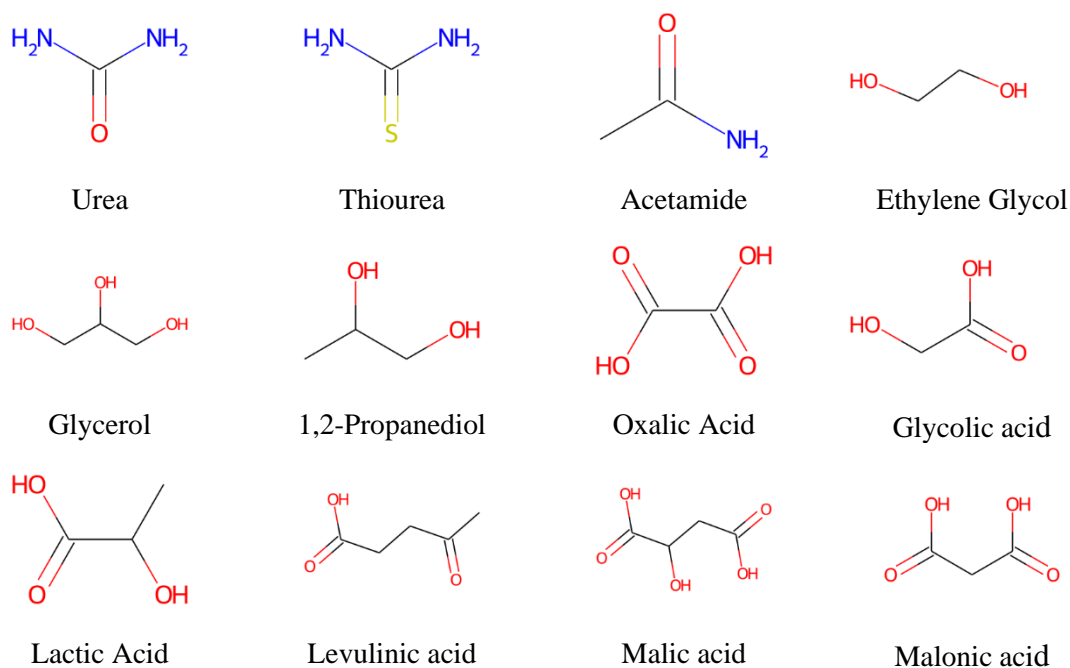Hofmeister investigated the effect of salts on biomolecules for the first time, and his findings are summarized in the Hofmeister series [2,94]. The Hofmeister series reflects the effect of ions on the behavior of macromolecules by influencing the structure of water molecules and direct ion–macromolecule interactions as well as interactions with water molecules in the first hydration shell of the macromolecule [95]. It should be mentioned that such effects are generally more pronounced for anions than for cations. the typical ordering of It should be mentioned that such effects are generally more pronounced for anions than for cations. The typical ordering of the anion series is as follows:

$$CO_3^{2-} > SO_4^{2-} > S_2O_3^{2-} > H_2PO_4^- > F^- > Cl^- > Br^- > NO_3^- > I^- > ClO_4^- > SCN^-$$
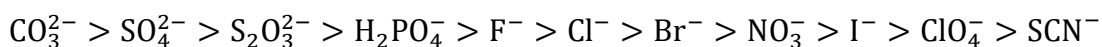
The anions that are located on the left side of Cl are called kosmotropes, while those to its right are called chaotropic. The kosmotropes assumed to be water structure makers are strongly hydrated and have stabilizing and salting-out effects on proteins and macromolecules. However, chaotropes considered water structure breakers are known to destabilize folded proteins and give rise to salting-in behavior [95].

During my Ph.D. program, two studies were done to investigate the influence of the Hofmeister series on the properties of enzymes. In the first study [23], the influence of the selected anions on the catalytic and conformational properties of human rhinovirus-14 (HRV) 3C protease was studied. Human rhinovirus (HRV) infections, the most frequent causative agents of the common cold are members of the picornavirus family. All the members of this family have a positive-sense, single-stranded RNA genome that is translated into a single polyprotein precursor. In the case of HRVs, the viral polyprotein is processed by 3C. The 3C protease catalyzes most of the subsequent internal cleavages to generate functional proteins and enzymes [96]. In this study, the stability of the protein backbone along the simulation trajectories (100 ns) in the aqueous solution and aqueous solution of Na_2SO_4 (kosmotropic), NaCl (neutral from the point of view of theHofmeister effect) and $NaClO_4$ (chaotropic) were investigated by RMSD. The protein backbone solvated in aqueous solutions of Na_2SO_4 has much smaller RMSD values in comparison to the RMSD values of the protein backbone in the aqueous solution and in the aqueous solution of NaCl and $NaClO_4$. Also,

the RMSD values in the presence of NaCl are smaller than the RMSD values of the protein backbone in water and, $NaClO_4$. Furthermore, a more detailed representation of the difference in the flexibility or stability of residues within the simulation was obtained by measuring the RMSF analysis of each residue of HRV 3C protease. HRV 3C protease residues in the aqueous solution of Na_2SO_4 have fewer fluctuations as compared to the water or in the presence of sodium chloride. Obtained results clearly showed that the HRV 3C protease in the presence of kosmotropic anions, in contrast with chaotropic anions, displays increased stability. This observation agreed with the Hofmeister effect and enables us to rank anion ability to the rigidity of the protein backbone in the order from most (sulfate) to least rigidifying conditions (perchlorate and/or water).

In the second study [22], the global stability, ligand binding, and catalytic properties of trypsin by anions were examined. Trypsin (EC 3.4.21.4) is a pancreatic serine protease that selectively catalyzes the hydrolysis of ester, amide and, peptide bonds at the carboxyl side of arginine, lysine and ornithine. Trypsin can be applied in biological research and be used for organic synthesis. It is worth mentioning that trypsin is less active and stable in the presence of organic solvents [97]. In this work, RMSD measurements of C-alpha atoms of the trypsin enzyme in water and 1 M aqueous solutions of Na2SO4, NaCl, and NaClO4 revealed that the trypsin enzyme is more stable in the aqueous solution of Na2SO4 compared to other aqueous solution and the aqueous solution of other salts. Also, the dynamics of each residue in the polypeptide chain and the interaction of selected amino acid residues with anions were investigated by RMSF and RDF, respectively. A detailed analysis of MD simulations indicates that a particular residue in the binding pocket and two specific residues in the loop have a high affinity to sulfate in comparison with the perchlorate anions, with a possible influence on the stability of this part of the enzyme. Generally speaking, our results showed that that the effect of the specific anion on trypsin properties agrees with the localization of the anions in the Hofmeister series.

References:

(1) Bellissent-Funel, M.-C.; Hassanali, A.; Havenith, M.; Henchman, R.; Pohl, P.; Sterpone, F.; Van Der Spoel, D.; Xu, Y.; Garcia, A. E. Water determines the structure and dynamics of proteins. *Chemical reviews* **2016**, *116* (13), 7673-7697.

(2) Hofmeister, F. About the science of the effects of salts: About the water withdrawing effect of the salts. *Arch. Exp. Pathol. Pharmacol.* **1888**, *24*, 247-260.

(3) Kang, B.; Tang, H.; Zhao, Z.; Song, S. Hofmeister series: Insights of ion specificity from amphiphilic assembly and interface property. *ACS omega* **2020**, *5* (12), 6229-6239.

(4) Sakai, K.; Sato, Y.; Okada, M.; Yamaguchi, S. Enhanced activity and stability of protein-glutaminase by Hofmeister effects. *Molecular Catalysis* **2022**, *517*, 112054.

(5) Dušeková, E.; Garajová, K.; Yavaşer, R.; Varhač, R.; Sedlák, E. Hofmeister effect on catalytic properties of chymotrypsin is substrate-dependent. *Biophysical Chemistry* **2018**, *243*, 8-16.

(6) Garajová, K.; Balogová, A.; Dušeková, E.; Sedláková, D.; Sedlák, E.; Varhač, R. Correlation of lysozyme activity and stability in the presence of Hofmeister series anions. *Biochimica et Biophysica Acta (BBA)-Proteins and Proteomics* **2017**, *1865* (3), 281-288.

(7) Sedlák, E.; Stagg, L.; Wittung-Stafshede, P. Effect of Hofmeister ions on protein thermal stability: roles of ion hydration and peptide groups? *Archives of Biochemistry and Biophysics* **2008**, *479* (1), 69-73.

(8) Jha, I.; Attri, P.; Venkatesu, P. Unexpected effects of the alteration of structure and stability of myoglobin and hemoglobin in ammonium-based ionic liquids. *Physical Chemistry Chemical Physics* **2014**, *16* (12), 5514-5526.

(9) Micaêlo, N. M.; Soares, C. M. Protein structure and dynamics in ionic liquids. Insights from molecular dynamics simulation studies. *The Journal of Physical Chemistry B* **2008**, *112* (9), 2566-2572.

(10) Ghosh, S.; Parui, S.; Jana, B.; Bhattacharyya, K. Ionic liquid induced dehydration and domain closure in lysozyme: FCS and MD simulation. *The Journal of Chemical Physics* **2015**, *143* (12), 09B622_621.

(11) Ajloo, D.; Sangian, M.; Ghadamgahi, M.; Evini, M.; Saboury, A. A. Effect of two imidazolium derivatives of ionic liquids on the structure and activity of adenosine deaminase. *International journal of biological macromolecules* **2013**, *55*, 47-61.

(12) D'Oronzo, E.; Secundo, F.; Minofar, B.; Kulik, N.; Pometun, A. A.; Tishkov, V. I. Activation/inactivation role of ionic liquids on formate dehydrogenase from Pseudomonas sp. 101 and its mutated thermostable form. *ChemCatChem* **2018**, *10* (15), 3247-3259.

(13) Jumbri, K.; Rahman, M. A.; Abdulmalek, E.; Ahmad, H.; Micaelo, N. An insight into structure and stability of DNA in ionic liquids from molecular dynamics simulation and experimental studies. *Physical Chemistry Chemical Physics* **2014**, *16* (27), 14036-14046.

(14) Pabbathi, A.; Samanta, A. Spectroscopic and molecular docking study of the interaction of DNA with a morpholinium ionic liquid. *The Journal of Physical Chemistry B* **2015**, *119* (34), 11099-11105.

(15) Abbott, A. P.; Capper, G.; Davies, D. L.; Rasheed, R. K.; Tambyrajah, V. Novel solvent properties of choline chloride/urea mixtures. *Chemical communications* **2003**, (1), 70-71.

(16) Maugeri, Z.; de María, P. D. Novel choline-chloride-based deep-eutectic-solvents with renewable hydrogen bond donors: levulinic acid and sugar-based polyols. *Rsc Advances* **2012**, *2* (2), 421-425.

(17) Stepankova, V.; Vanacek, P.; Damborsky, J.; Chaloupkova, R. Comparison of catalysis by haloalkane dehalogenases in aqueous solutions of deep eutectic and organic solvents. *Green Chemistry* **2014**, *16* (5), 2754-2761.

(18) Huang, Z. L.; Wu, B. P.; Wen, Q.; Yang, T. X.; Yang, Z. Deep eutectic solvents can be viable enzyme activators and stabilizers. *Journal of Chemical Technology & Biotechnology* **2014**, *89* (12), 1975-1981.

(19) Fadaei, F.; Tortora, M.; Gessini, A.; Masciovecchio, C.; Catalini, S.; Vigna, J.; Mancini, I.; Mele, A.; Vacek, J.; Reha, D. Structural specificity of groove binding mechanism between imidazolium-based ionic liquids and DNA revealed by synchrotron-UV Resonance Raman spectroscopy and molecular dynamics simulations. *Journal of Molecular Liquids* **2022**, *347*, 118350.

(20) Fadaei, F.; Seifert, M.; Raymond, J. R.; Řeha, D.; Kulik, N.; Minofar, B.; Heitz, M. P. Interactions between a dsDNA Oligonucleotide and Imidazolium Chloride Ionic Liquids: Effect of Alkyl Chain Length, Part I. *Molecules* **2022**, *27* (1), 116.

(21) Zara, Z.; Mishra, D.; Pandey, S. K.; Csefalvay, E.; Fadaei, F.; Minofar, B.; Řeha, D. Surface Interaction of Ionic Liquids: Stabilization of Polyethylene Terephthalate-Degrading Enzymes in Solution. *Molecules* **2022**, *27* (1), 119.

(22) Dušeková, E.; Garajová, K.; Yavaşer, R.; Tomková, M.; Sedláková, D.; Dzurillová, V.; Kulik, N.; Fadaei, F.; Shaposhnikova, A.; Minofar, B. Modulation of global stability, ligand binding and catalytic properties of trypsin by anions. *Biophysical Chemistry* **2022**, *288*, 106856.

(23) Dušeková, E.; Berta, M.; Sedláková, D.; Řeha, D.; Dzurillová, V.; Shaposhnikova, A.; Fadaei, F.; Tomková, M.; Minofar, B.; Sedlák, E. Specific anion effect on properties of HRV 3C protease. *Biophysical Chemistry* **2022**, *287*, 106825.

(24) Shukla, S. K.; Mikkola, J.-P. Use of ionic liquids in protein and DNA chemistry. *Frontiers in Chemistry* **2020**, *8*, 598662.

(25) Alder, B. J.; Wainwright, T. E. Phase transition for a hard sphere system. *The Journal of chemical physics* **1957**, *27* (5), 1208-1209.

(26) Hollingsworth, S. A.; Dror, R. O. Molecular dynamics simulation for all. *Neuron* **2018**, *99* (6), 1129-1143.

(27) McCammon, J. A.; Gelin, B. R.; Karplus, M. Dynamics of folded proteins. *nature* **1977**, *267* (5612), 585-590.

(28) Leach, A. R.; Leach, A. R. *Molecular modelling: principles and applications*; Pearson education, 2001.

(29) Swope, W. C.; Andersen, H. C.; Berens, P. H.; Wilson, K. R. A computer simulation method for the calculation of equilibrium constants for the formation of physical clusters of molecules: Application to small water clusters. *The Journal of chemical physics* **1982**, *76* (1), 637-649.

(30) Bauer, P.; Hess, B.; Lindahl, E. GROMACS 2022.1 Manual. *Zenodo* **2022**.

(31) Van Gunsteren, W. F.; Berendsen, H. J. A leap-frog algorithm for stochastic dynamics. *Molecular Simulation* **1988**, *1* (3), 173-185.

(32) Khabiri, M. Computational Investigations of Biomolecular Systems and Comparison with Experiments in Various Environmental Conditions. *Nove Hrady, Czech Republic* **2011**.

(33) Copps, J.; Murphy, R. F.; Lovas, S. Molecular dynamics simulations of peptides. In *Peptide-Based Drug Design*, Springer, 2008; pp 115-126.

(34) Genheden, S.; Reymer, A.; Saenz-Méndez, P.; Eriksson, L. A. Computational chemistry and molecular modelling basics. **2017**.

(35) Pérez, A.; Marchán, I.; Svozil, D.; Sponer, J.; Cheatham III, T. E.; Laughton, C. A.; Orozco, M. Refinement of the AMBER force field for nucleic acids: improving the description of α/γ conformers. *Biophysical journal* **2007**, *92* (11), 3817-3829.

(36) Salomon-Ferrer, R.; Case, D. A.; Walker, R. C. An overview of the Amber biomolecular simulation package. *Wiley Interdisciplinary Reviews: Computational Molecular Science* **2013**, *3* (2), 198-210.

(37) Case, D. A.; Cheatham III, T. E.; Darden, T.; Gohlke, H.; Luo, R.; Merz Jr, K. M.; Onufriev, A.; Simmerling, C.; Wang, B.; Woods, R. J. The Amber biomolecular simulation programs. *Journal of computational chemistry* **2005**, *26* (16), 1668-1688.

(38) Vanommeslaeghe, K.; Pamidighantam, S.; Sheetz, R. M.; Connolly, J. W.; Roitberg, A. E.; MacKerell Jr, A. D. Toward an automatic force field parametrization engine: assignment of parameters by analogy for the CHARMM General Force Field (CGenFF). In *Abstracts of Papers of the American Chemical Society*, 2009; AMER CHEMICAL SOC 1155 16TH ST, NW, WASHINGTON, DC 20036 USA: Vol. 238.

(39) Jorgensen, W. L.; Maxwell, D. S.; Tirado-Rives, J. Development and testing of the OPLS all-atom force field on conformational energetics and properties of organic liquids. *Journal of the American Chemical Society* **1996**, *118* (45), 11225-11236.

(40) Wang, J.; Wolf, R. M.; Caldwell, J. W.; Kollman, P. A.; Case, D. A. Development and testing of a general amber force field. *Journal of computational chemistry* **2004**, *25* (9), 1157-1174.

(41) Hess, B.; Bekker, H.; Berendsen, H. J.; Fraaije, J. G. LINCS: A linear constraint solver for molecular simulations. *Journal of computational chemistry* **1997**, *18* (12), 1463-1472.

(42) Ryckaert, J.-P.; Ciccotti, G.; Berendsen, H. J. Numerical integration of the cartesian equations of motion of a system with constraints: molecular dynamics of n-alkanes. *Journal of computational physics* **1977**, *23* (3), 327-341.

(43) Vanommeslaeghe, K.; MacKerell Jr, A. D. Automation of the CHARMM General Force Field (CGenFF) I: bond perception and atom typing. *Journal of chemical information and modeling* **2012**, *52* (12), 3144-3154.

(44) Venable, R. M.; Kramer, A.; Pastor, R. W. Molecular dynamics simulations of membrane permeability. *Chemical reviews* **2019**, *119* (9), 5954-5997.

(45) Allen, M. P.; Tildesley, D. J. *Computer simulation of liquids*; Oxford university press, 2017.

(46) Brooks III, C. L. Methodological advances in molecular dynamics simulations of biological systems. *Current opinion in structural biology* **1995**, *5* (2), 211-215.

(47) Berendsen, H. J.; Postma, J. v.; Van Gunsteren, W. F.; DiNola, A.; Haak, J. R. Molecular dynamics with coupling to an external bath. *The Journal of chemical physics* **1984**, *81* (8), 3684-3690.

(48) Andersen, H. C. Molecular dynamics simulations at constant pressure and/or temperature. *The Journal of chemical physics* **1980**, *72* (4), 2384-2393.

(49) Nosé, S. A molecular dynamics method for simulations in the canonical ensemble. *Molecular physics* **1984**, *52* (2), 255-268.

(50) Hoover, W. G. Canonical dynamics: Equilibrium phase-space distributions. *Physical review A* **1985**, *31* (3), 1695.

(51) Bussi, G.; Donadio, D.; Parrinello, M. Canonical sampling through velocity rescaling. *The Journal of chemical physics* **2007**, *126* (1), 014101.

(52) Nosé, S.; Klein, M. Constant pressure molecular dynamics for molecular systems. *Molecular Physics* **1983**, *50* (5), 1055-1076.

(53) Parrinello, M.; Rahman, A. Polymorphic transitions in single crystals: A new molecular dynamics method. *Journal of Applied physics* **1981**, *52* (12), 7182-7190.

(54) Martyna, G. J.; Tuckerman, M. E.; Tobias, D. J.; Klein, M. L. Explicit reversible integrators for extended systems dynamics. *Molecular Physics* **1996**, *87* (5), 1117-1157.

(55) Berendsen, H. J.; van der Spoel, D.; van Drunen, R. GROMACS: A message-passing parallel molecular dynamics implementation. *Computer physics communications* **1995**, *91* (1-3), 43-56.

(56) Lindahl, E.; Hess, B.; Van Der Spoel, D. GROMACS 3.0: a package for molecular simulation and trajectory analysis. *Molecular modeling annual* **2001**, *7*, 306-317.

(57) Van Der Spoel, D.; Lindahl, E.; Hess, B.; Groenhof, G.; Mark, A. E.; Berendsen, H. J. GROMACS: fast, flexible, and free. *Journal of computational chemistry* **2005**, *26* (16), 1701-1718.

(58) Hess, B.; Kutzner, C.; Van Der Spoel, D.; Lindahl, E. GROMACS 4: algorithms for highly efficient, load-balanced, and scalable molecular simulation. *Journal of chemical theory and computation* **2008**, *4* (3), 435-447.

(59) Páll, S.; Abraham, M. J.; Kutzner, C.; Hess, B.; Lindahl, E. Tackling exascale software challenges in molecular dynamics simulations with GROMACS. In *Solving Software Challenges for Exascale: International Conference on Exascale Applications and Software, EASC 2014, Stockholm, Sweden, April 2-3, 2014, Revised Selected Papers 2*, 2015; Springer: pp 3-27.

(60) Abraham, M. J.; Murtola, T.; Schulz, R.; Páll, S.; Smith, J. C.; Hess, B.; Lindahl, E. GROMACS: High performance molecular simulations through multi-level parallelism from laptops to supercomputers. *SoftwareX* **2015**, *1*, 19-25.

(61) Pronk, S.; Páll, S.; Schulz, R.; Larsson, P.; Bjelkmar, P.; Apostolov, R.; Shirts, M. R.; Smith, J. C.; Kasson, P. M.; Van Der Spoel, D. GROMACS 4.5: a high-throughput and highly parallel open source molecular simulation toolkit. *Bioinformatics* **2013**, *29* (7), 845-854.

(62) Kutzner, B.; Van der Spoel, D.; Lindahl, E. Gromacs 4: Algorithms for Highly Efficient, Load–Balanced, and Scalable Molecular Simulation Hess. *J Chem Theory Comput* **2008**, *4*, 435-447.

(63) Humphrey, W.; Dalke, A.; Schulten, K. VMD: visual molecular dynamics. *Journal of molecular graphics* **1996**, *14* (1), 33-38.

(64) Berman, H. M.; Westbrook, J.; Feng, Z.; Gilliland, G.; Bhat, T. N.; Weissig, H.; Shindyalov, I. N.; Bourne, P. E. The protein data bank. *Nucleic acids research* **2000**, *28* (1), 235-242.

(65) Burley, S. K.; Bhikadiya, C.; Bi, C.; Bittrich, S.; Chen, L.; Crichlow, G. V.; Christie, C. H.; Dalenberg, K.; Di Costanzo, L.; Duarte, J. M. RCSB Protein Data Bank: powerful new tools for exploring 3D structures of biological macromolecules for basic and applied research and education in fundamental biology, biomedicine, biotechnology, bioengineering and energy sciences. *Nucleic acids research* **2021**, *49* (D1), D437-D451.

(66) Nutt, D. R.; Smith, J. C. Molecular dynamics simulations of proteins: Can the explicit water model be varied? *Journal of Chemical Theory and Computation* **2007**, *3* (4), 1550-1560.

(67) Prasad, V.; Kannam, S. K.; Hartkamp, R.; Sathian, S. P. Water desalination using graphene nanopores: influence of the water models used in simulations. *Physical Chemistry Chemical Physics* **2018**, *20* (23), 16005-16011.

(68) van der Kamp, M. W.; Shaw, K. E.; Woods, C. J.; Mulholland, A. J. Biomolecular simulation and modelling: status, progress and prospects. *Journal of the Royal Society interface* **2008**, *5* (suppl_3), 173-190.

(69) Martínez, L. Automatic identification of mobile and rigid substructures in molecular dynamics simulations and fractional structural fluctuation analysis. *PloS one* **2015**, *10* (3), e0119264.

(70) LaBean, T. H.; Li, H. Constructing novel materials with DNA. *Nano Today* **2007**, *2* (2), 26-35. Vijayaraghavan, R.; Izgorodin, A.; Ganesh, V.; Surianarayanan, M.; MacFarlane, D. R. Long-term structural and chemical stability of DNA in hydrated ionic liquids. *Angewandte Chemie International Edition* **2010**, *49* (9), 1631-1633.

(71) Chidchob, P.; Sleiman, H. F. Recent advances in DNA nanotechnology. *Current opinion in chemical biology* **2018**, *46*, 63-70.

(72) Seeman, N. C.; Sleiman, H. F. DNA nanotechnology. *Nature Reviews Materials* **2017**, *3* (1), 1-23.

(73) Bansal, M. DNA structure: Revisiting the Watson–Crick double helix. *Current Science* **2003**, 1556-1563.

(74) Alberts, B.; Johnson, A.; Lewis, J.; Raff, M.; Roberts, K.; Walter, P. The structure and function of DNA. In *Molecular Biology of the Cell. 4th edition*, Garland Science, 2002.

(75) Abrescia, N. G.; Thompson, A.; Huynh-Dinh, T.; Subirana, J. A. Crystal structure of an antiparallel DNA fragment with Hoogsteen base pairing. *Proceedings of the National Academy of Sciences* **2002**, *99* (5), 2806-2811.

(76) Gardner, M. J.; Hall, N.; Fung, E.; White, O.; Berriman, M.; Hyman, R. W.; Carlton, J. M.; Pain, A.; Nelson, K. E.; Bowman, S. Genome sequence of the human malaria parasite Plasmodium falciparum. *Nature* **2002**, *419* (6906), 498-511.

(77) Bulloch, M. S.; Ralph, S. A. Is the AT-rich DNA of malaria parasites a drug target? *Trends in Pharmacological Sciences* **2022**.

(78) Ghosh, A.; Bansal, M. A glossary of DNA structures from A to Z. *Acta Crystallographica Section D: Biological Crystallography* **2003**, *59* (4), 620-626.

(79) Watson, J. D.; Crick, F. H. Molecular structure of nucleic acids: a structure for deoxyribose nucleic acid. *Nature* **1953**, *171* (4356), 737-738.

(80) Landrum, G. RDKit: Open-source cheminformatics. **2006**.

(81) Van Rossum, G.; Drake, F. L. *Python 3 reference manual*; CreateSpace, 2009.

(82) Kluyver, T.; Ragan-Kelley, B.; Pérez, F.; Granger, B. E.; Bussonnier, M.; Frederic, J.; Kelley, K.; Hamrick, J. B.; Grout, J.; Corlay, S. *Jupyter Notebooks-a publishing format for reproducible computational workflows*; 2016.

(83) O'Connor, C. M.; Adams, J. U.; Fairman, J. Essentials of cell biology. *Cambridge, MA: NPG Education* **2010**, *1*, 54.

(84) Feig, M. *Modeling solvent environments: applications to simulations of biomolecules*; John Wiley & Sons, 2009.

(85) Chandran, A.; Ghoshdastidar, D.; Senapati, S. Groove binding mechanism of ionic liquids: a key factor in long-term stability of DNA in hydrated ionic liquids? *Journal of the American Chemical Society* **2012**, *134* (50), 20330-20339.

(86) Benedetto, A.; Ballone, P. Room-temperature ionic liquids and biomembranes: setting the stage for applications in pharmacology, biomedicine, and bionanotechnology. *Langmuir* **2018**, *34* (33), 9579-9597.

(87) Ohno, H.; Fukumoto, K. Amino acid ionic liquids. *Accounts of chemical research* **2007**, *40* (11), 1122-1129.

(88) Earle, M. J.; Seddon, K. R. Ionic liquids. Green solvents for the future. *Pure and applied chemistry* **2000**, *72* (7), 1391-1398.

(89) Rodriguez, H.; Brennecke, J. F. Temperature and composition dependence of the density and viscosity of binary mixtures of water+ ionic liquid. *Journal of Chemical & Engineering Data* **2006**, *51* (6), 2145-2155.

(90) Ghandi, K. A review of ionic liquids, their limits and applications. *Green and sustainable chemistry* **2014**, *2014*.

(91) Wang, B.; Qin, L.; Mu, T.; Xue, Z.; Gao, G. Are ionic liquids chemically stable? *Chemical reviews* **2017**, *117* (10), 7113-7131.

(92) Smith, E. L.; Abbott, A. P.; Ryder, K. S. Deep eutectic solvents (DESs) and their applications. *Chemical reviews* **2014**, *114* (21), 11060-11082.

(93) El Achkar, T.; Greige-Gerges, H.; Fourmentin, S. Basics and properties of deep eutectic solvents: a review. *Environmental Chemistry Letters* **2021**, *19* (4), 3397-3408.

(94) Hofmeister, F. About the water withdrawing effect of the salts. *Archiv fuer experimentelle Pathologie und Pharmakologie* **1888**, *25*, 1-30.

(95) Zhang, Y.; Cremer, P. S. Interactions between macromolecules and ions: the Hofmeister series. *Current opinion in chemical biology* **2006**, *10* (6), 658-663.

(96) Cox, G. A.; Johnson, R. B.; Cook, J. A.; Wakulchik, M.; Johnson, M. G.; Villarreal, E. C.; Wang, Q. M. Identification and characterization of human rhinovirus-14 3C protease deamidation isoform. *Journal of Biological Chemistry* **1999**, *274* (19), 13211-13216.

(97) Aslani, E.; Abri, A.; Pazhang, M. Immobilization of trypsin onto Fe3O4@ SiO2–NH2 and study of its activity and stability. *Colloids and Surfaces B: Biointerfaces* **2018**, *170*, 553-562.

CHAPTER 2

Structural specificity of groove binding mechanism between imidazolium-based Ionic Liquids and DNA revealed by synchrotron-UV Resonance Raman spectroscopy and molecular dynamics simulations.

Structural specificity of groove binding mechanism between imidazolium-based Ionic Liquids and DNA revealed by synchrotron-UV Resonance Raman spectroscopy and molecular dynamics simulations.

Abstract

The predicted capability of Ionic Liquids (ILs) in stabilizing the native structure of nucleic acids is relevant in the field of biotechnology, especially for DNA storage and handling. In the present work, we implement a joint combination of advanced spectroscopic techniques such as synchrotron-UV Resonance Raman spectroscopy (SR-UVRR) and molecular dynamics (MD) simulations for deepening insight into the sequence and structural specificity of the binding interactions between imidazolium-based ILs and both the phosphate groups and nucleobases in the minor and major grooves of double strand DNA. A 30-base pair double-strand DNA structure has been chosen as model of natural DNA. The experimental and simulation results consistently give rise evidence the predominance of a groove binding mechanism between ILs cations and DNA, with a preferential interaction established between guanine residues and the shorter alkyl-chain length on imidazolium cation. Raman experiments allows us to detect both cooperative transition and reversible pre-melting structural transformation, involving specific tracts in the structure of DNA, that are activated at lower temperature for guanine residues with respect to adenine ones. The more marked affect operated by the imidazolium-based ILs with chloride as anion on the pre-melting states of adenine suggests a selective strong interaction of this anion with the adenine-rich tracts on the structure of DNA. MD simulation results reveal the influence of ILs on the structural properties of DNA and provide more details about the solvation, interaction, stability and flexibility of DNA in the hydrated ILs. According to the MD simulation analysis, a combination of electrostatic and hydrophobic interactions drives shorter alkyl-chain length of imidazolium cations to has stronger interaction with the DNA major groove.

Keywords: Synchrotron UV Resonance Raman, Molecular dynamics, ionic liquids, nucleic acids, solvation

Introduction

Thanks to the well-known programmability of the Watson-Crick pairing interactions, Deoxyribonucleic acid (DNA) is acquiring a crucial role as building-block for developing DNA-based devices in nanotechnology and biomedical technology [1-4]. For instance, the sequence-based recognition mechanism of DNA has been employed in DNA microarrays of gene expression analyses [5] and in chips for gene sequencing by hybridization [6,7]. Nanoscale self-assembly methods have been used for the construction of 2D and 3D ordered structures of DNA [8] and the design of hybrid materials such as metallic nanoparticles [9]. However, the lack of an appropriate medium in which nucleic acids are able to preserve their structures for a long time and under various conditions is becoming the bottleneck that limits the further expanding of the use of DNA in nanotechnology. Although DNA is considered reasonably stable in aqueous solution, the degradation of the chemical structure of DNA has been observed for long storage periods at room temperature [10]. Moreover, DNA is vulnerable to hydrolytic and oxidative damage in aqueous solutions [11,12]. Besides the inherent chemical instability of DNA in water, other conditions such as non-physiological temperature, pH and ionic strength or repeated freeze-thaw cycles can destroy the DNA helix structure and cause denaturation. Furthermore, the use of aqueous DNA samples

makes difficult some technological processes implemented in nanotechnology since small volumes of water vaporizes immediately under open-air conditions or at high temperatures [13]. For these reasons, finding appropriate media that ensure to prolong the stability of DNA and to overcome the limitations of the use of aqueous buffers remains a challenging task.

Ionic liquids (ILs) are a class of organic salts majorly liquid at room temperature that offer unique opportunities if used as alternative solvents or co-solvents in various physical and chemical transformations [14]. In the last two decades, ILs has gained increasing popularity in biotechnology for a broad range of applications. Both experimental and simulation works have addressed the potential benefits exerted by the neat or aqueous solutions of ILs in the stabilization and functioning of proteins and DNA [15-19]. With respect to more common co-solutes or co-solvents, the large number of possible anion/cation combinations of ILs offers the possibility to design tailor-made compounds for specific purposes. Moreover, certain remarkable features of ILs, such as their vanishing vapour pressure, provide an attractive alternative to water in a large variety of applications [20]. Unlike the multiple studies reported on the effects of ILs on the structure and function of proteins, much less is known on the properties of DNA dissolved in pure or aqueous solution of ILs [13,19, 21-23]. The first experimental observation that DNA preserves its structure in various ILs during long-term storage at room temperature was provided by the pioneering study of MacFarlane [24]. A joint molecular dynamics simulation and spectroscopic study [25] suggest that site-specific interactions of IL cations and anions with DNA favor the long-term structural stability of nucleic acids in aqueous solutions of ILs. Other studies reveal that several types of ILs contribute to enhance DNA stability without modifying its structure [26-33]. Additionally, ILs can be potentially used for controlling the properties of the nucleic acids, for example for increasing the sensitivity of electrochemical DNA sensors [34], and for developing more efficient protocols for extraction and purification of DNA [35]. Finally, an increasing number of studies on the possible applications of ILs for delivery of nucleic acids into the eukaryotic cells has emerged in more recent years [23].

Considering the potential use of ILs as new-generation solvents and/or co-solvents for DNA, it is crucial understanding the molecular origin of the observed enhanced stability of nucleic acids in ILs, by accounting that even small differences in ionic composition of ILs can drastically change the effect on DNA properties. Several studies point out that ILs with imidazolium-based cations are efficient co-solvents of water in improving the structural stability of DNA [25,27,28,31-33,36]. The effect exerted by this class of ILs on the duplex structure of DNA is found to arise from specific interactions of the cation and anion with the minor and major grooves of nucleic acids. However, there is not a fully agreement on the driving forces that dominate this interaction mechanism between imidazolium-based ILs and DNA. For some authors [25,27,28,31,33], the dominant factors that lead to the enhancement of stabilization and preservation of DNA structure in aqueous solutions of ILs are associated to i) the DNA groove binding with IL cations through hydrophobic and polar forces and ii) the partial dehydration of DNA operated by ILs. An alternative view proposes as mechanism the semi-intercalation binding mode of the imidazolium cation with DNA, revealing also that this interaction becomes stronger as the alkyl chain length on imidazolium ring increases [32]. Another interpretation suggests that the most important contribution to the stability of DNA structure is to be ascribed to the capability of anions in imidazolium-based ILs to establish a greater number of hydrogen bonds with the nucleobases of DNA than the cations [26]. Overall the studies mentioned above evidence the need to rationalize the interaction properties of ILs components, i.e. cations and anions, with nucleic acids to predict the efficacies of aqueous solutions of ILs for DNA solvation and stabilization.

In the present work, we implement a joint combination of advanced spectroscopic techniques such as synchrotron-UV Resonance Raman spectroscopy (SR-UVRR) and molecular dynamics (MD) simulations for investigating structure-specific interactions between imidazolium-based ILs and a 30-base pair double-strand DNA structure. Preliminary experimental studies performed on large nucleic acid molecules dissolved in ILs/water solutions [37-40] addressed the type and the strength of network interactions established between ILs and DNA molecules, proposing a possible mechanism of the cation- and anion-mediated structural stabilization of nucleic acids. Moreover, the thermal stability of DNA has been found to increase as a function of concentration of 1-butyl-3-methylimidazolium chloride [BMIM]Cl [38]. The present study aims to clarify the sequence and structural specificity of the strong binding interactions (electrostatic, hydrophobic, H-bonds) between the ILs and phosphate groups and nucleobases in the DNA minor and major grooves, beside to address the formation of peculiar nucleic acid structures in hydrated ILs. Multi-wavelength UV Resonance Raman (UVRR) spectroscopy enables to measure experimental quantities directly related to pair hydrogen bond strength and base stacking forces in nucleic acid strands [37-39,41,42]. The fine tuning of the excitation wavelength achievable by synchrotron radiation (SR) source gives UVRR technique a special sensitivity to both the local and global DNA conformational changes. This allows to efficiently monitor local events such as base mobility or to probe intermediated structural states involving dangling ends of DNA sequence that are more exposed to the interaction with cation and anions of ILs [37-39]. In this study, the experimental outcomes from SR-UVRR spectroscopy are supported and further completed by molecular dynamics simulation simulations carried out on the same double-strand DNA structure used for Raman experiments. MD simulations are used for resolving scientific problems that would be difficult (if not impossible) to study experimentally and light up the invisible microscopic details of experiments and explain the results. In the present work, DNA structure along the simulation trajectories is analyzed in the presence of ILs and compare with its crystal structure to investigate the structure and the groove dimensions of DNA. Furthermore, the binding characteristics of ILs to DNA are studied to better clarify the binding pattern of ILs to DNA.

Materials and methods

Chemicals and sample preparation
Both fully complementary oligonucleotides (sequence of strand 1: AAC CCA GAT GTC CTA CAG GAT AGC TCG CAG; 53 % of GC pairs, without 5-phosphate termination, 9184.94 Da) were synthesized by the company VBC Genomics (Vienna, Austria). The double-strand DNA (dsDNA) was prepared to 100 μM duplex concentration in Tris buffer 10 mM at pH 7.4, heated for 5 minutes at 90 °C and slowly cooled down to room temperature. The formation of the double-strand structure has been checked through circular dichroism measurements using a spectropolarimeter JASCO J-810. The ionic liquids 1-methylimidazolium chloride [MIM]Cl, 1-ethyl-3-methylimidazolium chloride [EMIM]Cl, 1-butyl-3-methylimidazolium chloride [BMIM]Cl and 1-butyl-3-methylimidazolium bromide [BMIM]Br (see Fig. S1 for chemical structures of IL) were acquired from IoLiTec with a purity of 99%. For the main purpose of this work, the procedure of water removal was not critical. However, in order to know the starting water content of ILs before the dilution, all the ILs have been dried inside a desiccator under vacuum with phosphorus pentoxide for 48h at room temperature. After the treatment the water content of all the ILs was ca. 100 ppm (Karl Fischer), which we assumed to be a reasonable level in view of the further dilution. For the preparation of dsDNA/IL samples, each IL has been added

39

to the solution of dsDNA at 100 µM and diluted with Tris buffer solution 10 mM at pH 7.4 to reach the final concentration of 54 mM of IL and 10 µM of dsDNA, corresponding to about 177 molecules of IL for each base-pair of DNA. This concentration of ILs has been chosen on the basis of previous Raman investigations carried out on large DNA molecules [38] that evidenced a stabilization effect exerted by methylimidazolium-based IL on DNA starting from about 80 molecules of IL for each base pair. All the solutions were freshly prepared for UVRR measurements and they appeared limpid before the running of experiments and after the thermal heating.

UVRR measurements and analysis of spectra

UVRR spectra were collected by exploiting the synchrotron-based UVRR set-up available at the BL10.2-IUVS beamline of Elettra Sincrotrone Trieste (Italy) [43]. All the DNA and DNA/IL solutions were measured in the temperature range between 291-375 K using 250 and 266 nm as exciting wavelengths. The exciting wavelength at 250 nm was set by regulating the undulator gap and using a Czerny-Turner monochromator (Acton SP2750, Princeton Instruments, Acton, MA, USA) equipped with a holographic grating with 1800 groves/mm for monochromatizing the incoming synchrotron radiation. The excitation wavelength at 266 nm was provided by a CryLas FQSS 266-Q2, Diode Pumped Passively Q196 Switched Solid State Laser. Raman signal was collected in back-scattered geometry, analyzed by using a single pass of a Czerny-Turner spectrometer (Trivista 557, Princeton Instruments, 750 mm of focal length) equipped with holographic grating at 1800 g/mm and detected using a CCD camera. The calibration of the spectrometer was standardized using cyclohexane (spectroscopic grade, Sigma Aldrich). The final radiation power on the samples was kept at about 40 and 200 µW for excitation with 250 and 266 nm, respectively. Any possible photo-damage effect due to a prolonged exposure of the sample to UV radiation was avoided by continuously spinning the sample cell during the measurements. The comparison between the individual spectra acquired repeatedly for each sample showed no gradual changes to the spectra with respect to accumulation number were observed, ensuring that any sample photodegradation due to UV radiation does not occur. For each Raman spectrum, after subtraction of a flat baseline, the central wavenumber position of the peaks of interest has been estimated by fitting the spectra with a suitable number of Gaussian functions. The intensity of the bands of interest has been assessed trough an integration algorithm applied over the wavenumber region of interest.

UV-VIS measurements

UV/VIS absorption spectra were collected with a Perkin Elmer LAMBDA™ 25 UV/VIS spectrometer operating in double-beam mode and equipped with plug-n-play single cell Peltier with stirrer for the temperature control. UV-VIS spectra were recorded on the samples of dsDNA (1 µM in TRIS buffer) and dsDNA 1 µM with addition of ILs at concentration of 5.3 mM in the temperature range between 293 and 373 K with $\Delta T = 5$ K. All the solutions were freshly prepared in a rectangular quartz cell of 10 mm path-length. The UV spectra were recorded in the range from 200 to 700 nm at a scanning speed of 480 nm/min and 1 nm of bandwidth.

Molecular dynamics simulations

For performing the MD simulations and quantifying the interaction of DNA with the ILs ([MIM]Cl, [EMIM]Cl, [BMIM]Cl, [BMIM]Br) in the aqueous solutions, the General Amber Force Field (GAFF) [44] was used for DNA and the imidazolium-based ILs. It is worthy to mention that the general accuracy of GAFF in the case of ILs solvents was tested and GAFF has been widely used in IL simulations for years. For example, Sprenger and his coworkers [45] examined the accuracy of the generic AMBER force field for the case of ionic liquids. In their study,

thermodynamic and transport parameters of a collection of 19 room-temperature ionic liquids were calculated using molecular dynamics and compared to the experiment. According to the results, GAFF can reproduce these properties with good accuracy when compared to experiment and with similar accuracy when compared to other published force fields. In another study, Picalek et al [46] did the molecular dynamics investigation of the interfacial structure of aqueous solutions of 1-butyl-3-methylimidazolium tetrafluoroborate. Both nonpolarizable and polarizable force fields for aqueous solutions of ILs were used to explain the anomalous dependence of the surface tension on concentration. The general GAFF parameter set was used to provide a good description of the surface properties of the pure IL. In addition, Jiang et al. [47] did MD simulations using both electronically nonpolarizable and polarizable models to analyze an energetic IL, 1-hydroxyethyl-4-amino-1,2,4-triazolium nitrate (HEATN). The GAFF was used for the nonpolarizable model. Their findings revealed a link between molecular structure, dynamics, and other physical properties for this class of IL, which matched the experimental results. In this work, a total number of 67 molecules cation and 67 molecules of anion were added randomly to reach the desired IL concentrations (54 mM) in a cubic box with dimension 12.7×12.7×12.7 nm, where the box later solvated by water molecules. Packmol package was used for random distribution of the salts in the simulation boxes [48, 49]. Since the salts and water molecules were added to the simulation box at random, certain undesirable interactions might arise in the systems, necessitating minimization. In this study, the steepest descent minimization approach was utilized to eliminate all unfavorable interactions. After minimization, all systems were equilibrated by performing 100 ps NVT (Canonical ensemble) restrained simulations followed by 100 ps NPT (isothermal–isobaric ensemble). Equilibration proceeded with the production runs where the linear constraint solver (LINCS) algorithm [50] was employed for all bonds involving hydrogen atoms and short range non-bonded interactions were cut off by 1.2 nm. Long-range electrostatic interactions were treated by the particle mesh Ewald method [51] procedure. For the production of initial velocities, Maxwell–Boltzmann distribution was used for all simulations. V-rescale coupling algorithm was used [52] with the coupling constant of 0.1 ps to ensure constant temperature and pressure during the simulations. MD production runs were performed in NPT ensemble for 100 ns at 300K where 2 fs time step was used. Data for further analysis were stored in every 5 ps for all simulations. Gromacs 2018 program package was used for performing MD simulations [53-57]. Also, for visualizations and preparation of snapshots [58], Visual Molecular Dynamics (VMD) was used. After the simulation, some strategies including radial distribution function (RDF) and root mean square deviation (RMSD) [59] were done to extract relevant information about the system. In details, the RDF is used to describe the distribution of solvent molecules around one specific molecule or atom. Also, the RMSD is computed to show the deviations of the backbone atoms of dsDNA from its initial structure and represents how structures and parts of structures alter over time as compared to the starting point.

Results and discussion

Local and cooperative structural transitions of guanine residues in hydrated ILs
Figure 1(a)-(b) displays the temperature behavior of UVRR spectra, collected using 250 nm as excitation wavelength, for dsDNA in absence and presence of [EMIM]Cl, as an example. The panels visualize the evolution of the difference spectra obtained by subtracting the spectrum measured at lowest temperature from the Raman profiles measured at the indicated temperatures (intermediate traces in the Fig. 1(a)-(b)). UVRR spectra of dsDNA and dsDNA/[EMIM]Cl at 291 and 375 K are reported at the bottom and at the top of the Fig. 1. At the excitation wavelength of

250 nm, Raman spectra of DNA are dominated by the vibrational signals arising from guanine dG bases [37, 38,41, 60, 61], such as the prominent modes dGI ∼ 1483 cm⁻¹ and dGII ∼ 1582 cm⁻¹ labelled in Fig. 1(a). Both these signals are sensitive structural markers of base stacking interactions and hydrogen-bonds (H-bonds) involving the guanine residues [62-64]. This is mainly due to the strong in-plane character of these vibrational modes that are attributed to the N7=C8 and C8-N9 ring stretching coupled with C8-H in-plane deformation of dG purine group (dGI mode) [60,62,65,66] and to the N3-C4, C4-C5 and C5-N7 stretching motions of the same purine moiety (dGII mode) [63,65,67] (for the numbering of atoms of nucleobases see Figure S2). The Raman signals arising from purine residues of DNA include also the broad band at ∼ 1332 cm⁻¹ (Fig. 1(a)) that results from the overlap between base ring vibrations assigned to adenine dA and guanine dG residues [62, 66].
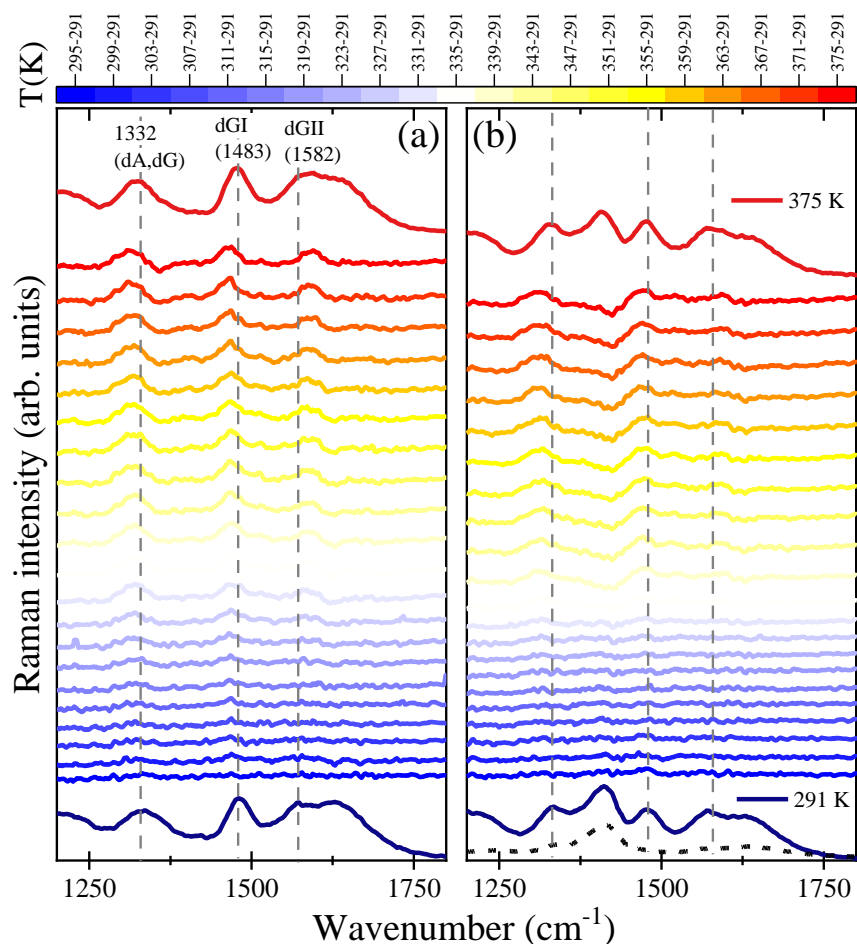

Figure 1: 250 nm-excited Raman spectra of dsDNA (10 μM) (a) and dsDNA in [EMIM]Cl/Tris (b) collected at 291 K (bottom trace) and 375 K (top trace); intermediate traces are the difference spectra computed by subtracting the spectrum measured at the lowest temperature from the spectrum at the indicated temperatures. The spectrum of [EMIM]Cl/Tris solution is also reported (dashed line in panel b).

The UVRR spectra reported in Fig. 1(b) clearly show that the main Raman bands assigned to dsDNA are well discernible also in the sample of DNA dissolved in aqueous solution of IL, with a minor spectral contribution attributable to the Raman signal of the ionic liquid.

In the wavenumber region 1200-1800 cm^{-1}, many perturbations are observed in the 250 nm-excited UVRR spectra of dsDNA and dsDNA/[EMIM]Cl as the temperature is raised, in terms of change in intensity and frequency of the main Raman bands (Fig. 1). This is well evidenced by the temperature trend observed for the Raman difference spectra which reveals a remarkable increase in intensity of the Raman bands at ~ 1332, 1483 and 1582 cm^{-1} as a function of temperature. The intensity recovery of the mode dGI ~ 1483 cm^{-1} (Raman hyperchromic effect) is largely associated to i) the H-bonds breaking and base unstacking and to ii) local structural changes, such as reversible rupture or weakening of H-bonds as well as the bases tilting that specifically involve guanine residues in the structure of DNA [37,64-66, 68-71]. The thermal pathway for dGI Raman band of dsDNA is reported in Fig. 2 and it shows i) a reversible increase in intensity at low temperature (i.e. the peak observed at ~ 299 K) and ii) a sharp transition detected at higher temperature (about 330 K, inflection point of the curves).
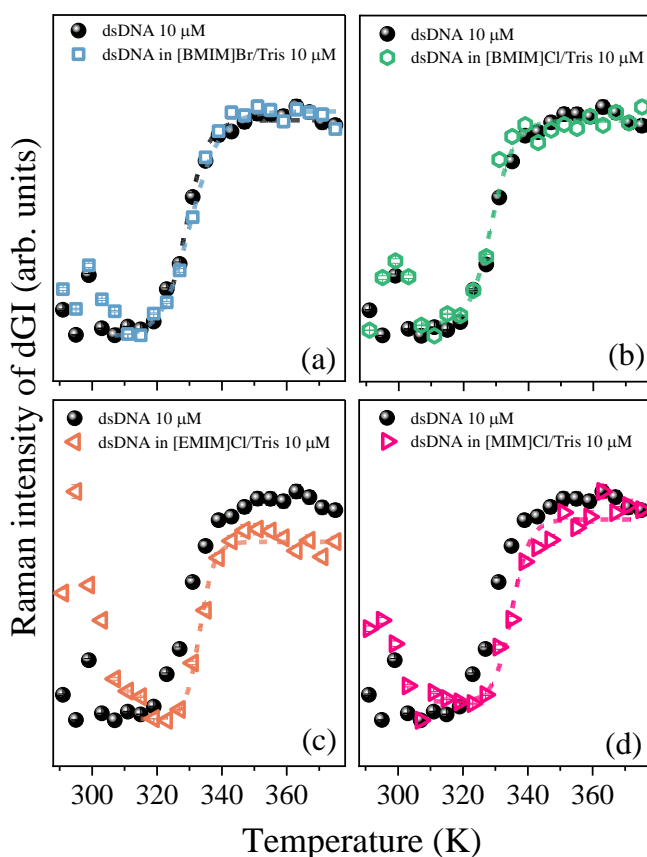

Figure 2: Melting profile for Raman band dGI of dsDNA in absence and presence of ionic liquids: (a) [BMIM]Br, (b) [BMIM]Cl, (c) [EMIM]Cl and (d) [MIM]Cl. All the plots have been normalized to the minimum and the maximum values for a better comparison. Dashed lines are fitting of the experimental data by using eqn. (1), see details in the text.

The latter sudden increase of resonance Raman band dGI finds correspondence in the marked hyperchromicity detected in the UV absorbance melting curve of dsDNA at the temperature of ~ 327 K (Fig. S3). Since the increase of optical density of DNA is directly connected with the disturbance of stacking interactions between bases, the marked increment of dGI band intensity may reflect the cooperative structural perturbation of guanine bases associated to the helix to coil transition (melting) of dsDNA promoted by the increment of temperature [37-39,41,63,64,69,70]. This dG structural transition probably entails a progressive partial disruption of guanine stacking promoted by the increment of temperature. The disappearance of Raman hyperchromicity observed for dGI band of dsDNA at high temperature (Fig. 2) indicates that no further changes in the DNA secondary structure involving guanine residues are detected in this temperature region [69].

The cooperative character of the dG transition detected in Fig. 2 is supported by the characteristic two-state profile exhibited by Raman intensity of dGI band above 310-320 K that can be satisfactorily fitted by a sigmoidal function:

$$I(T) = \frac{A + B \, exp\left(\frac{\Delta H_G}{R}\left(\frac{1}{T_{G_{coop}}} - \frac{1}{T}\right)\right)}{1 + exp\left(\frac{\Delta H_G}{R}\left(\frac{1}{T_{G_{coop}}} - \frac{1}{T}\right)\right)} \tag{1}$$

In eqn (1), A and B define the lower and upper limit of ordinate (Raman spectral band intensity), R is the gas constant and ΔH_G and $T_{G_{coop}}$ are the enthalpy variation and the transition temperature associated to the structural process involving dG bases. By fitting the data of Figure 2 to eqn (1) the cooperative dG transition temperature $T_{G_{coop}}$ for dsDNA in absence and presence of various imidazolium-based ILs (see values reported in Table 1) can be extracted with a relative good precision.

Table 1: Cooperative transition temperature $T_{G_{coop}}$ associated to partial disruption of guanine stacking estimated for dsDNA in absence and presence of ILs. The $T_{G_{coop}}$ values have been obtained by fitting the experimental UVRR data of Fig 2 to eqn (1). The melting temperatures T_m calculated by UV absorbance experiments (data shown in Fig. S3) are reported for dsDNA in Tris solution and in presence of [BMIM]Cl and [EMIM]Cl in the right column of the Table.

	$T_{G_{coop}}$ (K)	T_m (K)
dsDNA	329 ± 1	326.7 ± 0.5
dsDNA/[BMIM]Br	330 ± 1	
dsDNA/[BMIM]Cl	329 ± 1	327.0 ± 0.5
dsDNA/[EMIM]Cl	333 ± 1	328.3 ± 0.5
dsDNA/[MIM]Cl	335 ± 1	

The thermal paths of Fig. 2 and the $T_{G_{coop}}$ data of Table 1 clearly reveal the different effect of ionic liquids on the thermally-activated structural changes localized on guanine bases of dsDNA. This is observed in the form of higher $T_{G_{coop}}$ transition temperature found for dsDNA in the presence of [EMIM]Cl and [MIM]Cl. Such a finding can be explained by the formation of a preferential interaction between the cations of imidazolium-based ILs and the guanine residues on DNA

grooves that probably affect the double helix thermal structure stability [25,27,28,31,33]. This is also consistent with the significant number of H-bonds that were found to exist between the oxygen and nitrogen of guanine and oxygen of thymine as acceptors and the activated C-H bonds of the imidazolium ring as donors [25]. Conversely, the similar temperature-dependence of dGI band observed for dsDNA in buffer and in aqueous solutions of [BMIM]Cl and [BMIM]Br suggests a comparable reduction in the extent of base stacking interactions along all the stages of the melting transition in the case of these ILs.

Interestingly, it has to be remarked that the UV Raman intensity of dGI band selectively detects cooperative structural changes that are specifically localized on guanine-pairs during the melting of dsDNA [37,38,41]. This is evident by the comparison between the $T_{G_{coop}}$ values and the melting transition temperatures T_m calculated by UV absorbance experiments and reported in Table 1. Only a slight increment of the melting temperature (about 1.5 K) is observed for dsDNA dissolved in [EMIM]Cl solution with respect to Tris buffer, while the corresponding variation of $T_{G_{coop}}$ is about 4 K for the same system (see Table 1). This supports the interpretation of the guanine transition temperature detected by UVRR as a process involving cooperative conformational changes specifically localized on dG base tracts of DNA, differently from the average melting process probed by UV absorption of DNA.

The $T_{G_{coop}}$ increment observed in the presence of cations with shorter alkyl-chain length on the imidazolium ring, i.e. [EMIM]Cl and [MIM]Cl can be explained on the basis of recent experimental and simulation results indicating increasing charge delocalization in the imidazolium cation with increasing length of the alkyl chain [72-74]. We can argue that such a charge delocalization on imidazolium ring may lead to weakening of electrostatic interaction between dsDNA backbones and -[BMIM]$^+$ with respect to the case of -[EMIM]$^+$ or -[MIM]$^+$, in turn leading to the different stabilization effect on the structure of DNA. The increment of $T_{G_{coop}}$ found for short alkyl chain imidazolium cations corroborates the previous outcomes obtained on large DNA molecules hydrated in imidazolium-based ILs [39] and is opposite to the results reported by Liu et al. [32] that suggest the establishment of stronger intercalating interactions with DNA upon the increasing the length of the alkyl side chain in imidazolium cations. Our findings seem to support the conclusion of a predominance of groove binding mechanism between IL cations and DNA [21,25,27,28,31,33] instead of semi-intercalation [32].

In addition to the cooperative transition discussed above, the temperature profile for Raman band dGI of dsDNA shows a temperature-dependent increase of the intensity at about 299 K (Fig. 2) that clearly departs from the idealized two-state transition behavior detected by $T_{G_{coop}}$. This trend has been associated to the typical signature of non-cooperative structural changes occurring prior the melting of DNA, i.e. pre-melting transformations already observed in oligonucleotides and large DNA molecules [37,64,67,69,70,75]. The substantial independence from temperature of the UV absorbance of dsDNA in the pre-melting region (Fig. S3) confirms the localized nature of these conformational changes of dG residues detected by UVRR. The pre-melting observed for dsDNA at about 299 K is probably associated to structural changes such as enhanced base mobility and reversible rupture or weakening of interbase H-bonds that perturb but not destroy the guanine stacking interactions [64,76]. We can argue that the pre-melting transition detected by UVRR is associated to a conformational adjustment of the phosphate backbone of dsDNA induced by a partial disruption in the layer of hydration shell around double helix that affects both backbone helical geometry and inter-base interactions [75]. Interestingly, the plots in Fig. 2 point out that the presence of [EMIM]Cl and [MIM]Cl notably reduces the pre-melting temperature of dsDNA.

This can be better detected by looking at the plots of the first-order derivative of the temperature profiles of dGI intensity for dsDNA in absence and presence of ILs reported in Fig. S4. The maxima found in the temperature derivatives of Fig. S4 correspond to the inflection points of the two-step trend of dGI band observed for T$\gtrsim$310 K (i.e. $T_{G_{coop}}$ values reported in Table 1), while the points at which derivative changes sign mark the pre-melting temperature characteristic of each analyzed system. It can be clearly noted that for dsDNA dissolved in [EMIM]Cl and [MIM]Cl solution the pre-melting temperature of dG bases reduces from 299 to 295 and 293 K, respectively. This finding further supports the hypothesis of a stronger interaction between the imidazolium cations with shorter alkyl-chain length -[EMIM]$^+$ and -[MIM]$^+$ and the guanine residues in the structure of dsDNA, as confirmed also by MD simulations results (see in the following).
Fig. 3 displays the temperature-dependence of the wavenumber position for the Raman bands at $\sim$ 1483, 1582 and 1332 cm^{-1} for dsDNA in presence and absence of ILs.
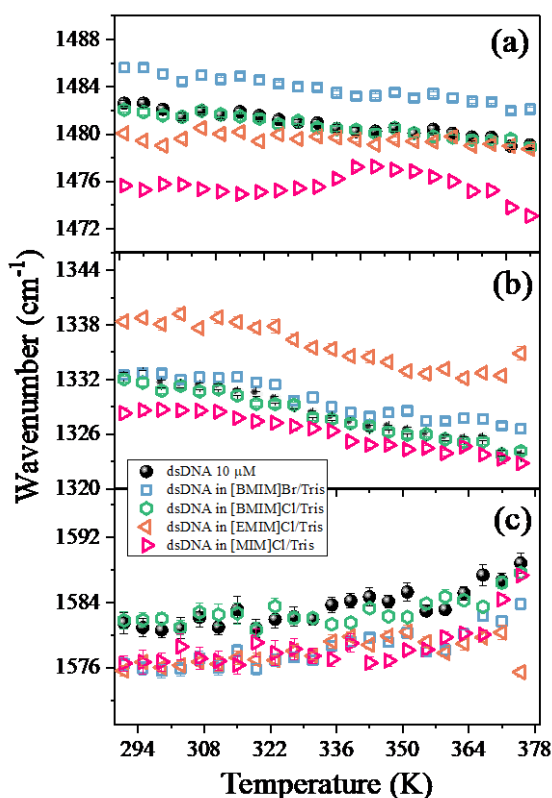

Figure 3: Temperature evolution of central wavenumber position of the Raman bands at $\sim$ 1483 (dGI) (a), $\sim$ 1332 (dA,dG) (b) and 1582 (dGII) (c) for dsDNA in absence and presence of ILs. The plots have been derived from UVRR spectra collected using 250 nm as excitation wavelength.

The red-shift of the dGI mode (Fig. 3(a)) with increasing T reflects the formation of stronger H-bonds on N7 site of dG [37,38,66]. This effect can be ascribed to the progressive substitution of base-base H-bonds with base-water H-bonds, promoted by the increment of thermal motion, that might lower the frequency of dGI mode. Remarkably, the presence of [MIM]Cl induces a significant further red-shift of the dGI band with respect to the buffer solution, over all the explored T range (Fig. 3(a)). This finding is consistent with the "dehydration" effect operated by the ionic liquid [MIM]Cl on the structure of the duplex [25,27], whose cation experiences stronger

interactions with the H-bonding sites of guanine with respect to water. Other Raman bands with predominant imidazole ring character are diagnostic of nucleoside conformations in DNA, such as the prominent signal at 1332 cm^{-1} observed in the spectrum of dsDNA [66, 60]. This band is found to downshift with the increment of the temperature for dsDNA, as shown in Fig. 3(b). Interestingly, we observe a stronger perturbation exerted by [EMIM]Cl with respect to the other ILs on the thermal pathway of the signal at 1332 cm^{-1} that appears overall blue-shifted with respect to the other systems. This latter effect can be ascribed to the sensitivity of the Raman band at ~ 1332 cm^{-1} to the local changes involving both dG and dA residues [60, 62]. Similarly, the upshift revealed for the frequency position of the Raman band dGII of dsDNA as a function of temperature (Fig. 3(c)) is closely related to the partial disruption of guanine stacking occurring during the cooperative transition detected for dsDNA at about 330 K [37]. The reinforcement of the double bonds of the guanine ring reflects the transition from double- to single-stranded structure of DNA during the melting, occurring both in absence and presence of ILs (see Fig. 3(c)).

Intermediate conformational states of dA-dT residues in hydrated ILs
The analysis of the UVRR spectra collected using 266 nm as excitation wavelength provides specific information on the thermally-induced conformational changes of adenine dA and thymine dT residues in dsDNA. Fig. 4 displays the temperature evolution of 266 nm-excited UVRR spectra for dsDNA in absence and presence of [EMIM]Cl, as an example.
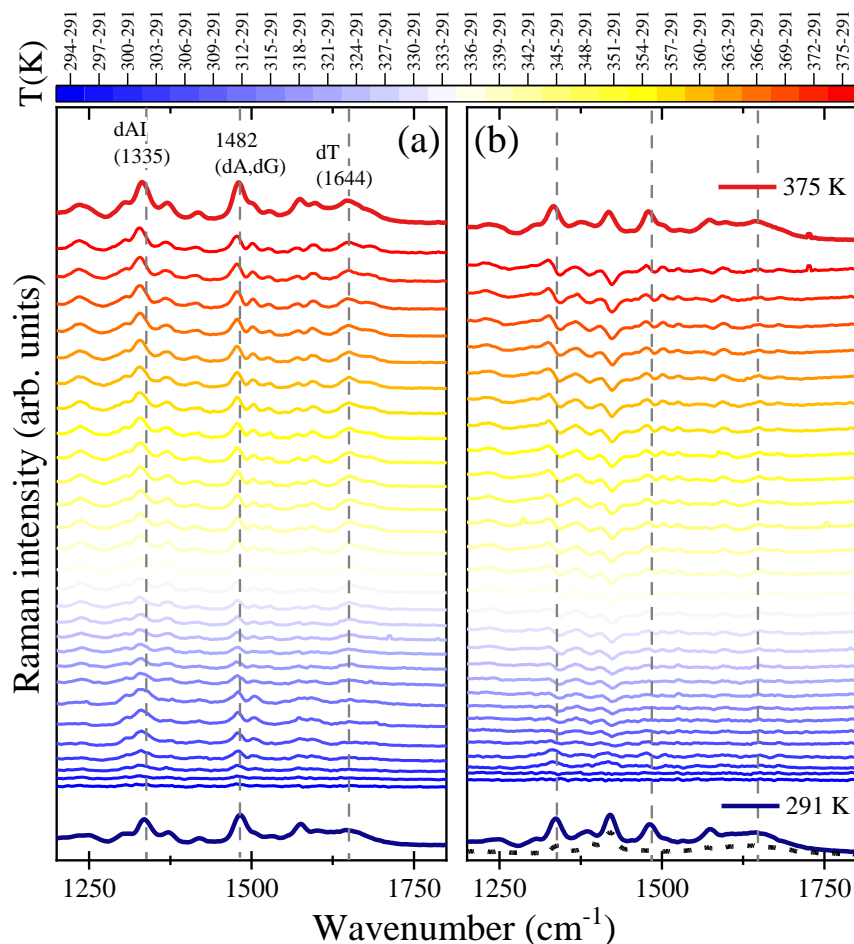
Figure 4: 266 nm-excited Raman spectra of dsDNA (10 μM) (a) and dsDNA in [EMIM]Cl/Tris (b) collected at 291 K (bottom trace) and 375 K (top trace); intermediate traces are the difference spectra computed by subtracting the spectrum measured at the lowest temperature from the spectrum at the indicated temperatures. The spectrum of [EMIM]Cl/Tris solution is also reported for comparison (dashed line in panel b).

The Raman difference spectra reported in Fig. 4 evidence remarkable temperature-induced changes in intensity and frequency of the Raman bands of dsDNA at ~ 1335, 1482 and 1644 cm^{-1}. The signal at ⌣1335 cm^{-1} (dAI) is attributed to the coupled stretching vibrations of N7=C8 and C5- N7 bonds of adenine dA [60,77,78]. This mode is sensitive to dA nucleoside conformation [69] and to the changes of H-bonds at the acceptor site N7 of adenine [67,79]. At the excitation wavelength of 266 nm the signal at ⌣ 1482 cm^{-1} contains comparable contributions arising from dA and dG residues [37]. The signal labelled as dT ~ 1644 cm^{-1} is attributed to coupled stretching of C4=O and C5=C6 bonds of thymine dT residue and it is particularly reflective of any perturbations occurring at the C=O site of dT base [70,80,81] (see Fig. S1 for the numbering of atoms). The comparison between UVRR spectra of dsDNA in absence and presence of ILs (Fig. 4(a)-(b)) suggests that the DNA duplex follows different thermal pathway when it is in hydrated ILs. This can be well rationalized by looking to the temperature dependence of the intensity of dAI band. Fig. 5 shows the evolution of the Raman hyperchromism for the signal dAI ⌣ 1335 cm^{-1} that, similarly to the dGI band intensity, reflects the partial unstacking of dA bases during the melting of DNA.
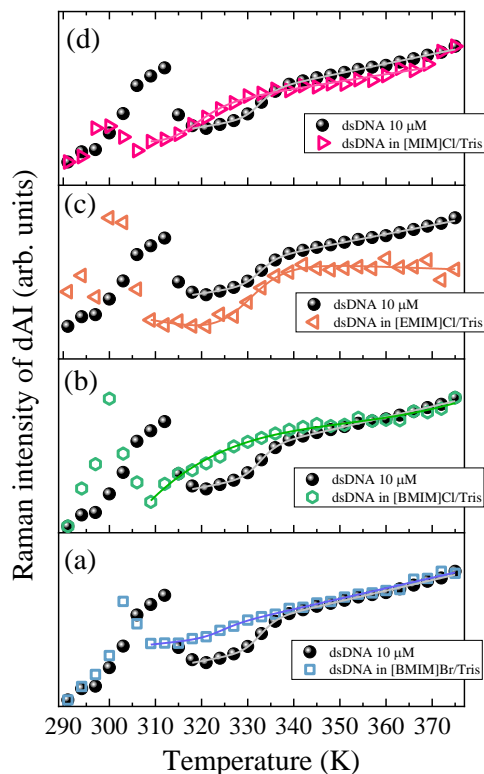

Figure 5: Melting profile for Raman band dAI of dsDNA in absence and presence of ionic liquids: (a) [BMIM]Br, (b) [BMIM]Cl, (c) [EMIM]Cl and (d) [MIM]Cl. All the plots have been normalized to the minimum and the maximum values for a better comparison. Full lines are fitting of the experimental data by using eqn. (2), see details in the text.

As first remark, the intensity of dAI band of dsDNA exhibits a temperature dependence that slightly departs from the ideal two-state behavior typical of the cooperative transition detected, in

49

the same temperature range, for dGI band (see Fig. 2). The trend reported in Fig. 5 for dAI band indicates that even rather small temperature variations may give rise to local conformational changes that primarily involve A-tracts in the structure of dsDNA [37,64,70,75]. More quantitative information on the structural modifications and on the thermodynamic parameters associated to each step of the process experienced by dA residues in absence and presence of ILs can be traced back by the first-order derivative of the temperature profiles of dAI intensity (Fig. S5). The trend of derivative curves evidences, for all the analyzed systems, a reversible pre-melting transformation detected for temperature below 315 K and a more cooperative transition occurring at higher temperature $T_{A_{coop}}$. The monoatomic dependence on temperature of the dAI band above 315 K suggests the occurrence of a simple two-stage structural process involving adenine-pairs during thermal pathway of sDNA, differently from the multiple intermediate stacking arrangements detected for dA in large molecules of DNA [39]. This cooperative transition probably involves a partial disruption of the adenine staking interactions that precedes the separation of DNA strands during the melting. The values of $T_{A_{coop}}$ for dsDNA in absence and presence of ILs can be estimated by fitting of the experimental trends reported in Fig. 5 with a similar two-state law:

$$I_{dAI}(T) = \frac{C + m_C \cdot T + (D + m_D \cdot T) \cdot e^{\frac{\Delta H_A}{R}\left(\frac{1}{T_{A_{coop}}} - \frac{1}{T}\right)}}{1 + e^{\frac{\Delta H_A}{R}\left(\frac{1}{T_{A_{coop}}} - \frac{1}{T}\right)}}$$

(2)

where C and D represent the lower and upper limit of ordinate (Raman spectral dA band intensity), R is the gas constant, ΔH_A and $T_{A_{coop}}$ are the enthalpy variation and the temperature associated to the cooperative transition of adenine-pairs. The parameters m_c and m_D have been introduced in eqn. (2) to account for the linear temperature-dependence of the band intensity in the pre- and post-melting regions, respectively. The values of $T_{A_{coop}}$ for dsDNA and dsDNA/ILs are reported in Table 2 and they point out a general decrement of the dA cooperative transition temperature exerted by all the ILs considered in this study.

Table 2: Cooperative transition temperature $T_{A_{coop}}$ associated to partial disruption of adenine stacking interactions estimated for dsDNA in absence and presence of ILs. The $T_{A_{coop}}$ values have been obtained by fitting of the experimental data of Fig 5 to eqn (2).

	$T_{A_{coop}}$ (K)
dsDNA	333 ± 1
dsDNA/[BMIM]Br	324 ± 1
dsDNA/[BMIM]Cl	324 ± 1
dsDNA/[EMIM]Cl	330 ± 1
dsDNA/[MIM]Cl	318 ± 1

Fig. 6 summarizes the values estimated for the pre-melting and the cooperative transitions temperatures associated to guanine (T_G) and adenine (T_A) residues of dsDNA in absence and presence of ILs.
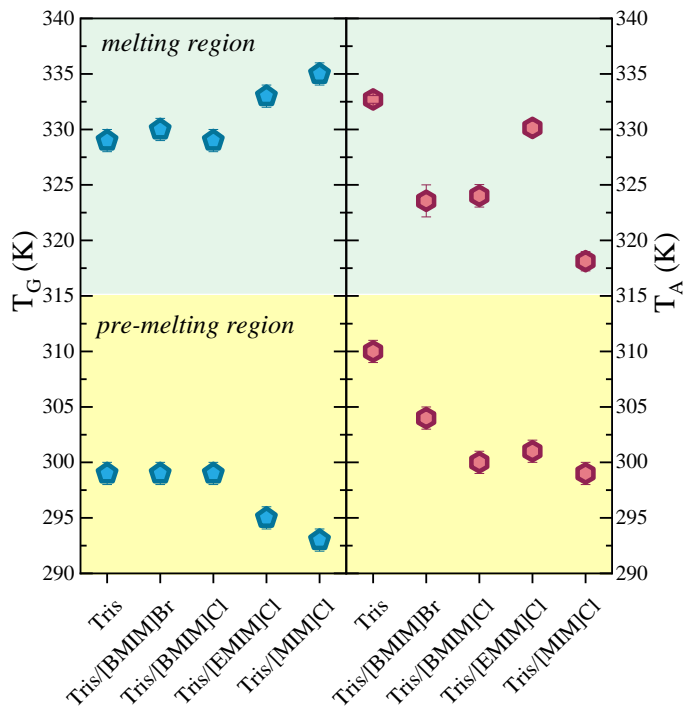
Figure 6: Estimated pre-melting and cooperative transitions temperatures localized on guanine (T_G, cyan symbols) and adenine (T_A, red symbols) residues of dsDNA as a function of the different type of solvents, i.e. Tris buffer or ILs/Tris solutions.

As first remark, we observe a notable difference in the thermally-induced behavior of guanine and adenine residues in dsDNA that are involved in cooperative structural transformations occurring at slightly higher temperature for dA with respect to dG. More interestingly, the effect on the transition temperature associated to this cooperative transformation is opposite for the two residue, i.e. an increment of T_G observed especially for ILs with shorter alkyl-chain length of imidazolium cations and a general decrement of T_A common to all the ILs.

The experimental results indicate that both dG and dA tracts in the structure of dsDNA are involved in thermally-activated reversible pre-melting conformational transformations occurring at specific temperatures below 315 K. Consistently with similar pre-melting phenomena observed in Poly(dA–dT) · poly(dA–dT) double-helical B DNA [69,70,81], the reversible increment in the dAI intensity at 310 K may be related to the stabilization of extra amount of propeller twist between the A-T base planes through the formation of a third hydrogen bond cross-strand between consecutive dA - dT pairs [70]. Interestingly, Fig. 6 points out that the presence of all the considered ILs induces a notable reduction of the characteristic temperature associated to the pre-melting transformation of dA bases in dsDNA with a more marked affect detected for ILs with chloride as anion. This finding can be rationalized by taking into account the predicted binding capability of ions with the minor groove of DNA that determines DNA deformations, such as AT-tract bending [82,93]. The more marked affect operated by the imidazolium-based ILs with Cl$^-$ as anion suggests a selective strong interaction of this anion with the adenine-rich tracts on the structure of dsDNA. The analysis of temperature behavior of the Raman intensity of the band at ∼ 1482 cm^{-1} (dA,dG) reported in Supplementary information section (Fig. S6) confirms the stronger

influence operated on the temperature of pre-melting of dA tracts by ILs with Cl⁻ as anion with respect to Br⁻.

In the wavenumber region 1300-1500 cm^{-1}, many Raman bands of dsDNA shift to lower frequency upon the increment of the temperature, both in absence and presence of ILs. This is clearly visible in Fig. 7(a) and (b) for the signals at ∼ 1335 (dAI) and at ∼ 1482 (dA,dG).
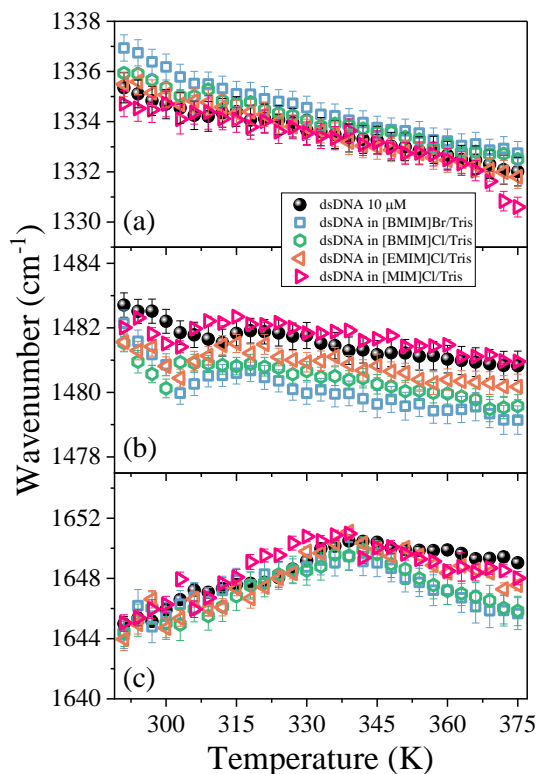

Figure 7: Temperature evolution of central wavenumber position of the Raman bands at ∼ 1335(dAI) (a), ∼ 1482(dA,dG) (b) and ∼ 1644(dT) (c) for dsDNA in absence and presence of ILs. The plots have been derived from UVRR spectra collected using 266 nm as excitation wavelength.

These Raman bands are mainly associated to vibrations arising from purine residues. The frequency of the oscillators associated to these Raman signals is sensitive to the different hydrogen bonding states on the proton-acceptor N7 site mainly of adenine residues [62,66,69,78,79]. The concerted red-shifts observed for the Raman signals in Fig. 7(a) and (b) may be explained by the progressive weakening of H-bonds at the acceptor sites N7 of adenine as the temperature is raised [69,79]. This is due to the replacement of inter-adenine hydrogen bonds with weaker adenine-water hydrogen bonds. This could be favored by the progressive exposition to the solvent of the dA residues of dsDNA during the melting. Fig. 7(a) and (b) point out no significant modifications on the frequency of the Raman bands attributed to dA induced by the presence of ILs. This could be consistent with the conclusion that the binding of anions of ILs with the minor groove of DNA especially induces the base tilting rather than the rupture of hydrogen bonds on adenine residues in A-T tracts. Fig. 7(c) displays the temperature-dependence of the wavenumber position for dT band whose strength of oscillation accounts for any perturbations occurring at C4=O site of thymine residue [60,70,79]. The marked upshift of this mode observed in the temperature region

prior the melting at ∼ 335 K can be correlated with a decrease in H-bonding strength on C=O site of thymine during the cooperative transition detected at this temperature for dA residues [37, 70]. The relative large blue-shift (about 7 cm^{-1}) observed for dT band as a function of temperature is consistent with the existence in the duplex structure of dsDNA of a cross-strand three-centered H-bonds between dA and dT bases [70]. Since the pre-melting transition is primarily attributed to changes in degree of propeller twisting and in the strength of the cross-strand three-centered H-BONDS, the data reported in Fig. 7(c) seem to suggest a negligible perturbation operated by ILs on the extent of these three-centered H-bonding.

Structure of dsDNA in hydrated ILs
By MD simulations, we analyzed the structure of the dsDNA along the simulation trajectories (100 ns) to check if the DNA could maintain its native B-conformation in the hydrated ILs considered in this study ([MIM]Cl, [EMIM]Cl, [BMIM]Cl and [BMIM]Br). The structural stability of the dsDNA was investigated by comparing the root mean square deviation (RMSD) values of DNA solvated in pure water and in the hydrated ILs solutions (Fig. 8).
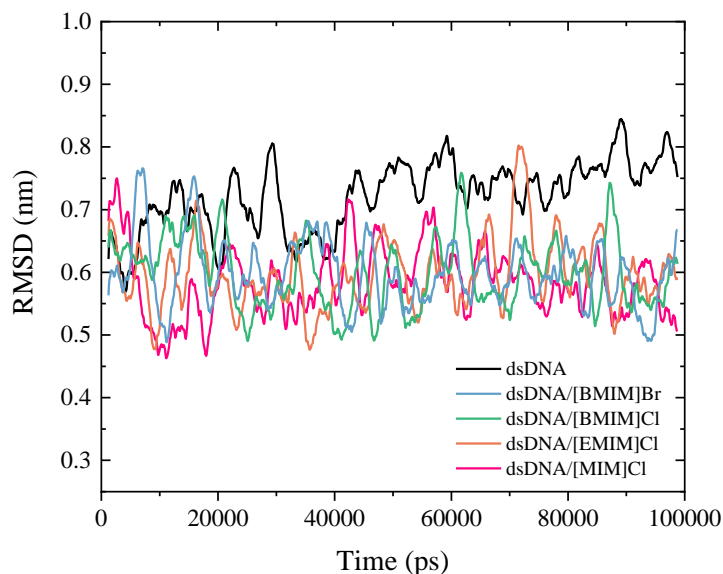
Figure 8: Root-mean-square deviation (RMSD, nm) of dsDNA solvated in the four hydrated ILs (54 mM) and in pure water.

Over the 100 ns, the average RMSD values in hydrated [MIM]Cl, [EMIM]Cl, [BMIM]Cl, [BMIM]Br and pure water are 0.582 nm, 0.596 nm, 0.598 nm, 0.598 nm and 0.721 nm, respectively. All the average RMSD values calculated for DNA in each hydrated IL were found to be lower than the value observed in the pure water solution. Furthermore, decreasing the alkyl-chain length on imidazolium cation from 1-butyl-3-methylimidazolium to 1-methylimidazolium seems to slightly decrease the average RMSD value of the DNA. This indicates that the alkyl chain lengths of the cations have a small influence on the stability of the DNA at room temperature, consistently with the experimental evidence.
Fig. 9 shows the distribution of 1-methylimidazolium cations on the surface of dsDNA. This picture illustrates that populations of cations were not only located near DNA phosphate groups due to the charge attraction but also associated with the major and minor grooves of DNA.

According to this figure, it is assumed that the cations disrupted the hydration shells and entered the minor and major grooves and remained bound to the grooves without disturbing the helical structure of dsDNA. It is supposed that the hydrogen bond between the cation-grooves might assist in stabilizing the DNA.
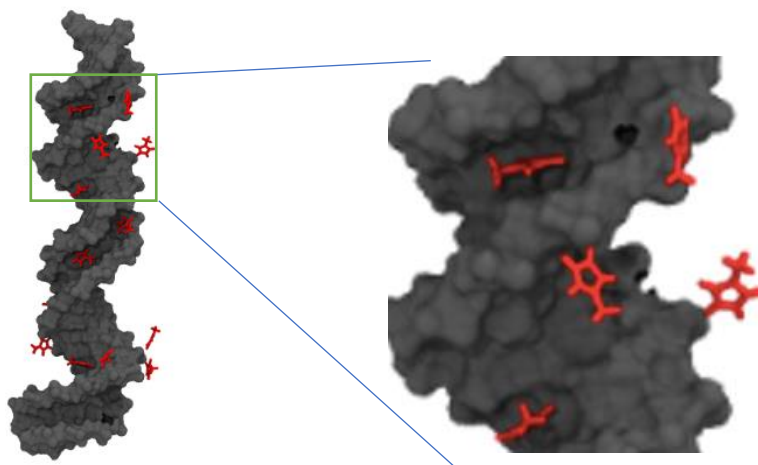

Figure 9: Representative distribution of 1-methylimidazolium cations that shows their association with the DNA phosphate groups, major and minor grooves in the aqueous solution of [MIM]Cl (54 mM). Color coding: gray, DNA; red, 1-methylimidazolium cations.

Role of hydration shells
It is assumed that the stability of DNA is mainly dependent on the water content, or more specifically, the properties of hydration shells around DNA. In fact, the hydration shells play a vital role in stabilizing or destabilizing DNA and their conformational dynamics [27]. Fig. 10 displays the distribution of 1-methylimidazolium cations and water molecules in the solvation layers of dsDNA, defined as a shell of 0.35 nm.
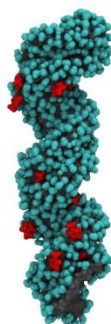
Figure 10: Representative distribution of the populations of 1-methylimidazolium cations and water molecules within 0.35 nm of DNA surface in the aqueous solution of [MIM]Cl (54 mM). Color coding: gray, DNA; cyan, water and red, 1-methylimidazolium cation.

According to this figure, 1-methylimidazolium cations penetrate the hydration layer of the DNA and take part in the solvation mechanism. As shown in Fig. 10, the cations interact with the various region of DNA, thereby the cations are trapped in the DNA. Consequently, water molecules are not able to diffuse inside the helical structure easily [25] and, the disturbing of DNA conformation by water diffusion is reduced. Such partial dehydration of the DNA by cations could also prevent hydrolytic reactions such as depurination and deamination, as previously suggested by other authors [25,27]. Moreover, the number of water molecules in DNA solvation shell as a function of the simulation time have been calculated to gain more information about the scale of water displacement by the alkyl imidazolium cations. Fig. 11 shows the number of water molecules around the major groove in the aqueous solution of [MIM]Cl, [EMIM]Cl, [BMIM]Cl and [BMIM]Br.
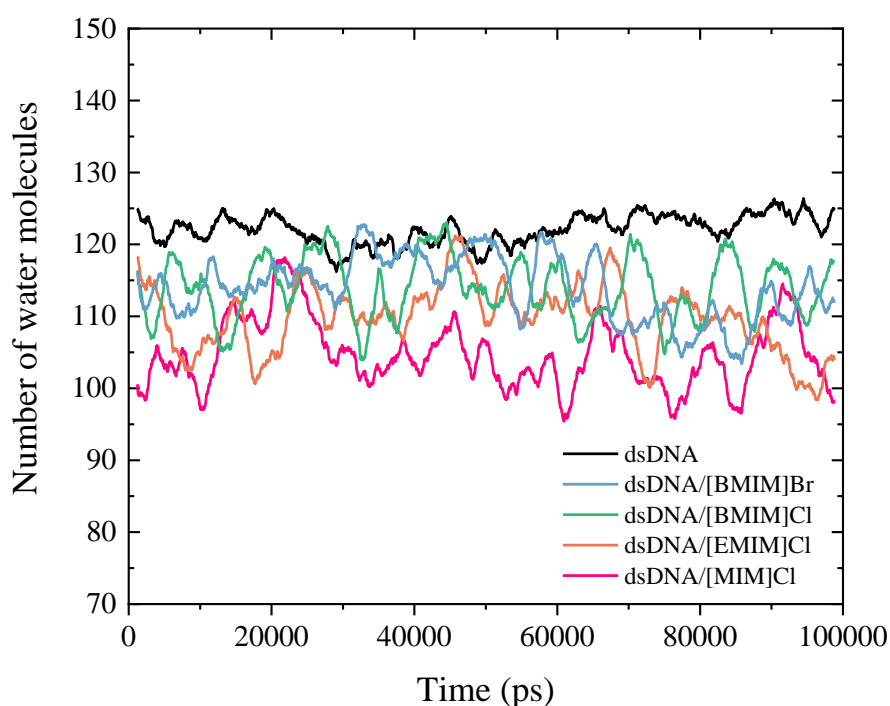
Figure 11: The number of water molecules which are present within 3.5 Å around the dsDNA major groove at different hydrated ILs (concentration of 54 mM of IL in water) throughout the simulation trajectory.

According to this plot, the number of water molecules which are present within 3.5 Å around the major groove of DNA is lowest in hydrated [MIM]Cl solution. In other words, more water molecules were stripped off by 1-methylimidazolium cations from DNA surface. This finding further supports the experimental UVRR data that suggest a stronger interaction of guanine residues in the structure of dsDNA with imidazolium cations with shorter alkyl-chain length.

Binding characteristics of ILs–dsDNA
In this study, various radial distribution function (RDFs) of ILs around DNA (major groove) were explored and compared to find the binding pattern of ILs to DNA. Fig. 12 shows the RDF of center

of mass (COM) of the imidazolium ring around the major groove of DNA in different hydrated imidazolium ILs solutions. According to this figure, the distribution of cations in the major groove is highest in the aqueous solution of [MIM]Cl, meaning the penetration of [MIM] cations into the DNA major groove. According to the Fig. 12 and prior mentioned, it is assumed that the interaction of the cationic headgroups with the DNA (the major groove) increases with decreasing alkyl chain length of the ILs. It is supposed that the interaction of shorter alkyl-chain length on the imidazolium ring ([MIM]$^+$) with major groove and partial dehydration of DNA are the key factors that stabilize DNA in hydrated ILs, consistently with the experimental UVRR results.
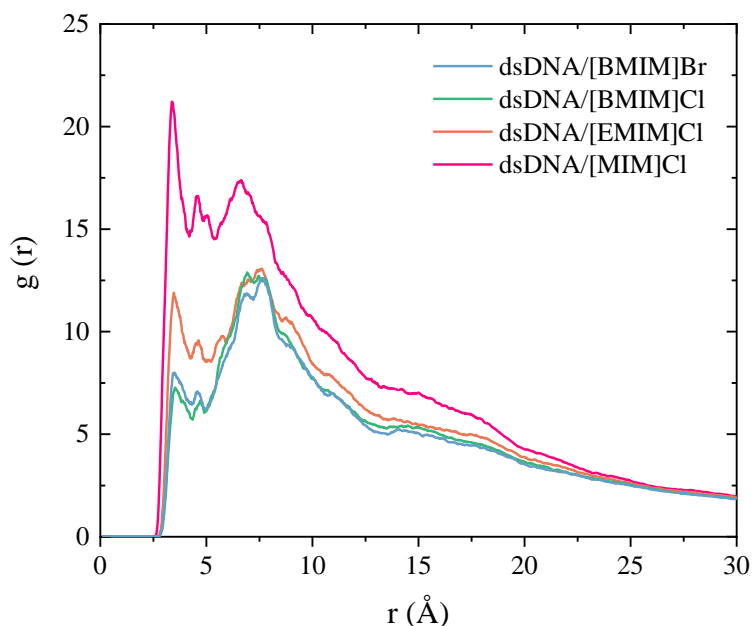
Figure12: The RDF of COM of the imidazolium ring around major groove of the DNA in different hydrated imidazolium ILs solutions (54 mM). The N7 site for the major groove was considered for calculating the RDFs.

Moreover, Fig. 12 shows that the switching chloride ion to bromide of [BMIM] ionic liquids the interaction of [BMIM] cation with major groove of dsDNA is slightly pronounced. It is worthy to mention that as DNA is a polyanion polymer, the anions are not well-distributed on the surface of DNA. Hence, the distribution of anions around the DNA was not reported in this study. However, the DNA was simulated in two hydrated [BMIM]-based ILs ([BMIM]Cl and [BMIM]Br) to investigate the effects of the anion on DNA stability. According to Fig. 11, the average number of water molecules present within 3.5 Å around the major groove of DNA in [BMIM]Br/water solution and [BMIM]Cl solution are approximately the same and no meaningful difference was observed. It is absolutely logical why no meaningful changes on number of water molecules around DNA structure in solutions of [BMIM]Br and in [BMIM]Cl were observed, because the concentration of water in the solution is more than 50 mol/L and the changes of its concentration around dsDNA due change of ions is negligible.

Summary and conclusions

The possible capability of ionic liquids in stabilizing and preserving the conformation of nucleic acids is important in the field of biology, medical diagnostics and biotechnology, especially for DNA storage and handling. Several studies predicted that aqueous solutions of ILs with cations based on imidazolium enable to improve the structural stability of DNA but the dominant mechanism of interactions between this class of ILs and nucleic acids is still to be fully understood. About this, many experimental techniques of analysis of DNA suffer from the missing of sequence specificity and are less sensitive to transitions which do not involve changes the number of closed base pairs. SR-UVRR technique takes advantage of the capability to differentiate contributions of single nucleobases interactions to the structural transformation of DNA duplexes during thermal pathway. In this work, we have implemented SR-UVRR experiments and molecular dynamics simulations for directly testing the nature of the conformational transitions along the melting pathway of a synthetic 30-base pair duplex, taken as natural DNA model, as affected by the presence of imidazolium-based ILs. Our experimental and simulation findings consistently suggest the predominance of a groove binding mechanism between the imidazolium cations and dsDNA, with a preferential interaction established between guanine residues and the imidazolium cations with shorter alkyl-chain length. This seems to be a common behavior observed for both short and large DNA molecules hydrated in imidazolium-based ILs. UVRR data evidence that even rather small temperature variations may give rise to reversible pre-melting structural transitions that involve both dG and dA tracts in the structure of dsDNA. These conformational changes, not detected by UV absorption melting curves, are associated to reversible rupture or weakening of H-bonds in the double-stranded structure as well as bases tilting that are activated at lower temperature for guanine residues with respect to adenine ones. The binding of Cl^- anions with the minor groove of DNA especially induces the base tilting rather than the rupture of hydrogen bonds on adenine residues in A-T tracts. According to the MD simulation results, electrostatic interactions drive the stronger attraction observed between the cations in the aqueous solution of [MIM]Cl to the DNA major groove. It is assumed that such partial dehydration of the DNA by cations prevents hydrolytic reactions and increases conformational stability of the DNA in comparison with other hydrated ILs.

Acknowledgments

List of abbreviations

Ionic Liquids (ILs)

Synchrotron-UV Resonance Raman spectroscopy (SR-UVRR)

Molecular dynamics (MD)

Deoxyribonucleic acid (DNA)

UV Resonance Raman (UVRR)

double-strand DNA (dsDNA)

1-methylimidazolium chloride [MIM]Cl

1-ethyl-3-methylimidazolium chloride [EMIM]Cl

1-butyl-3-methylimidazolium chloride [BMIM]Cl

1-butyl-3-methylimidazolium bromide [BMIM]Br

General Amber Force Field (GAFF)

NVT (Canonical ensemble)

NPT (isothermal–isobaric ensemble)

linear constraint solver (LINCS)

Visual Molecular Dynamics (VMD)

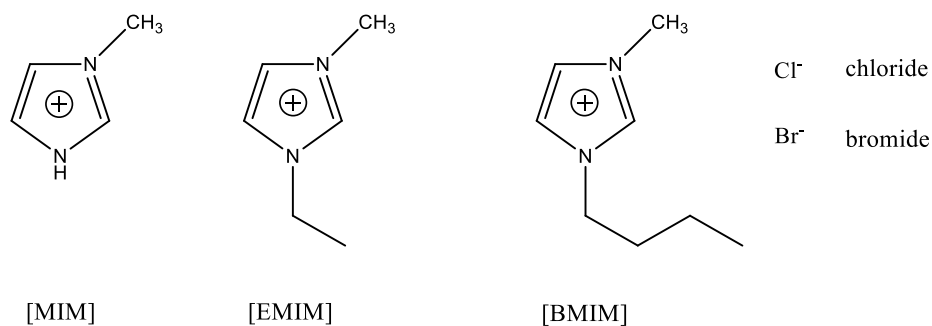Radial distribution function (RDF)

Root mean square deviation (RMSD)

Supporting Information

Cl⁻	chloride
Br⁻	bromide

[MIM]   [EMIM]   [BMIM]

Figure S1: chemical structure of Ionic Liquids (ILs) considered in this study, i.e. 1-methylimidazolium chloride ([MIM]Cl), 1-ethyl-3-methylimidazolium chloride ([EMIM]Cl), 1-butyl-3-methylimidazolium chloride ([BMIM]Cl) and 1-butyl-3-methylimidazolium bromide ([BMIM]Br).
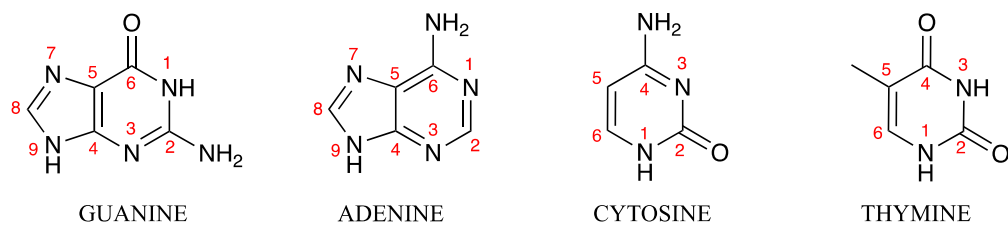
Figure S2: structure and numbering conventions adopted for nucleotides guanine (dG), adenine (dA), cytosine (dC) and thymine (dT).
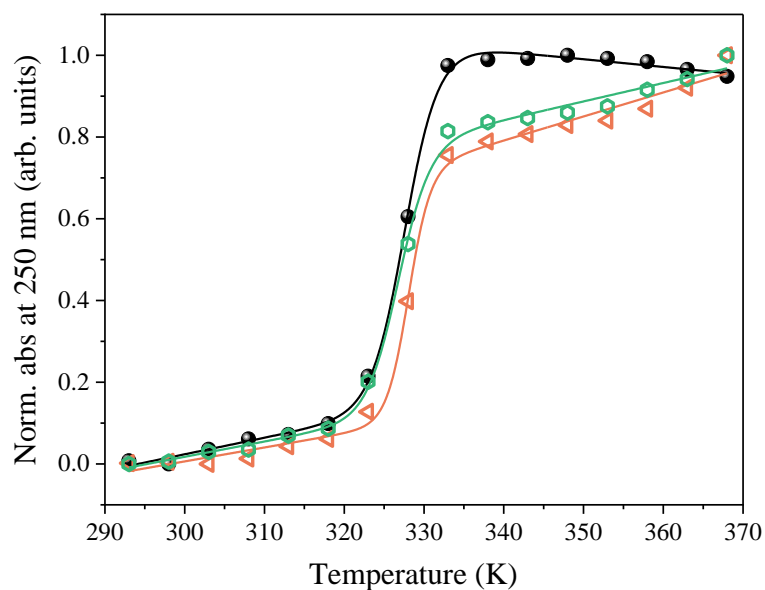

Figure S3: UV absorbance melting curves represented by absorbance at 250 nm measured during denaturation process of dsDNA in Tris buffer aqueous solution (black symbols) and in presence of [EMIM]Cl (orange symbols) and [BMIM]Cl (green symbols).
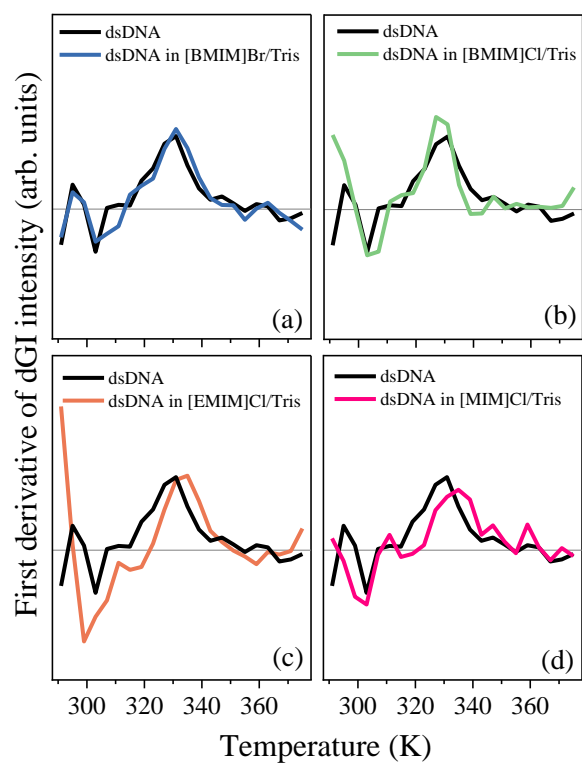
Figure S4: First derivative curves of the temperature profiles for guanine Raman band (dGI) of dsDNA in absence and presence of ILs (Fig. 2(a)-(d).
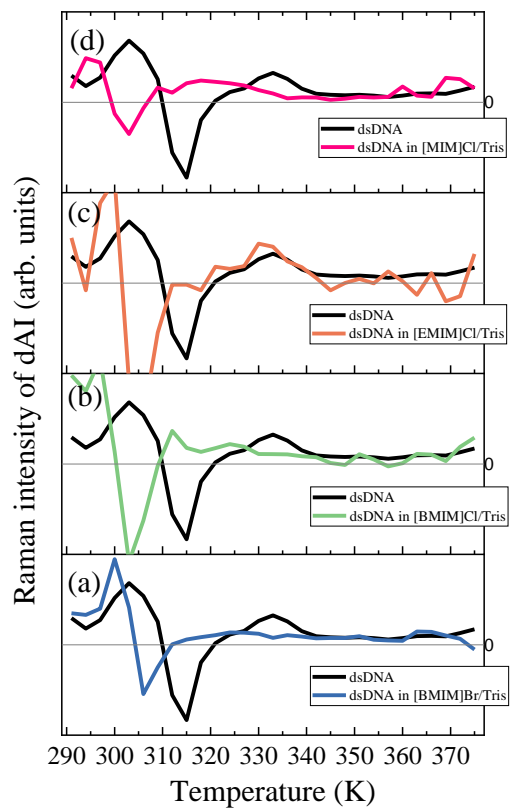
Figure S5: First derivative curves of the temperature profiles for adenine Raman band (dAI) of dsDNA in absence and presence of ILs (Fig. 5(a)-(d).
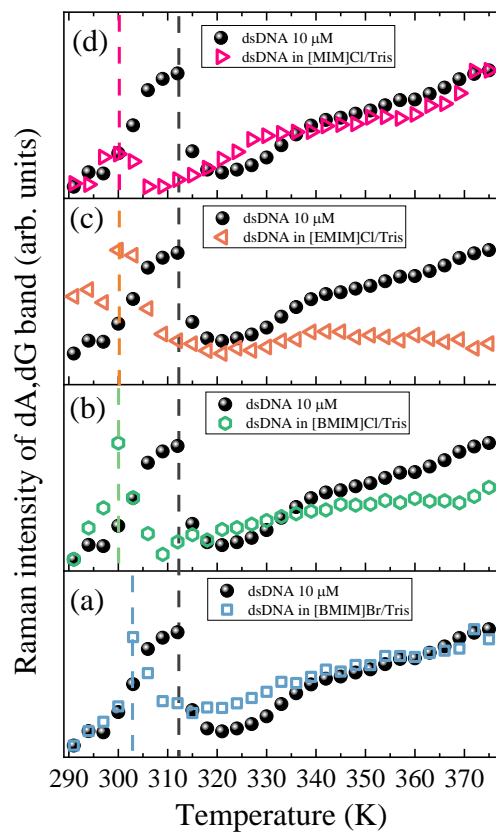
Figure S6: Melting profile for Raman band at ~ 1482 cm^{-1} (dA,dG) for dsDNA in absence and presence of ionic liquids: (a) [BMIM]Br, (b) [BMIM]Cl, (c) [EMIM]Cl and (d) [MIM]Cl. The intensities have been derived from UVRR data collected using 266 nm as excitation wavelength.
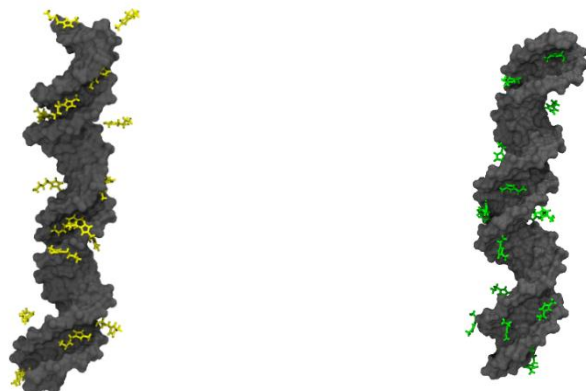
Figure S7: Representative distribution of [**BMIM**]$^+$ and [**EMIM**]$^+$ cations showing their association with the DNA phosphate groups, major and minor grooves in the aqueous solution of [BMIM]Cl and [EMIM]Cl (54mM). The distribution of **Cl**$^-$ anions was not shown here. Color coding: gray, DNA; yellow, [**BMIM**]$^+$; green, [**EMIM**]$^+$.
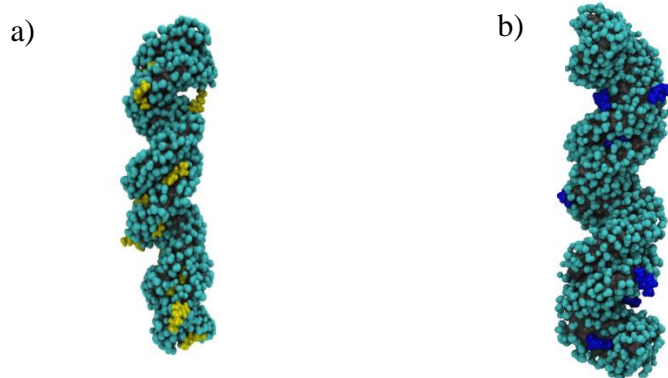
a)

b)

Figure S8: Representative populations of cations and water molecules within 0.35 nm of the DNA surface. (a) hydrated [BMIM]Cl and (b) hydrated [EMIM]Cl solutions (54 mM). Color coding: cyan, water; gray, DNA; yellow, [BMIM]$^+$ cation; blue, [EMIM]$^+$ cation.

References:

[1] E. Lattuada, M. Leo, D. Caprara, L. Salvatori, A. Stoppacciaro, F. Sciortino, P. Filetici, DNA-GEL, Novel Nanomaterial for Biomedical Applications and Delivery of Bioactive Molecules, Front. Pharmacol. 11 (2020) 01345 https://doi.org/10.3389/fphar.2020.01345

[2] H. Joshi, A. Kaushik, N. C. Seeman, and P. K. Maiti, Nanoscale Structure and Elasticity of Pillared DNA Nanotubes, ACS Nano 10 (2016) 7780-7791 https://doi.org/10.1021/acsnano.6b03360

[3] Y. Murakami, M. Maeda, DNA-Responsive Hydrogels That Can Shrink or Swell, Biomacromolecules 6 (2005) 2927–2929 doi: 10.1021/bm0504330

[4] S. D. Patil, D. G. Rhodes, D. J. Burgess, DNA-based therapeutics and DNA delivery systems: a comprehensive review, AAPS J. 7 (2005) E61–E77 doi: 10.1208/aapsj070109

[5] M. J. Heller, DNA microarray technology: devices, systems, and applications, Annu. Rev. Biomed. Eng. 4 (2002) 129–153 10.1146/annurev.bioeng.4.020702.153438

[6] O. Fedrigo, G. Naylor, A gene-specific DNA sequencing chip for exploring molecular evolutionary change, Nucleic Acids Res. 32 (2004) 1208–1213 doi: 10.1093/nar/gkh210

[7] C. Morishima, M. Chung, K. W. Ng, D. J. Brambilla, D. R. Gretch, Strengths and limitations of commercial tests for hepatitis C virus RNA quantification. J. Clin. Microbiol. 42 (2004) 421–425 https://doi.org/10.1128/JCM.42.1.421-425.2004

[8] J. Zheng, J. J. Birktoft, Y. Chen, T. Wang, R. Sha, P. E. Constantinou, S. L. Ginell, C. Mao, N. C. Seeman, From molecular to macroscopic via the rational design of a selfassembled 3D DNA crystal, Nature 461 (2009) 74–77 doi: 10.1038/nature08274

[9] R. J. Macfarlane, B. Lee, M. R. Jones, N. Harris, G. C. Schatz, C. A. Mirkin, Nanoparticle Superlattice Engineering with DNA, Science 334 (2011) 204– 208 doi: 10.1126/science.1210493

[10] T. Lindahl, B. Nyberg, Rate of depurination of native deoxyribonucleic acid, Biochemistry, 11 (1972) 3610–3618 https://doi.org/10.1021/bi00769a018

[11] W. K. Pogozelski, T. D. Tullius, Oxidative strand scission of nucleic acids: Routes initiated by hydrogen abstraction from the sugar moiety, Chem. Rev. 98 (1998) 1089–1108 https://doi.org/10.1021/cr960437i

[12] J. Cadet, T. Delatour, T. Douki, D. Gasparutto, J. P. Pouget, J. L. Ravanat, S. Sauvaigo, Hydroxyl radicals and DNA base damage, Mutat. Res./Fundam. Mol. Mech. Mutagen., 424 (1999) 9–21 https://doi.org/10.1016/S0027-5107(99)00004-4

[13] H. T. Karimata, N. Sugimoto Structure, stability and behaviour of nucleic acids in ionic liquids, Nucleic Acids Res., 42(14) (2014) 8831–8844 doi: 10.1093/nar/gku499

[14] Z. Lei, B. Chen, Yoon-Mo Koo, D. R. MacFarlane, Introduction: Ionic Liquids, Chem. Rev. 117(10) (2017) 6633–6635 https://doi.org/10.1021/acs.chemrev.7b00246

[15] A. Benedetto, P. Ballone, Room Temperature Ionic Liquids Meet Biomolecules: A Microscopic View of Structure and Dynamics, ACS Sustain. Chem. Eng. 4 (2016) 392−412 https://doi.org/10.1021/acssuschemeng.5b01385

[16] K. S. Egorova, E. G. Gordeev, V. P. Ananikov, Biological Activity of Ionic Liquids and Their Application in Pharmaceutics and Medicine, Chem. Rev. 117 (2017) 7132−7189 https://doi.org/10.1021/acs.chemrev.6b00562

[17] D. Saha, A. Mukherjee, Effect of water and ionic liquids on biomolecules, Biophys Rev. 10(3) (2018) 795-808 https://doi.org/10.1007/s12551-018-0399-2

[18] M. Sivapragasam, M. Moniruzzaman, M. Goto, Recent advances in exploiting ionic liquids for biomolecules: Solubility, stability and applications, Biotechnol. J. 11 (2016) 1000–1013 https://doi.org/10.1002/biot.201500603

[19] S. K. Shukla, J.-P. Mikkola, Use of Ionic Liquids in Protein and DNA Chemistry, Front. Chem. 8 (2020) 598662 https://doi.org/10.3389/fchem.2020.598662

[20] M. J. Earle, K. R. Seddon KR, Ionic liquids. Green solvents for the future, Pure Appl Chem 72 (2000) 1391–1398 https://doi.org/10.1351/pac200072071391

[21] E. A. Oprzeska-Zingrebe, J. Smiatek, Aqueous ionic liquids in comparison with standard co-solutes Differences and common principles in their interaction with protein and DNA structures, Biophys. Rev. 10 (2018) 809–824 doi: 10.1007/s12551-018-0414-7.

[22] H. Tateishi-Karimata, N. Sugimoto, Biological and nanotechnological applications using interactions between ionic liquids and nucleic acids, Biophysical Reviews 10 (2018) 931–940 doi: 10.1007/s12551-018-0422-7

[23] K. S. Egorova, A. V. Posvyatenko, S. S. Larin, V. P. Ananikov, Ionic liquids: prospects for nucleic acid handling and delivery, Nucleic Acids Res. 49(3) (2021) 1201-1234 doi: 10.1093/nar/gkaa1280

[24] R Vijayaraghavan, A. Izgorodin, V. Ganesh, M. Surianarayanan, D. R MacFarlaneet, Long-term structural and chemical stability of DNA in hydrated ionic liquids, Angew. Chem., Int. Ed. 49 (2010) 1631−1633 https://doi.org/10.1002/anie.200906610

[25] A. Chandran, D. Ghoshdastidar, S. Senapati, Groove Binding Mechanism of Ionic Liquids: A Key Factor in Long-Term Stability of DNA in Hydrated Ionic Liquids, J. Am. Chem. Soc. 134 (2012) 20330−20339 https://doi.org/10.1021/ja304519d

[26] L. Cardoso, N. M. Micaelo, DNA molecular solvation in neat ionic liquids, Chem. Phys. Chem 12 (2011) 275–277 https://doi.org/10.1002/cphc.201000645

[27] K. Jumbri, M. B. Abdul Rahman, E. Abdulmalek, H. Ahmada, N. M. Micaelo, An insight into structure and stability of DNA in ionic liquids from molecular dynamics simulation and experimental studies, Phys. Chem. Chem. Phys. 16 (2014) 14036-14046 https://doi.org/10.1039/C4CP01159G

[28] K. Jumbri, M. B. Abdul Rahman, E. Abdulmalek, H. Ahmada, N. M. Micaelo, An insight into structure and stability of DNA in ionic liquids from molecular dynamics simulation and experimental studies, Phys. Chem. Chem. Phys. 16 (2014) 14036-14046 https://doi.org/10.1039/C4CP01159G

[29] A. Pabbathi, A. Samanta, Spectroscopic and molecular docking study of the interaction of DNA with a morpholinium ionic liquid, Phys Chem B 119(34) (2015) 11099–11105 https://doi.org/10.1021/acs.jpcb.5b02939

[30] H. Zhao H, DNA stability in ionic liquids and deep eutectic solvents, J. Chem. Technol. Biotechnol. 90(1) (2015) 19–25 https://doi.org/10.1002/jctb.4511

[31] Y. Ding, L. Zhang, J. Xie, R. Guo, Binding Characteristics and Molecular Mechanism of Interaction between Ionic Liquid and DNA, J. Phys. Chem. B 114 (2010) 2033–2043 https://doi.org/10.1021/jp9104757

[32] H. Liu, Y. Dong, J. Wu, C.Chen, D. Liu, Q. Zhang, S. Du, Evaluation of interaction between imidazolium-based chloride ionic liquids and *calf thymus* DNA, Sci. Total Environ. 1–7 (2016) 566–567 https://doi.org/10.1016/j.scitotenv.2016.05.087

[33] P.K. Singh, J. Sujana, A. K. Mora, S. Nath, Probing the DNA–ionic liquid interaction using an ultrafast molecular rotor, J. Photoch. Photobiol. A 246 (2012) 16- 22 http://dx.doi.org/10.1016/j.jphotochem.2012.07.006

[34] Z. Meng, T. Kubar, Y. Mu, F. Shao, A MD-QM theoretical study of DNA-mediated charge transport in hydrated ionic liquids, J Chem Theory Comput. 14(5) (2018) 2733–2742 https://doi.org/10.1021/acs.jctc.7b01201

[35] A. N. Bowers, M. J. Trujillo-Rodríguez, M.Q. Farooq, J. L. Anderson, Extraction of DNA with magnetic ionic liquids using in situ dispersive liquid–liquid microextraction, Anal. Bioanal. Chem. 411 (2019) 7375–7385 doi: 10.1007/s00216-019-02163-9

[36] A. Garai, D. Ghoshdastidar, S. Senapati, P. K. Maiti, Ionic liquids make DNA rigid, J. Chem. Phys. 149 (2018) 045104 (2018) https://doi.org/10.1063/1.5026640

[37] C. Bottari, S. Catalini, P.Foggi, I. Mancini, A. Mele, D. R. Perinelli, A. Paciaroni, A, Gessini, C. Masciovecchio, B. Rossi, Base-specific pre-melting and melting transitions of DNA in presence of ionic liquids probed by synchrotron-based UV Resonance Raman scattering, J. Mol. Liq. 330 (2021) 115433 https://doi.org/10.1016/j.molliq.2021.115433

[38] C. Bottari, I. Mancini, A. Mele, A. Gessini, C. Masciovecchio, B. Rossi, Conformational stability of DNA in hydrated ionic liquid by synchrotron-based UV resonance raman, Proc. SPIE 11086, UV and Higher Energy Photonics: From Materials to Applications 2019, 110860Q https://doi.org/10.1117/12.2529077

[39] B. Rossi, M. Tortora, S. Catalini, J. Vigna, I. Mancini, A. Gessini, C. Masciovecchio and A. Mele, Phys. Chem. Chem. Phys. (2021) https://doi.org/10.1039/D1CP01970H

[40] D. Saha, M. Kulkarni, A. Mukherjee, Water modulates the ultraslow dynamics of hydrated ionic liquids near CG rich DNA: consequences for DNA stability, Phys. Chem. Chem. Phys. 18 (2016) 32107-32115 https://doi.org/10.1039/C6CP05959G

[41] F. Bianchi, L. Comez, R. Biehl, F. D'Amico, A. Gessini, A. M. Longo, C. Masciovecchio, C. Petrillo, A. Radulescu, B. Rossi, F. Sacchetti, F. Sebastiani, N. Violini, A. Paciaroni, Structure of human telomere G-quadruplex in the presence of a model drug along the thermal unfolding pathway, Nucleic Acids Res. 46(22) (2018) 11927–11938 https://doi.org/10.1093/nar/gky1092

[42] L. Comez, F. Bianchi, V. Libera, M. Longo, C. Petrillo, F. Sacchetti, F. Sebastiani, F. D'Amico, B. Rossi, A. Gessini, C. Masciovecchio, H. Amenitsch, C. Sissi, A. Paciaroni, Polymorphism of human telomeric quadruplexes with drugs: a multi-technique biophysical study, Phys. Chem. Chem. Phys. 22(20) (2020) 11583-11592 doi: 10.1039/d0cp01483d

[43] B. Rossi, C. Bottari, S. Catalini, A. Gessini, F. D'Amico, C. Masciovecchio, Synchrotron based UV Resonant Raman scattering for material science, Molecular and Laser Spectroscopy, Volume 2 (eds V. P. Gupta, Y. Ozaki), Elsevier (2020), Chapter 13, pages 447-478, http://dx.doi.org/10.1016/B978-0-12-818870-5.00013-7

[44] D. A. Case, T. A. Darden, T. E. Cheatham, C. L. Simmerling, J. Wang, R.E. Duke, P. A. Kollman, (2008) Amber 10 (No. BOOK). University of California

[45] K. G. Sprenger, V. W. Jaeger, J. Pfaendtner, The general AMBER force field (GAFF) can accurately predict thermodynamic and transport properties of many ionic liquids, J. Phys. Chem. B 119(18) (2015) 5882–5895 https://doi.org/10.1021/acs.jpcb.5b00689

[46] J. Picálek, B. Minofar, J. Kolafa, P. Jungwirth, Aqueous solutions of ionic liquids: study of the solution/vapor interface using molecular dynamics simulations, Phys. Chem. Chem. Phys. 10(37) (2008) 5765-5775 https://doi.org/10.1039/B806205F

[47] W. Jiang, T. Yan, Y. Wang, G. A. Voth, Molecular dynamics simulation of the energetic room-temperature ionic liquid, 1-hydroxyethyl-4-amino-1, 2, 4-triazolium nitrate (HEATN), J. Phys. Chem. B 112(10) (2008) 3121-3131 https://doi.org/10.1021/jp710653g

[48] J. M. Martínez, L. Martínez, Packing optimization for automated generation of complex system's initial configurations for molecular dynamics and docking, J. Comput. Chem. 24(7) (2003) 819-825 doi: 10.1002/jcc.10216

[49] L. Martínez, R. Andrade, E. G. Birgin, J. M. Martínez, PACKMOL: a package for building initial configurations for molecular dynamics simulations, J. Comput. Chem. 30(13), J. (2009) 2157-2164 doi: 10.1002/jcc.21224

[50] B. Hess, H. Bekker, H. J. Berendsen, J. M. Fraaije, LINCS: a linear constraint solver for molecular simulations, J. Comput. Chem. 18(12) (1997) 1463-1472 https://doi.org/10.1002/(SICI)1096-987X(199709)18:12<1463::AID-JCC4>3.0.CO;2-H

[51] T. Darden, D. York, L. Pedersen, Particle mesh Ewald: An N· log (N) method for Ewald sums in large systems, J. Chem. Phys. 98(12) (1993) 10089-10092 https://doi.org/10.1063/1.464397

[52] G. Bussi, D. Donadio, M. Parrinello, Canonical sampling through velocity rescaling. J. Chem. Phys.126(1) (2007) 014101 https://doi.org/10.1063/1.2408420

[53] M. J. Abraham, T. Murtola, R. Schulz, S. Páll, J. C. Smith, B. Hess, E. Lindahl, GROMACS: High performance molecular simulations through multi-level parallelism from laptops to supercomputers, SoftwareX 1 (2015) 19-25 https://doi.org/10.1016/j.softx.2015.06.001

[54] S. Páll, M. J. Abraham, C. Kutzner, B. Hess, E. Lindahl, Tackling exascale software challenges in molecular dynamics simulations with GROMACS. In International conference on exascale applications and software pp. 3-27 (2014) DOI: 10.1007/978-3-319-15976-8_1

[55] S. Pronk, S. Páll, R. Schulz, P. Larsson, P. Bjelkmar, R. Apostolov, M. R. Shirts, J. C. Smith, P. M. Kasson, D. van der Spoel, B. Hess, E. Lindahl, GROMACS 4.5: a high-throughput and highly parallel open source molecular simulation toolkit, Bioinformatics, 29(7) (2013) 845-854 doi: 10.1093/bioinformatics/btt055.

[56] B. Hess, C. Kutzner, D. Van Der Spoel, E. Lindahl, GROMACS 4: algorithms for highly efficient, load-balanced, and scalable molecular simulation, J. Chem. Theory Comput. 4(3) (2008) 435-447 https://doi.org/10.1021/ct700301q

[57] D. Van Der Spoel, E. Lindahl, B. Hess, G. Groenhof, A. E. Mark, H. J. Berendsen, GROMACS: fast, flexible, and free, J. Comput. Chem. 26(16) (2005) 1701-1718. https://doi.org/10.1002/jcc.20291

[58] W. Humphrey, A. Dalke, K. Schulten, VMD: visual molecular dynamics, J. Mol. Graph. 14(1) (1996) 33-38 doi: 10.1016/0263-7855(96)00018-5

[59] S. Genheden, A. Reymer, P. Saenz-Méndez, L. A. Eriksson, Computational Chemistry and Molecular Modelling Basics, in *Computational Tools for Chemical Biology* pp. 1-38 (2017) DOI: 10.1039/9781788010139-00001

[60] S. P. A. Fodor, R. P. Rava, T. R. Hays, T. G. Spiro, Ultraviolet resonance Raman spectroscopy of the nucleotides with 266-, 240-, 218-, and 200-nm pulsed laser excitation, J. Am. Chem. Soc. 107 (1985) 1520-1529 https://doi.org/10.1021/ja00292a012

[61] S. P. A. Fodor, T. G. Spiro, Ultraviolet resonance Raman spectroscopy of DNA with 200-266-nm laser excitation, J. Am. Chem. Soc. 108 (1986) 3198-3205 https://doi.org/10.1021/ja00272a006

[62] J. G. Duguid, V.A. Bloomfield, J. M. Benevides, G. J. Thomas Jr., Raman Spectroscopy of DNA-Metal Complexes. I. The Thermal Denaturation of DNA in the Presence of Sr' , Ba^2, Mg^{2+}, Ca^{2+}, Mn^{2+}, $C0^{2+}$, Ni^{2+}, and Cd^{2+}, Biophys. J. 69 (1995) 2623-2641 https://doi.org/10.1016/S0006-3495(95)80133-5

[63] P.Y. Turpin, L. Chinsky, A. Laigle, B. Jollès, DNA structure studies by resonance Raman spectroscopy, J. Mol. Struct. 214 (1989) 43-70 https://doi.org/10.1016/0022-2860(89)80005-5

[64] S. C. Erfurth, W. I. Peticolas, Melting and premelting phenomenon in DNA by laser Raman scattering, Biopolymers 14 (1975) 247-264 https://doi.org/10.1002/bip.1975.360140202

[65] Z. Q. Wen, G. J. Thomas Jr., UV resonance Raman spectroscopy of DNA and protein constituents of viruses: assignments and cross sections for excitations at 257, 244, 238, and 229 nm, Biopolymers 45(5) (1998) 247-256 https://doi.org/10.1002/(SICI)1097-0282(199803)45:3<247::AID-BIP7>3.0.CO;2-R.

[66] J. G. Duguid, V. A. Bloomfield, J. M. Benevides, G. J. Thomas, DNA melting investigated by differential scanning calorimetry and Raman spectroscopy., Biophys. J. 71 (1996) 3350-3360 https://doi.org/10.1016/S0006-3495(96)79528-0

[67] S. Chan, R. H. Austin, I. Mukerji, T. G. Spiro, Temperature-Dependent Ultraviolet Resonance Raman Spectroscopy of the Premelting State of dA* dT DNA, Biophys. J. 72 (1997) 1512-1520 https://doi.org/10.1016/S0006-3495(97)78799-X

[68] B. Tomlinson, W. L. Peticolas, Conformational Dependence of Raman Scattering Intensities in Polyadenylic Acid, J. Chem. Phys. 52 (1970) 2154 https://doi.org/10.1063/1.1673270

[69] L. Movileanu, J. M. Benevides, G. J. Thomas Jr, Temperature Dependence of the Raman Spectrum of DNA. Part I—Raman Signatures of Premelting and Melting Transitions of Poly(dA–dT)·Poly(dA–dT), J. Raman Spectrosc. 30 (1999) 637–649 https://doi.org/10.1002/(SICI)1097-4555(199908)30:8<637::AID-JRS431>3.0.CO;2-B

[70] I. Mukerji, A. P. Williams, UV resonance Raman and circular dichroism studies of a DNA duplex containing an A(3)T(3) tract: evidence for a premelting transition and three-centered H-bonds, Biochemistry 41 (2002) 69-77 https://doi.org/10.1021/bi010918i

[71] L. Chinsky, P.Y.Turpin, Ultraviolet resonance Raman study of DNA and of its interaction with actinomycin D, Nucleic Acid Res. 5(8) (1978) 2969–2978 https://doi.org/10.1093/nar/5.8.2969

[72] K. Shimizu, M. Tariq, M. F. C. Gomes, L. N. Rebelo, J. N. C. Lopes, Assessing the Dispersive and Electrostatic Components of the Cohesive Energy of Ionic Liquids Using Molecular Dynamics Simulations and Molar Refraction Data, J. Phys. Chem. B 114 (2010) 5831-5834 https://doi.org/10.1021/jp101910c

[73] L. Santos, J. N. C. Lopes, J. A. P. Coutinho, J. Esperanca, L. R. Gomes, I. M. Marrucho, L. N. Rebelo, Ionic liquids: first direct determination of their cohesive energy, J. Am. Chem. Soc. 129 (2007) 284-285 https://doi.org/10.1021/ja067427b

[74] T. Koddermann, D. Paschek, R. Ludwig, Molecular Dynamic Simulations of Ionic Liquids: A Reliable Description of Structure, Thermodynamics and Dynamics, Chem. Phys. Chem. 8(17) (2007) 2464-2470 doi: 10.1002/cphc.200700552.

[75] L. Movileanu, J. M. Benevides, G. J. Thomas Jr, Determination of base and backbone contributions to the thermodynamics of premelting and melting transitions in B DNA, Nucleic Acids Res. 30 (17) (2002) 3767–3777 https://doi.org/10.1093/nar/gkf471

[76] L. Rimai, V. M. Maher, D. Gill, I. Salmeen, J. J. McCormick, The temperature dependence of Raman intensities of DNA. Evidence for premelting changes and correlations with ultraviolet spectra, Biochim. Biophys. Acta, 361 (1974) 155—165 https://doi.org/10.1016/0005-2787(74)90343-8

[77] J. M. Benevides, S.A. Overman, G.J. Thomas Jr, Raman, polarized Raman and ultraviolet resonance Raman spectroscopy of nucleic acids and their Complexes, J. Raman Spectrosc. 36 (2005) 279–299 https://doi.org/10.1002/jrs.1324

[78] N. Fujimoto, A. Toyama, H. Takeuchi, Effects of hydrogen bonding on the UV resonance Raman bands of the adenine ring and its C8-deuterated analog, J. Mol. Struct. 447 (1998) 61-69 https://doi.org/10.1016/S0022-2860(98)00301-9

[79] A. Toyama, H. Takeuchi, I. Harada, Ultraviolet resonance Raman spectra of adenine, uracil and thymine derivatives in several solvents. Correlation between band frequencies and hydrogen-bonding states of the nucleic acid bases, J. Mol. Structure 242 (1991) 87-98 https://doi.org/10.1016/0022-2860(91)87129-6

[80] M. Tsuboi, M. Komatsu, J. Hoshi, E. Kawashima, T. Sekine, Y. Ishido, M. P. Russell, J. M. Benevides, G. J. Thomas, Raman and Infrared Spectra of (2'S)-[2'-2H]Thymidine: Vibrational Coupling between Deoxyribosyl and Thymine Moieties and Structural Implications, J. Am. Chem.Soc. 119 (1997) 2025-2032 https://doi.org/10.1021/ja962676t

[81] A. Jirasek, H. G. Schulze, C. Hughesman, A. L. Creagh, C. A. Haynes, M. W. Blades, R. F. B. Turner, Discrimination between UV radiation-induced and thermally induced spectral changes in AT-paired DNA oligomers using UV resonance Raman spectroscopy, J. Raman Spectrosc. 37 (2006)1368–1380 https://doi.org/10.1002/jrs.1552

[82] N. V. Hud, V. Sklenar, J. Feigon, Localization of ammonium ions in the minor groove of DNA duplexes in solution and the origin of DNA A-tract bending, J. Mol. Biol. 286 (1999) 651-660 https://doi.org/10.1006/jmbi.1998.2513

[83] N. V. Hud, J. Feigon, Localization of Divalent Metal Ions in the Minor Groove of DNA A-Tracts J. Am. Chem. Soc. 119 (1997) 5756-5757 https://doi.org/10.1021/ja9704085

CHAPTER 3

Interactions between a dsDNA Oligonucleotide and Imidazolium Chloride Ionic Liquids: Effect of Alkyl Chain Length, Part I

Fadaei, F., Seifert, M., Raymond, J. R., Řeha, D., Kulik, N., Minofar, B., & Heitz, M. P. (2022). Interactions between a dsDNA Oligonucleotide and Imidazolium Chloride Ionic Liquids: Effect of Alkyl Chain Length, Part I. *Molecules*, *27*(1), 116. https://doi.org/10.3390/molecules27010116

molecules

MDPI

Article

Interactions between a dsDNA Oligonucleotide and Imidazolium Chloride Ionic Liquids: Effect of Alkyl Chain Length, Part I

Fatemeh Fadaei [1,2], Michelle Seifert [3], Joshua R. Raymond [3], David Řeha [1], Natalia Kulik [1], Babak Minofar [1,*] and Mark P. Heitz [3,*]

[1] Laboratory of Structural Biology and Bioinformatics, Institute of Microbiology of the Czech Academy of Sciences, Zámek 136, 37333 Nove Hrady, Czech Republic; fadaei@nh.cas.cz (F.F.); reha@nh.cas.cz (D.Ř.); kulik@nh.cas.cz (N.K.)

[2] Faculty of Science, University of South Bohemia in České Budějovice, Branišovská 1645/31A, 37005 Ceske Budejovice, Czech Republic

[3] Department of Chemistry and Biochemistry, SUNY Brockport, Brockport, NY 14420, USA; michelle.seifert@t-online.de (M.S.); jraym1@brockport.edu (J.R.R.)

* Correspondence: minofar@nh.cas.cz (B.M.); mheitz@brockport.edu (M.P.H.)

Abstract: Ionic liquids (ILs) have become nearly ubiquitous solvents and their interactions with biomolecules has been a focus of study. Here, we used the fluorescence emission of DAPI, a groove binding fluorophore, coupled with molecular dynamics (MD) simulations to report on interactions between imidazolium chloride ($[Im_{n,1}]^+$) ionic liquids and a synthetic DNA oligonucleotide composed entirely of T/A bases (7(TA)) to elucidate the effects ILs on a model DNA duplex. Spectral shifts on the order of 500–1000 cm^{-1}, spectral broadening (~1000 cm^{-1}), and excitation and emission intensity ratio changes combine to give evidence of an increased DAPI environment heterogeneity on added IL. Fluorescence lifetimes for DAPI/IL solutions yielded two time constants 0.15 ns (~80% to 60% contribution) and 2.36–2.71 ns for IL up to 250 mM. With DNA, three time constants were required that varied with added IL (0.33–0.15 ns (1–58% contribution), ~1.7–1.0 ns (~5% contribution), and 3.8–3.6 ns (94–39% contribution)). MD radial distribution functions revealed that π-π stacking interactions between the imidazolium ring were dominant at lower IL concentration and that electrostatic and hydrophobic interactions become more prominent as IL concentration increased. Alkyl chain alignment with DNA and IL-IL interactions also varied with IL. Collectively, our data showed that, at low IL concentration, IL was primarily bound to the DNA minor groove and with increased IL concentration the phosphate regions and major groove binding sites were also important contributors to the complete set of IL-DNA duplex interactions.

Keywords: DAPI; DNA duplex; DNA oligonucleotide; imidazolium ionic liquids; fluorescence; fluorescence lifetime; molecular dynamics; radial distribution function

1. Introduction

Deoxyribonucleic acid (DNA), the most important of biomolecules, plays pivotal biological roles in the storing and carrying of genetic information for the growth, functioning, and reproduction of all known organisms. Due to its tiny size, geometric properties, and atom recognition capabilities, DNA has been recognized as an interesting candidate for the development of new nanomaterial and advanced molecular devices [1,2]. For example, DNA probes, including synthetic oligonucleotides and amplicons, are used in a variety of DNA microarray and DNA chip devices for gene expression, point mutations, and pharmacogenomic and diagnostic applications [3]. Hence, due to the development of DNA molecular probes, the studies on the interaction between synthetic oligonucleotides and other molecules are very important. Recently, multiple works have investigated the interaction of novel molecules with DNA. For instance, Rezki's group designed and synthesized

the imidazolium ionic liquid halides carrying different fluorinated phenylacetamide side chains [4]. In other work, the same group studied pyridinium ionic liquids for their DNA binding properties [5]. In these examples, they investigated the interaction the synthesized ILs with DNA to determine the anticancer mechanism. According to their results, there was a reasonably good binding affinity between the DNA and the designed ionic liquids. In addition, Revathi et al. [6] synthesized a new series of bio active Cu(II) and Zn(II) complexes. They performed both experimental and theoretical study to investigate the possible interaction of them with DNA. They revealed that the mixed ligand complexes interact with CT DNA by intercalation mode. Besides, Alraqa and coworkers [7] designed and synthesized the hybridization of benzotriazole and 1,2,3-triazoles with several functionalities, including amide, ketone, ester, and/or carboxylic acid. According to their results, the compounds have good interaction with the minor grooves of DNA through hydrogen bonding and hydrophobic interactions. They also suggest the reported molecules may be future anticancer agents.

Ionic liquids (ILs) are made of organic cations and usually an inorganic anion, the combination of which results in a water-free salt with a melting point below 100 °C, as first defined by Walden in 1914 [8]. In consideration of using ILs as solvents, they offer attractive physicochemical properties, including low vapor pressure, high thermal stability, nonflammability, and good conductivity. As such, ILs have become viable alternative solvents or co-solvent to conventional organic solvents in different fields of life sciences. In addition, it is interesting to note that a wide variety of cations and anions can be used to form ILs and that each one has unique properties that can meet specific requirements for use in biochemistry, biotechnology, medicine, pharmacology, and bio-nanotechnology, etc., applications [9–16]. The applications and relevant functions of ILs in biomolecular systems are based on the nature of the specific interaction that occur between ILs and biomacromolecules. In recent years, researchers have started investigating interactions between ILs and biomolecules. For example, He et al. [17] used various experimental methods and molecular dynamics (MD) simulation to investigate the interactions between the imidazolium-based IL surfactant 1-dodecyl-3-methylimidazolium bromide [Im$_{12,1}$]Br and DNA in dilute brine. According to their results, there are electrostatic attractions between DNA phosphate groups and [Im$_{12,1}$]Br headgroups and hydrophobic interactions among the alkyl chains. Jumbri et al. [18] used both computational and experimental evidence to analyze the characteristics and the influence of ILs on the structural properties of DNA. The main criterion for DNA stabilization was the hydration shells around the DNA phosphate group where DNA maintains its duplex conformation in ILs. Wang and Cui [19] worked on the interaction of 1-butyl-3-methylimidazolium methanesulfonate ([Im$_{4,1}$][MS]) and 1-hexyl-3-methylimidazolium methanesulfonate ([Im$_{6,1}$][MS]) with calf thymus deoxyribonucleic acid (ctDNA) by fluorescence and ultraviolet–visible (UV) absorption spectra. According to their results, the binding force increased with increasing IL alkyl chain length. They also suggested that both electrostatic and hydrophobic interactions were present between the ctDNA with [Im$_{n,1}$][MS], and hydrophobic interactions played a key role in the interaction process of ctDNA with IL.

Since ILs play a major role in the search for potential candidates as replacements for organic solvents, which can have a deleterious impact on the environment and health, the assessment of ILs as potential green solvent candidates requires that a wide range of applications be examined and as mentioned these contexts must include a thorough examination of IL interactions with varieties of biomolecules. In this regard, it has been shown that ILs have the capability to stabilize DNA for periods of time up to a year, which makes them very attractive as potential solvents for DNA storage [2,20]. Spectroscopy offers a convenient and simple means by which DNA/IL interactions may be studied. Recently, methylene blue analogs have been studied with respect to aggregation and binding to salmon sperm DNA [21]. It was determined that arylamine fragments play a crucial role in DNA interactions, and judicious choice leads to control over binding. Additional work from the same group reported the interactions of PMAM-calix-dendrimers on DNA

binding with no apparent effect on DNA structure that resulted in stabilized DNA [22]. A popular fluorescent probe is 4, 6-Diamidin-2-phenylindol (DAPI, Scheme 1), which is an A/T-nucleic acid specific fluorophore that has been shown to intercalate within the minor groove of B-form DNA [23–28]. Kapuscinskis' research showed that the maximum amount of dye bound to synthetic DNA is one molecule of DAPI per three base pairs [23]. When DAPI binds to DNA, its fluorescence intensity increases and the absorbance shows a significant spectral red shift [29]. Thus, changes in the DAPI microenvironment can be readily detected by measuring spectral changes upon varying parameters that affect the DAPI–DNA interactions. In addition, time-resolved fluorescence has been used to examine DAPI interactions with solvents, polydeoxynucleotides, and linear and closed DNA [30–32]. Gratton and co-workers have reported on the lifetime response of DAPI in ctDNA, and several polydeoxynucleotides that included all A/T sequences polyd(AT), and poly(dA)poly(dT) [30–32]. They found that the decay kinetics in aqueous solution and alcohol solvents were best described by two time constants that were on the order of 0.2 ns and 2.5 ns, but, when in an A/T environment, the time constants lengthened to ~0.4 ns and ~3.8 ns. The fluorescence indicated a lifetime heterogeneity that had its origin from a distribution of ground state molecular conformers. Another conclusion drawn from this work is that the DAPI non-exponentiality is reflective of the DNA binding site heterogeneity [30,31]. They further discussed the idea of preferential solvation of the upon DAPI binding to DNA, where the degree of indole ring solvation is responsible for the relative contributions of the two observed time constants [30].
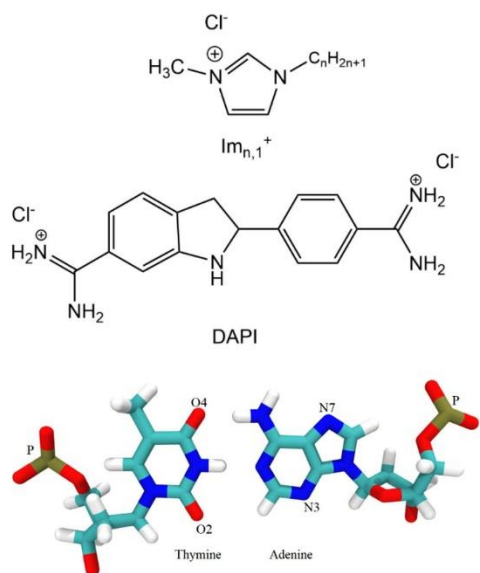
Scheme 1. Structures of the 1- hexadecyl-3-methylimidazolium chloride ([$Im_{16,1}$]Cl), 4, 6-Diamidin-2-phenylindol (DAPI), thymine, and adenine.

In the context of IL research, it is worth noting here that there is still little attention that has been given to the study of interactions between DNA and ILs. To that end, we studied IL effects on a model DNA oligomer system wherein we have examined the effect of IL concentration. The DNA oligonucleotide chosen has the single strand sequence 5′-TATATATATATATA-3′, (7(TA)). We have used steady-state and time-resolved fluorescence coupled with MD simulation to elucidate the interactions that occur between the 7(TA) and 1-hexadecyl-3-methylimidazolium chloride [$Im_{16,1}$]Cl. In part, our goal is to

provide data that can be used to aid in the selection of ILs to be used as solvent systems in a biomolecular context. While we report here in detail on a $[Im_{16,1}]Cl + 7(TA)$ system, we have also included in supporting information some preliminary results from MD simulations that compare $[Im_{16,1}]^+$ to $[Im_{10,1}]^+$ and $[Im_{4,1}]^+$ (Figure S1). We are at present in the process of submitting a second communication to report the experimental results using these shorter chain cations with the goal of providing an assessment of hydrophobicity (via carbon chain lengths variation) on the binding characteristics of ILs to DNA duplex.

2. Results

2.1. Fluorescence Measurements

2.1.1. DAPI Binding Assay

Initial measurements were performed to assess the binding of DAPI to a synthetic double stranded 7(TA) repeat sequence (14 base pairs per strand), B-DNA oligonucleotide to determine the optimal DAPI:DNA ratio be used in our experiments. Experiments with calf thymus DNA (ctDNA) suggested a binding ratio of between 0.04–0.06 dye:DNA base pair [20]. Other work suggested that the DAPI binding site size was 0.33 dye per base pair [23]. The latter work was based on 18 different polynucleotides rather than ctDNA. In this work, aliquots of a DAPI stock solution were titrated into a 1.25 μM DNA duplex/tris buffer solution. Excitation spectra from our titration are presented in Figure 1 for a representative series of DAPI concentrations. The upper panel illustrates the relative spectral intensities for the dye titration, where the spectra were normalized to the peak intensity of the 0.18 μM spectrum. It is well known that the DAPI fluorescence intensity increases when bound to DNA [23,26,27,29,30]. We observed that the fluorescence intensity of DAPI increases upon binding to our 7(TA) DNA duplex and reached a maximum and decreased when the oligonucleotide had accommodated the maximum number DAPI molecules. We observed a maximum increase of ~17-fold. Solid lines in these spectra are for data below the determined optimal binding concentration and dash-dot-dot lines are those above the threshold. In addition to these spectra, we also include normalized spectra in the lower panel of Figure 1 to highlight the spectral shift and shape change as DAPI was added. The normalized spectra show a red shift at the excitation maximum (~365 nm) and a systematic intensity increase, as indicated by the arrows. For completeness, we have also included a set of emission spectra at these same DAPI concentrations in Supporting Information Figure S2, which illustrate similar behavior to the excitation spectra, though the spectral red shift was more substantial.

Excitation and emission peak intensities were normalized to the maximum value in the 0.18 μM spectrum and are shown in Figure 2. Intensity change is linear below ~3 μM DAPI and indicates that DAPI is continuing to bind to the DNA duplex up to this concentration. In either excitation or emission, the maximum intensity was located at ~3.5 μM DAPI, after which intensity systematically decreases. Figure 3 summarizes the energetics of the complete spectral results from the DAPI titration. The peak excitation (upper panel, red symbols) shifts only about 33 cm^{-1} up to a DAPI concentration of 2.1 μM, which is well under our experimental uncertainty of ~100 cm^{-1}, whereas we observe a >300 cm^{-1} red shift for DAPI at 2.9–17.2 μM. In contrast, the emission (blue symbols) is more responsive to the DAPI changes, with peak shifts of 73 cm^{-1} and 2070 cm^{-1}, respectively. In addition, included in Figure 3 are the excitation and emission spectra full width at half maximum values (FWHM, lower panel). The FWHM show nominal change up to ~3 μM DAPI, and the spectra broaden significantly over the remainder of the titration. Here, DAPI is experiencing much broader range of interactions that include at least DAPI–DNA and DAPI-solvent varieties. From these spectroscopic measures, we estimate that the DNA duplex reaches maximum binding at ~ 3.5 μM, most clearly seen in Figure 2. To facilitate comparison of our data with Kapuściński [23], we assumed that our binding concentration estimate could be a representative average over the 14-base pair DNA, but we also exclude the two end TA pairs as less probable binding locations because of extra degrees of motional freedom. To this end, we compute a crudely estimated binding ratio of 0.29 DAPI per base pair and

find that this value is in reasonable agreement with Kapuściński's ratio of 0.33 DAPI per DNA base pair. We also estimated the association constant from the fluorescence data using the method described by Boger and co-workers [33] and determined a value for K of 2.8×10^6 M^{-1} in general agreement with DAPI literature reports that studied synthetic DNA oligomers [23,26,27,33].
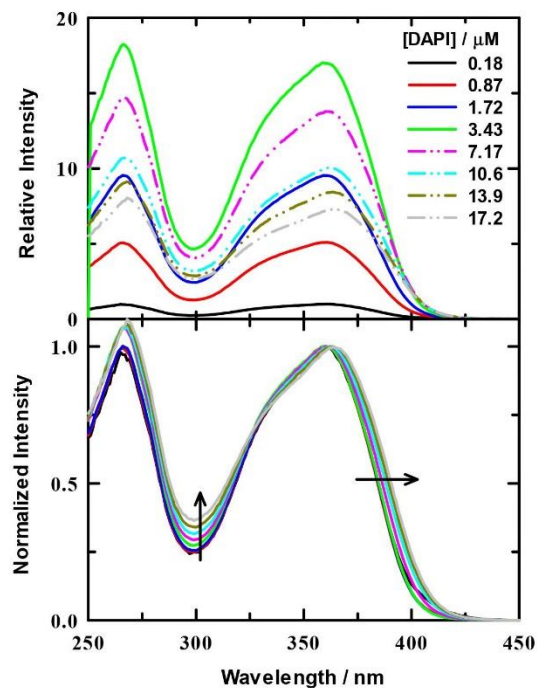

Figure 1. Excitation spectra for DAPI/DNA titration in 10 mM tris buffer at pH = 7.0. DNA concentration was 1.25 μM. Upper panel: Relative intensities of example spectra for varied ratios that are all scaled relative to DAPI/tris buffer. The DAPI/buffer was normalized to 1. Lower panel: normalized spectra for all ratios to help visualize the relative spectral changes. Arrows indicate the direction of spectral change with increasing ratio.
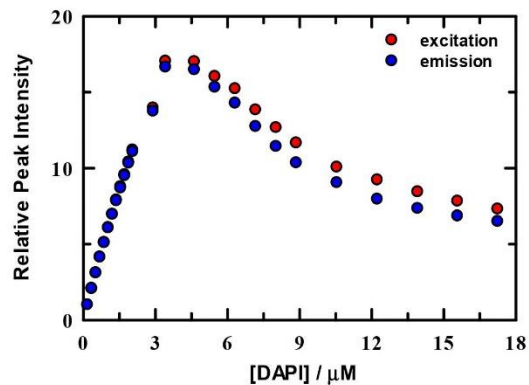
Figure 2. Normalized fluorescence intensities of DAPI in solution with 2.5 μM DNA/10 mM tris buffer at pH = 7.0. Data were normalized to the peak intensity for excitation (red) and emission (blue).
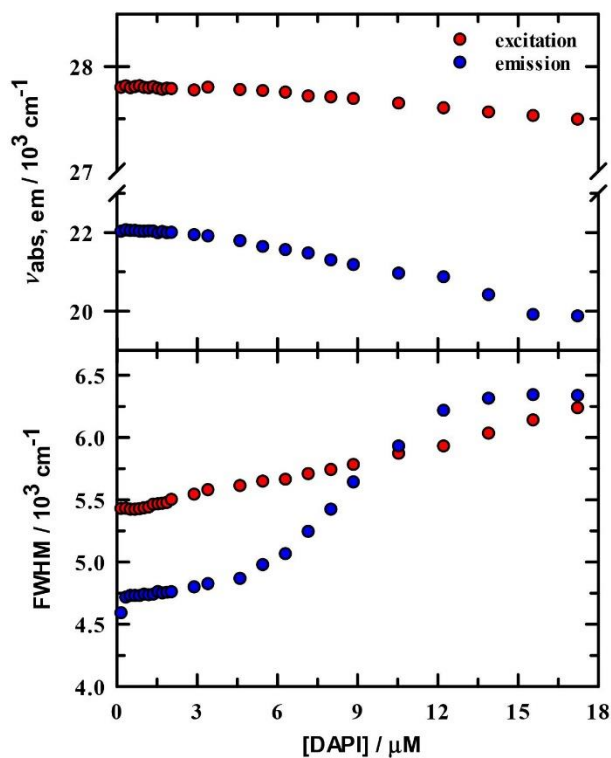

Figure 3. Steady-state spectral parameters for DAPI/DNA duplex in 10 mM tris buffer at pH = 7.0. Upper panel: excitation (red) and emission (blue) peak maxima. Lower panel: excitation and emission full width at half maximum values.

2.1.2. Steady-State Spectroscopy and [Im$_{16,1}$]Cl Titration

Excitation and emission spectral features upon addition of IL are similar to those observed in the DAPI + DNA duplex binding measurements. Spectral examples are shown

in supporting information; see Figures S3 and S4. The effects of IL addition on steady-state spectroscopy are also summarized in Figure 4, where we show the first and second moments (intensity weighted average frequency and width, respectively) of the excitation and emission spectra. The spectral first moment is selected as our metric because it also captures the variability in spectra shape in addition to the simple peak position. Thus, the trends in these data are more representative of the average environment probed by DAPI as IL is added to solution. Data are shown for DAPI in the absence (▲,△) and presence of DNA duplex (●, ○). For excitation, we observe a small red shift in the first moment of approximately 300 cm^{-1}, compared to the more substantial shift of 1000 cm^{-1} for the unweighted peak maximum. The moderation of the first moment shift is explained by the increased intensity of the 265 nm peak. In the presence of DNA duplex, we also observed red shifts of similar magnitude, 400 cm^{-1} in the first moment, and 950 cm^{-1} for the '360 nm' peak maximum. What is of particular interest here is that the shift with DNA results from an initially lower energy in the absence of IL (●) and immediately blue shifts on the first IL addition, followed by a gradual red shift to a constant position. It appears from the excitation data that, while DAPI is bound to DNA duplex, it immediately senses the presence of IL and shifts its energy to nearly the value of DAPI + buffer + IL. A similar pattern is observed for the emission data, where a strong initial red shift in the DAPI + DNA duplex emission occurs with added IL, followed by a smoothly increasing blue shift. The widths in both excitation and emission for both DAPI and DAPI + DNA duplex consistently increased, indicating an increased solution heterogeneity in the presence of IL.
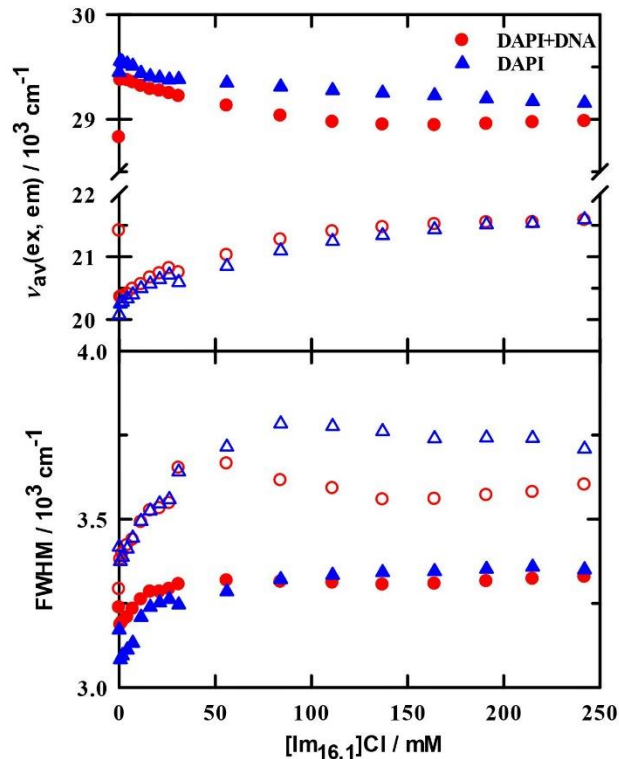
Figure 4. Steady-state excitation (filled symbols) and emission (open symbols) for DAPI + DNA duplex (circles) and DAPI (triangles) in 10 mM tris buffer at pH = 7.0 as a function of added IL. Upper panel: peak positions calculated from spectral first moments (intensity weighted average frequencies). Lower panel: full width at half maximum values of the intensity weighted spectra.

As a further metric for the behavior of spectral peak positions, we computed two sets of peak ratios as a simple means by which we tracked changes on IL addition. The excitation peak ratio (I_{360}/I_{265}) within a single spectrum at each IL concentration (see Figure S5) gives a sense of whether there is any band sensitivity to changes in IL concentration. Initial ratio values are 1.6 and 1.0 for DAPI in tris buffer and DAPI + DNA duplex in tris buffer, respectively. In brief, these ratios both steadily decrease over an IL range of 0–75 mM and then remain essentially constant to beyond 200 mM. Using this measure, other than a nearly uniform intensity difference over the entire IL concentration range, there appears to be nothing special about this ratio. The second ratio uses the spectral maximum at approximately 360 nm for excitation and 460 nm for emission, and computes values for $I_{[IL]}/I_{[IL]=0}$ as IL concentration is varied. These ratios are illustrated in Figure 5 and show rather different behaviors. In DAPI/buffer solutions, the minimum ratio is 1 and rises nearly linearly by more than a factor of 3, independent of excitation or emission. In stark contrast, the DAPI + DNA duplex ratios are all less than ~0.15 with a constant value up to ~50 mM, followed by a steep increase between 50–150 mM and then remain constant. There is a small difference between excitation and emission values, but the series clearly parallel one another.
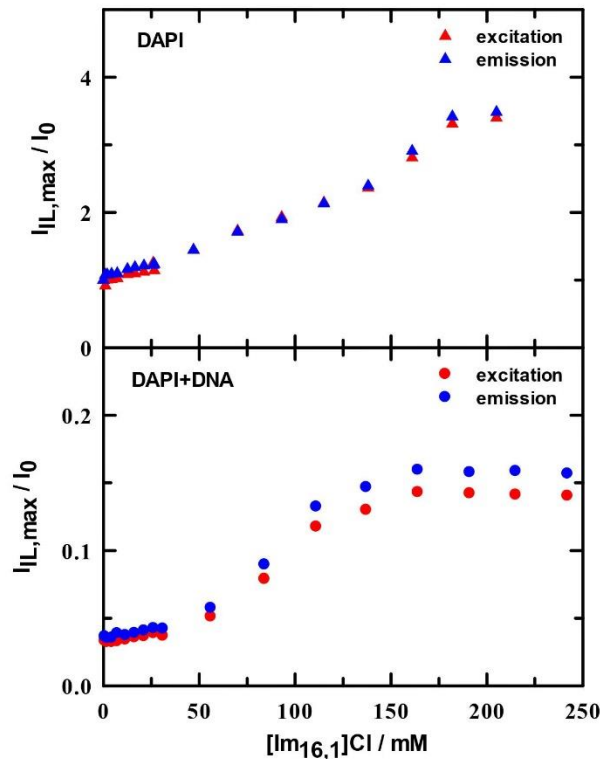
Figure 5. Spectral intensity ratios in 10 mM tris buffer at pH = 7.0 as a function of added IL determined by ratioing intensity in the presence of IL to that in the absence of IL. Upper panel: DAPI excitation (▲) and emission (▲) ratios. Lower panel: DAPI + DNA duplex excitation (●) and emission (●) ratios.

2.1.3. Time–Resolved Spectroscopy and [Im$_{16,1}$]Cl Titration

While the steady-state spectroscopy provides a general characterization of the DAPI fluorescence characteristics, time-resolved fluorescence reveals further details of the emissive properties and compiles the details of magic-angle intensity decay measurements for DAPI and DAPI + DNA duplex solutions in the presence of IL; Figure 6 illustrates the variations as IL is added to solution. These data are presented using a logarithmic scale to show the parameter variation more clearly, particularly at low IL concentration. Filled symbols show the data for time constants and associated fractional contributions to the intensity decay for solutions that include IL, and open pink symbols show the corresponding data in the absence of IL for comparison. Fractions were calculated from the raw data as

$$f_i = \frac{a_i \tau_i}{\sum a_i \tau_i} \tag{1}$$

where a_i is the normalized un-weighted pre-exponential factors determined from the DAS-6 fitting parameters, and τ_i is the ith component lifetime. Star symbols represent the fractionally weighted lifetimes, which are computed as follows:

$$\langle \tau \rangle = \frac{\sum a_i \tau_i^2}{\sum a_i \tau_i} \tag{2}$$

with parameters defined as in Equation (1). We see from the DAPI data (left panels) that the decays in all solutions are well described by two time constants with the larger contribution from the faster time constant (~140 $\pm$ 15 ps). The slower time constant varies between 2.36–2.71 ns. Neat buffer gives a reference point for the emission, and we see that the relative contributions are 77% and 23% for the faster and slower times, respectively. Upon addition of IL, the data shows an increase in the slower lifetime of ~13%, most evident beyond ~3 mM (~log (0.5)), while the faster lifetime remains essentially constant. The slower time contribution drops to 63%. Here, the trend in average lifetime tracks well with the slower time constant.
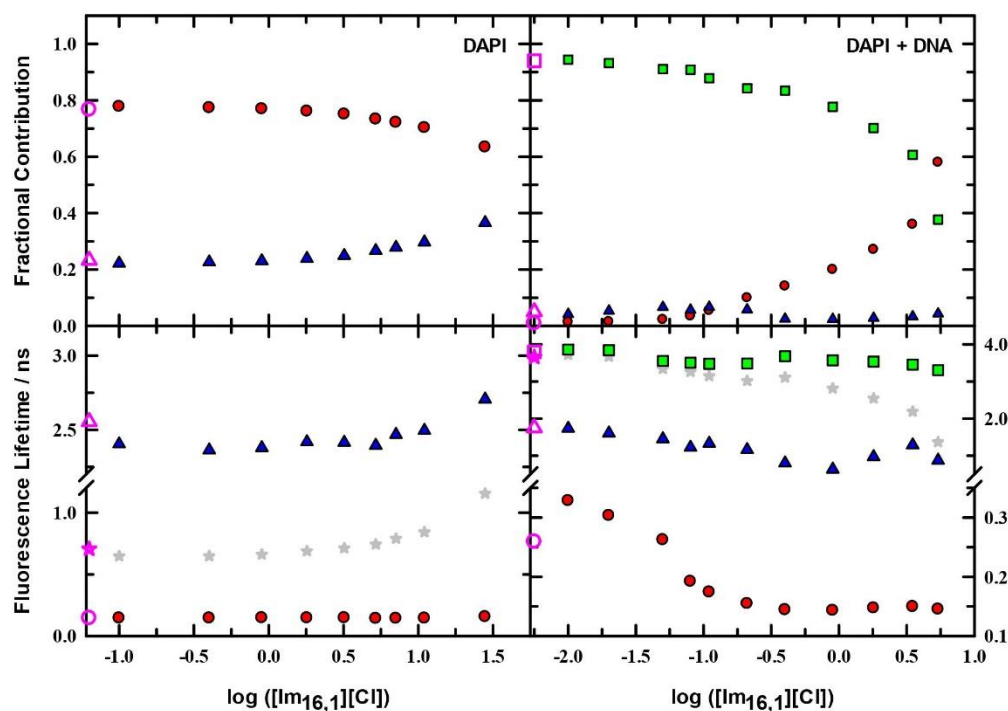

Figure 6. Lifetimes and fractional contributions for DAPI and DAPI + DNA duplex in 10 mM tris buffer at pH = 7.0 as a function of added IL. Left panels: DAPI time constants and associated fractions for a two component fit to the data (●,▲). Right panels: Data for DAPI + DNA duplex for a three component fit to the data (●,▲,■).

When DNA duplex is included in solution, three time constants are needed to characterize the intensity decay (Figure 6, right panels, note the lifetime scale change denoted on the right axis of the lower panel). In buffer solution, the faster (●) and middle (▲) time constants are similar to the DAPI/buffer values but show a modest change, where the fastest time constant increases 260 ps, and the second time decreases to ~1.7 ns. The slowest time constant (■) is 3.8 ns. DNA duplex in solution re-balances the relative contributions, and the two faster times contribute a combined 6% to the total decay. DNA-bound DAPI is dominated by the 3.8 ns lifetime. Since the DAPI/buffer solution requires two time constants, the inclusion of a third time constant with DNA duplex in solution suggests that the three time constants collectively describe two DAPI microenvironments. Moreover, the 94% contribution for the 3.8 ns indicates that DAPI is not 100% bound to DNA duplex, and some free DAPI is in solution. On addition of IL to 10 μM, only the fastest time constant

changes and increases to 330 ps with the same relative contribution. By 400 μM IL, the fastest time constant has decreased to the level of DAPI/buffer at ~150 ps and remains at that value. The middle time constant generally decreased over the IL range measured, as did the slowest time constant. The fractional contribution changes are also important, and both the fastest and slowest values showed steady change with IL such that, in the 5 mM IL solution, 58% of the intensity decay was from the 145 ps component, and 38% was from the 3.31 ns. These changes signal that the IL is effectively manipulating the DAPI microenvironment. The average lifetime values also indicate these changes and show that the most precipitous decrease begins at about 400 μM.

2.2. MD Simulations

2.2.1. The Effect of Concentration on Binding Characteristics of ILs–DNA Duplex

IL cation radial distribution functions (RDFs) have been calculated in three different regions of DNA duplex, which include the phosphate backbone, major groove, and minor groove, to investigate the binding pattern(s) of ILs to DNA duplex. Figure 7 shows the distribution of the imidazolium ring center-of-mass (COM) around the phosphate backbone, major groove, and minor groove of DNA duplex, at different IL concentrations.
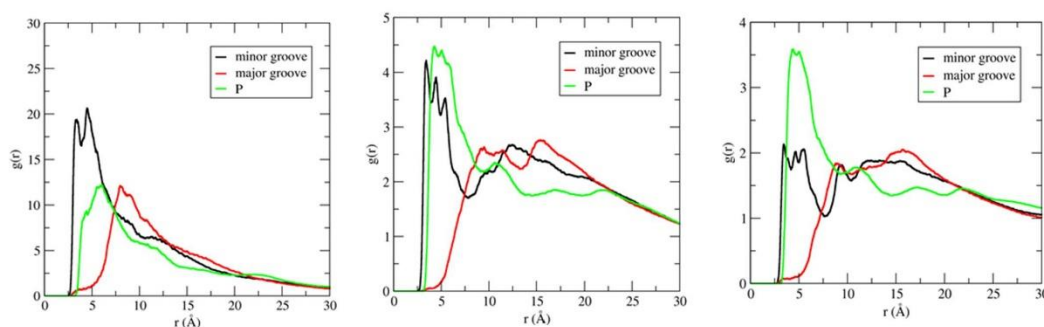

Figure 7. Center–of–mass (COM) radial distribution functions (RDF) for the $[Im_{16,1}]^+$ imidazolium ring around phosphate groups, minor, and major grooves of DNA duplex in different IL concentration solutions. RDFs calculations are performed using the N7 and O4 atoms for the electronegative sites in the major groove. Electronegative sites for the minor groove use N3 and O2 atoms. P atoms were used for the phosphate groups. IL concentrations are 20 mM (**left panel**), 250 mM (**middle panel**), and 500 mM (**right panel**).

For the RDF calculations, we used the phosphate group P atom, electronegative sites N3 and O2 for the minor groove, and electronegative sites N7, O6, and O4 for the major groove (see Scheme 1 for atom labeling). RDFs provide evidence that demonstrates IL cations occupy space within the DNA backbone and groove regions. There is preferential accumulation of the imidazolium ring COM in the minor groove (black lines) at low IL concentration (20 mM, left panel) by a factor of two compared to the major groove (red lines) and P regions (green lines), implying the intrusion of IL cation into the DNA duplex groove. The large peaks for the minor groove−COM of the $[Im_{16,1}]^+$ imidazolium ring locates the COM at 3.4 Å. The position of the peak also gives the nature of the interactions, and the DNA duplex–IL interaction here is primarily a π-π stacking interaction. Simulated data for the other ILs yield similar results in dilute solution (see Figure S6). Furthermore, the shift to longer distance of the phosphate − IL and major groove − IL peaks from 3.4 Å is due to the unavailability of space filled by ILs cations. The same behavior has been repeated in dilute solution by computing the RDFs of IL cation alkyl chain in the three regions of the DNA duplex. By increasing the $[Im_{16,1}]^+$ concentration, the IL cations also established a significant interaction with the DNA phosphate groups (Figure 7, middle

and right panels), the interaction of which is primarily electrostatic between the positively charged imidazolium ring and the negatively charged phosphate.

Figure 8 provides a view of the cation alignment in the DNA duplex minor groove in the 20 mM IL solution (left panel) and a representative snapshot of these cations that align perpendicular to the DNA duplex surface in 500 mM concentrated IL solution (right panel).
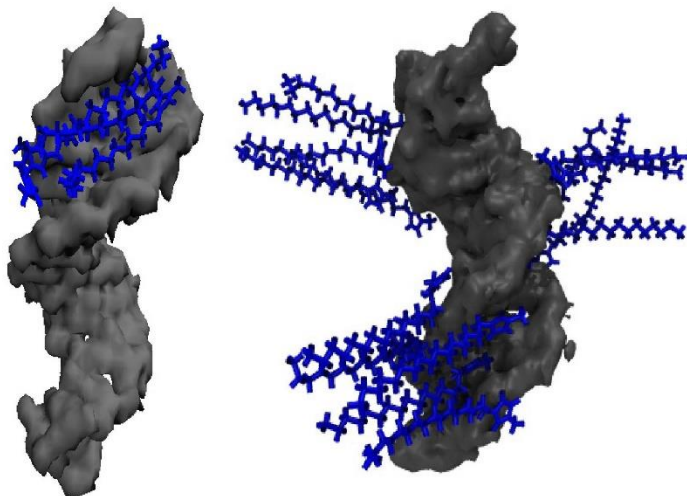

Figure 8. (**Left image**): The distribution of $[Im_{16,1}]^+$ cations (blue color) that shows the association with DNA duplex (gray) minor grooves in the aqueous solution. IL concentration is 20 mM. (**Right image**): The distribution of $[Im_{16,1}]^+$ cations for the association with the DNA duplex surface in the aqueous solution at 500 mM.

These findings are corroborated by a report from Ding et al. [34], who investigated the binding characteristics and molecular interaction mechanism between $[Im_{4,1}]Cl$ and DNA in aqueous solution medium used a wide variety of measurement techniques that included conductivity measurements, fluorescence spectroscopy, dynamic light scattering (DLS), cryogenic transmission electron microscopy (cryo–TEM), circular dichroism spectroscopy, ^{31}P nuclear magnetic resonance (NMR) spectroscopy, Fourier transform infrared spectroscopy, isothermal titration calorimetry (ITC), and quantum chemical calculations. Based on their reported quantum chemical calculations, at a low IL concentration, the cationic headgroups of $[Im_{4,1}]Cl$ localized within several angstroms of the DNA phosphates, whereas the hydrophobic chains arranged parallel to the DNA surface. When the IL concentration is above 0.06 M, the cationic headgroups are near DNA phosphates, and the hydrocarbon chains are perpendicularly attached to the DNA surface.

Owing to the perpendicular orientation of $[Im_{16,1}]^+$ to the DNA duplex groove bases, the IL alkyl chains on the opposite face of the imidazolium are exposed to the bulk solution and parallel alkyl group alignment of the cations to each other implies the existence of alkyl–alkyl chain interactions. The imidazolium ring COM RDFs around the DNA duplex were modified by multiplying the RDF at each concentration by the average number density of particles in the system, with the goal of determining the effect of concentration on the binding characteristics of IL–DNA duplex. Figure 9 shows the concentration dependent results for the imidazolium ring COM distribution around the DNA duplex phosphate backbone (left panel), major groove (middle panel), and minor groove (right panel) for 20 mM, 250 mM, and 500 mM solutions.
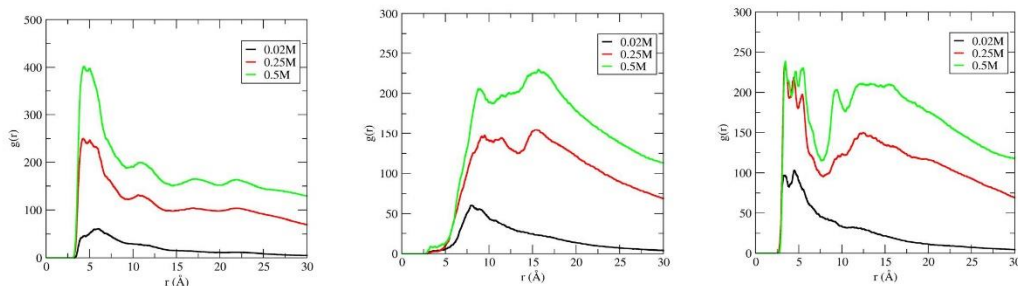
Figure 9. Concentration dependence of the $[Im_{16,1}]^+$ imidazolium ring center-of-mass distribution functions around the phosphate backbone (**left panel**), major groove (**middle panel**), and minor groove (**right panel**) of DNA duplex in aqueous solutions. IL concentrations are 20 mM (black line), 250 mM (red line), and 500 mM (green line) in each panel.

The distribution of IL cations around the various DNA duplex regions increases significantly with increasing IL concentration in all cases. In the P region, there is an 8-fold increase in $g(r)$ from 20 to 500 mM, and a ~4.5-fold increase and ~2.5-fold increase for the major and minor groove populations, respectively. Further, for P, the IL remains localized at ~5 Å as concentration is increased, but, for the DNA duplex groove regions, the dominant contribution shifts consistently from ~5 Å to 15 Å, where the $g(r)$ values are approximately equal. In addition, we note further that IL aggregation also occurs at high IL concentration, and this is pictured in Figure 10.
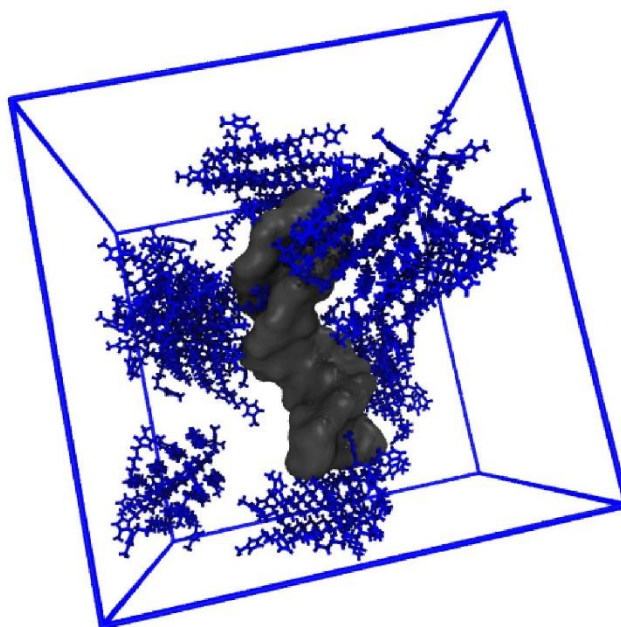

Figure 10. Aggregation of $[Im_{16,1}]Cl$ at 500 mM.

2.2.2. The Effect of Alkyl Chain Length on the Binding Characteristics of ILs–DNA Duplex

The COM RDF of the cation ring and cation alkyl chain around the DNA duplex surface were calculated to characterize more completely the binding characteristics of ILs

to DNA duplex. According to Figure 7, in dilute solution (IL = 20 mM), the COM of the imidazolium ring in hydrated ILs interacts most frequently with the DNA duplex minor groove. Figure 11, left panel, shows the COM RDFs of the imidazolium ring around DNA duplex minor grooves in 20 mM IL solutions.
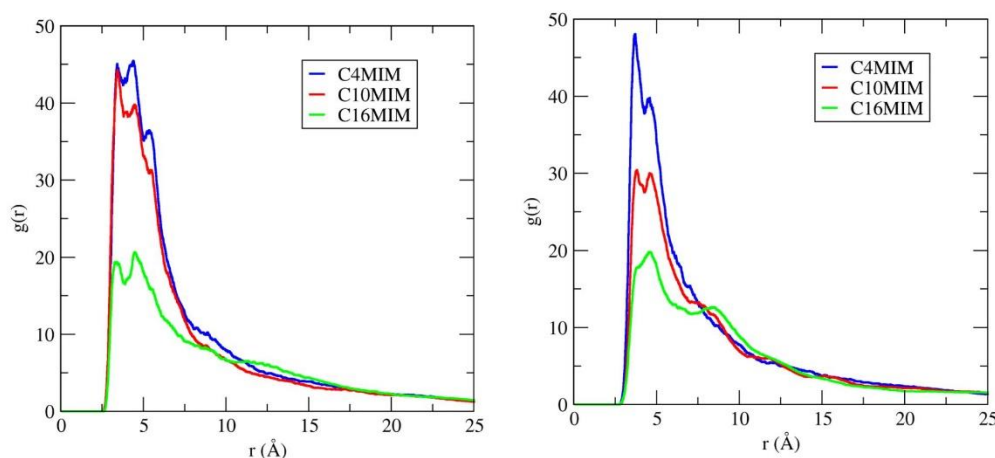

Figure 11. RDFs of the center-of-mass around minor grooves of DNA duplex in 20 mM IL solutions. The electronegative sites N3 and O2 atoms for the minor groove were used for these RDF calculations. (**Left panel**): Data for the imidazolium ring–groove interactions. (**Right panel**): Data for tail–groove interactions.

Here, we see that, by increasing the length of cation alkyl chains from C4 to C16, the COM distribution of the imidazolium ring around minor grooves of DNA decreases (left panel). We also illustrate the cation alkyl chain RDFs around the DNA minor grooves in 20 mM IL (Figure 11, right panel), and they, too, also decrease with chain length. According to these data, there is less interaction probability between the longer alkyl chain IL and the DNA minor groove.

3. Discussion

Two different binding modes have been reported from force spectroscopy measurements of DAPI binding to DNA duplex under varying ionic strength [35]. The authors report that DAPI minor groove binding occurs first and is the dominant mode until DNA duplex saturation is achieved, with a reported binding constant about 10^7 M^{-1}. The second binding mode is reported as intercalation, which is only observed after DNA saturation and with a decreased binding constant of 10^5 M^{-1}. Our spectroscopic results are consistent with these modes of association, as evidenced by the contrast in IL solution intensity ratios between DAPI and DAPI + DNA duplex (see Figure 5). For DAPI/IL solutions, there is no specific binding mechanism, and the ratio increases linearly with IL concentration, whereas, when DNA is present, the intensity ratio is suggestive of an IL concentration induction at low IL and presents a sigmoid shape as IL concentration increases. At least two possibilities explain this observation, where, in the first case, the IL can displace the bound DAPI but only after a threshold concentration reaches, seemingly, ~30–40 mM IL. At high IL concentration, the IL–IL associations offers an additional milieu (see MD results) with which DAPI is likely interacting, in addition to a combined DNA duplex-IL environment. For example, [Im$_{16,1}$]Cl has been shown to undergo aggregation in aqueous solution. El Seoud and co-workers determined the critical micelle concentration (cmc) for [Im$_{16,1}$]Cl from conductivity, surface tension, and fluorescence measurements and reported a cmc value of ~0.9 mM [36,37]. Therefore, [Im$_{16,1}$]Cl in our solutions has clearly aggregated. However,

the consistent response of DAPI over the entire titration range reported here indicated that, while IL aggregation occurs, it does not appear to affect the DAPI spectroscopy in any obvious manner. In addition, since DAPI is a dicationic dye, it must localize near to the IL ion region and, as such, resides in the aqueous-IL interfacial region. More importantly, when in the presence of DNA, DAPI is strongly associated with the duplex minor groove, and IL aggregation that occurs in the bulk does not appear to interfere with this spectroscopic signature. In fact, except for the difference in absolute value of the intensity ratios (see Figure 5), we calculate the same values for slope (i.e., same degree of linearity) when normalizing the intensity ratios in the lower IL concentration range of 0–30 mM for DAPI, in either the absence or presence of DNA. Thus, it is the DAPI–DNA interaction that is the primary driver of the observed intensity ratio difference and the presence of DNA effectively mitigates the impact of IL on the DAPI spectroscopy. The intensity ratio for DAPI/IL is between 1 and 4, whereas, in the presence of DNA, duplex is not more than 0.15, even at 200 mM IL. The intensity ratio increases and signals that DNA duplex bound DAPI does sense IL but, apparently, does not see a neat IL environment.

In consideration of the lifetime data, the fastest (●, Figure 6) time constant change on first addition of IL (=10 μM) gives evidence that the IL interacts with DAPI. However, more importantly, since the time constant value increased, we interpret this as the IL interacting with DNA duplex-bound DAPI because the fastest time constant for the free DAPI-IL interaction was 145 ps and remained constant independent of IL. With successive additions of IL to the DNA duplex solution, we noted a steady decrease in the fastest time constant (●) with a concomitant increase in its fractional contribution, with a simultaneous reduction in the contribution of the slowest time constant (■), which suggests a free DAPI environment is increasingly observed with added IL. It may be that IL has saturated the DNA duplex bound DAPI population and quenched the fluorescence, thereby shortening the DAPI lifetime, or that IL is displacing DAPI from the DNA duplex minor groove binding site, and the proportion of free DAPI fluorescence has increased. In either case, the fractional contribution (●) changes buttress the free DAPI perspective since the value increases dramatically from 1% in DAPI–DNA/buffer to 58% in 5 mM IL solution.

The data obtained from steady-state spectroscopy for $[Im_{16,1}]Cl$ titration indicated a small red shift in the first moment of approximately 300 cm^{-1} and also revealed that DAPI bound to the DNA duplex immediately sensed the presence of IL. The energy shifted to nearly the value of DAPI + IL+ buffer. This observation is consistent with the interactions revealed from MD simulations and corroborates the MD results. Of course, the MD data cannot be quantitatively compared with the spectroscopic data, but the RDF analysis revealed that such interactions are indeed present in the DNA + IL solutions. From MD simulations, we noted that, in the most dilute solution (20 mM), the hydrophobic alkyl chain is arranged parallel to the DNA duplex surface, where the imidazolium ring interacts via π-π stacking interaction with grooves. Thus, the interactions between DAPI and IL are projected to be the greatest. In the concentrated solution (500 mM), the cationic headgroups are near the DNA duplex phosphates, and the hydrocarbon chains are perpendicularly attached to the DNA duplex surface, especially in hydrated $[Im_{16,1}]^+$. We have concluded that the hydrophobic interaction between the IL hydrocarbon chain and the bases of DNA duplex plays a dominant role at lower IL concentrations, and the electrostatic interaction is essential in the IL binding to DNA duplex at higher IL concentrations. In the most dilute solution (20 mM), the hydrophobic alkyl chain is arranged parallel to the DNA duplex surface where the imidazolium ring interacts via π-π stacking interaction with grooves. The RDF data suggest that shorter chain cations readily populate the DNA duplex minor groove compared to longer chain analogs.

4. Materials and Methods

Chemicals were purchased and prepared as follows. The DAPI dye was purchased from Invitrogen ThermoFisher Scientific, Life Technologies Corporation, Carlsbad, CA, USA, and prepared at a stock concentration of 1 mM. The DNA oligonucleotides were from

Integrated DNA Technologies, Inc. (IDT), Coralville, IA, USA. A 0.5 mM stock solution of dsDNA (1 mM single strand) was prepared and used in dilution to make all required oligonucleotides solutions. Tris-HCl buffer (10 mM, pH 7) was used as a solvent. ILs were purchased from Ionic Liquids Technologies (IoLiTec), Heilbronn, Germany at >98%, stored in a nitrogen glove box and used as received.

The UV-visible (UV-vis) absorption spectrum was measured using a Perkin-Elmer double beam Lambda 800 UV-vis spectrophotometer, Waltham, MA, USA. Absorption measurements were made by scanning between 220 to 450 nm, with a slit width of 2.0 nm. Steady-state excitation and emission spectra were measured using a HORIBA Fluorolog 3 fluorimeter, Horiba Scientific, Piscataway, NJ, USA. The fluorimeter is equipped with a single grating excitation monochromator and a double grating emission monochromator for enhanced stray light rejection. All spectra were subtracted and corrected for instrument responses. Excitation spectra were measured over a wavelength range of 250–450 nm with emission detected at 470 nm, whereas emission spectra were measured by scanning over a wavelength range of 350–650 nm with excitation at 330 nm. For both spectral acquisitions, excitation and emission slits were fixed at a 2 nm band pass. When the signal was too high for the detector to respond linearly (>2 × 10^6 cps), the signal was reduced using a spectrally flat neutral density filter that applied a 2.93 factor reduction in intensity. Spectra were corrected when needed and the re-scaled data were used in the data set. We have described our time-correlated single photon counting (TCSPC) instrument previously [38,39]. Briefly, photons from a 405 nm NanoLED (405-L) high output diode laser (Horiba Scientific, Piscataway, NJ, USA) were passed through a polarizer prior to entering the sample. Emission photons were passed through an automated Glan-Thompson polarizer set at "magic" angle (54.7°) for lifetime measurements and spectrally resolved with the double grating monochromator, as well as detected with an air-cooled IBH TBX 850 detector. The instrument response function was measured using a scattering solution and was on the order of 170 ps. Time calibration of the counting electronics was 7.16 ps per channel. All decay data was measured at the peak of the steady-state emission with emission slits between 4–6 nm. Intensity decays were fit using a sum of exponentials models with an iterative reconvolution algorithm that was part of the IBH DAS6 decay analysis software (Horiba Scientific, Piscataway, NJ, USA). Following the deconvolution fitting process, the estimated effective time resolution was ~50 ps, which we have also confirmed from replicate measurements. Reduced chi-squared values (χ_r^2) for a fit was judged to be acceptable if $\chi_r^2 < 1.2$.

For DAPI-DNA duplex binding experiments, we used we used a 1.25 μM dsDNA sample with a constant volume addition of DAPI titrated into solution that resulted in a concentration that ranged from 0.175 to 17.2 μM DAPI in tris-HCl buffer. A solution of 1.25 μM dsDNA in tris-HCl buffer was used as the blank. For IL experiments, three solutions were prepared and run in parallel. The first set of solutions was used to measure the response of DAPI to the presence of ILs. A second set of solutions were made that included 1.25 μM of the DNA oligonucleotide. Finally, tris-HCl buffer containing the corresponding amount of IL was used as a blank. The IL concentrations added to each sample ranged from 0–250 mM. All optical measurements were made in 1 cm quartz cuvettes (23-Q-10, Starna Inc, Atascadero, CA, USA).

MD simulations were performed using the General Amber Force Field (GAFF) [40] and AMBER99SB-ILDN protein, nucleic AMBER94 [41] were used for the imidazolium-based ILs and DNA duplex, respectively. To build the initial structure of the systems, the DNA duplex molecule was placed in the center of the cubic box with the size of 7.1 × 7.1 × 7.1 nm. A total number of 5, 56, and 112 pair of cations and anions were added randomly by Packmol package in the simulation boxes [42,43] to reach the desired IL concentrations from the experiment that were 0.02 M, 0.25 M, and 0.5 M. Then, the simulation boxes were solvated by water molecules, using the TIP3P model of water [44]. As certain undesirable interactions might arise in the systems due to randomly added molecules to the simulation boxes, the steepest descent minimization approach was utilized

to eliminate all unfavorable interactions. After that, all systems were equilibrated by performing 100 ps NVT (Canonical ensemble) restrained simulations followed by 100 ps NPT (isothermal–isobaric ensemble). Equilibration proceeded with the production runs where the linear constraint solver (LINCS) algorithm [45] was employed for all bonds involving hydrogen atoms and short-range non-bonded interactions were cut off by 1.2 nm. Long-range electrostatic interactions were treated by the particle mesh Ewald method [46] procedure. To produce initial velocities, Maxwell–Boltzmann distribution was used for all simulations. V-rescale coupling algorithm was used [47] with the coupling constant of 0.1 ps to ensure constant temperature and pressure during the simulations. MD production runs were performed for 200 ns at 300 K, where 2 fs time step was used. Data for further analysis were stored in every 5 ps for all simulations. The GROMACS 2018 program package was used for performing MD simulations [48–52]. In addition, Visual Molecular Dynamics (VMD) was applied for visualizations and preparation of snapshots [53]. After the simulation, the radial distribution function (RDF) was used to describe the distribution of solvent molecules around the specific molecule or atoms of DNA or ILs.

We note here that using only picoseconds of equilibration time may be insufficient for the complex solutions studied here; therefore, we analyzed the data using the last 150 ns of the 200 ns simulation, which means we used the first 50 ns as an equilibration phase. The equilibration process described above was also checked by running an initial 10 ns NPT equilibration, followed by a 10 ns NVT equilibration, before starting the production run. A comparison between using the standard GROMACS procedure and using this longer equilibration process and running an initial 10 ns NPT equilibration, followed by a 10 ns NVT, both led to equilibrated systems which could be used for further analysis. Moreover, using either equilibration procedure did not change the final conclusions reached from the MD calculations. With regard to simulation equilibration, achievement of equilibrium/structural stability was checked by evaluating the root-mean-square deviation (RMSD), and Figure S7 shows examples of RMSD values for aqueous and IL solutions.

Additionally, Figure S8 shows unsmoothed RDFs for IL tail–DNA groove interaction in 20 mM IL to provide a sense of the actual fluctuations in the RDF data. Otherwise, all other RDF plots here are presented as smoothed functions.

5. Conclusions

Millions of biological samples, including cells, and DNA/RNA, are stored every year for diagnostics, research, and forensic science. Solvents play a critically important role in various ways from stabilizing and preserving the conformation of DNA to storage and handling of DNA, with application to different fields, including biology, medical diagnostics, and biotechnology. DNA samples in aqueous solution cannot preserve their structures for long periods of time and degradation of the DNA structure after prolonged storage is observed. In addition, there is the risk of hydrolytic and oxidative damage for DNA in water solutions. Moreover, using pure water as a solvent for DNA creates some difficulties in nanotechnology due to water vaporization for samples in small volumes and when under open-air conditions. Hence, to increase the use of DNA in industry, searching and finding an appropriate medium to increase the stability of DNA and overcome the limitations of aqueous buffers is necessary. Aqueous imidazolium based ionic liquids are suggested as medium to enhance the structural stability of DNA. However, the interaction mechanism between this IL class and DNA has been not completely assessed.

We have reported on the interactions between a self-complimentary 7(TA) DNA oligonucleotide and imidazolium chloride ionic liquids using steady-state and time-resolved fluorescence spectroscopy and complimented the experimental data with molecular dynamics simulations. We first determined the binding ratio between the fluorescent dye, DAPI, and the DNA duplex and found that there were approximately 3 DAPIs per DNA (here, DAPI ~3 μM), in good agreement with literature reports. Steady-state spectroscopy showed that, beyond 3 μM DAPI, the excitation and emission spectra blue shifted and broadened significantly, indicating that DAPI was both bound to DNA but also interacted

with bulk solvent. In the presence of DNA + IL, the excitation and emission spectra showed an immediate shift, which then moderated back toward the initial value observed in the absence of IL. Spectra remained broadened over the range of IL concentration, confirming that DAPI was residing in multiple environments. Computed intensity ratios ($I_{[IL]}/I_{[IL]=0}$) as a function of IL showed clearly different values for DAPI + IL solutions (~1–4) and DAPI + DNA + IL (<0.15), which differentiated DAPI interactions with bulk IL from the DNA-IL interactions. While the ratio values suggest that IL likely displaces some DAPI from its minor groove binding location (e.g., increased ratio), the DAPI appears to largely remain in the DNA groove.

Fluorescence lifetimes showed that, for DAPI in IL solutions, two time constants were required, with about 78% of the intensity decay associated with a 150 ps lifetime, and the contribution moderated to about 60% in 30 mM IL. The longer lifetime varied from 2.4 ns to 2.7 ns over the same range. The average lifetime varied from 0.7 ns to 1.1 ns. For DNA–based solutions, three time constants were needed, two of which were similar to DAPI/IL, with the addition of third time of ~3.8 ns. The contribution of the fastest time decreased from 330 ps to 150 ps, with a contribution that rose from an initial value of 1% to 58% in 5 mM IL. Moreover, the longest lifetime, associated with the DAPI–DNA duplex interaction, remained similar in time but decreased in contribution from 94% to 39%. We take this to indicate that DAPI senses an increasingly bulk–like IL environment while still associating with DNA. At least two populations of DAPI are represented, one bound to the DNA duplex, and one representing free DAPI.

MD simulations were used to investigate the interactions between alkyl imidazolium based ILs with. The results from MD simulations indicated that a fraction of IL cations always enter the DNA minor groove in a dilute solution of ILs. With increased IL concentration, the cationic headgroups lie near the DNA phosphates groups. Tail interactions are also observed where, at low IL concentration, the alkyl chains are arranged parallel to the DNA surface, and, with increased IL concentration, the alkyl chains are arranged perpendicular to the surface of DNA. Furthermore, with shorter alkyl chains, DNA–IL complexes form that show electrostatic attraction between the cation and DNA phosphates, π–π stacking interaction, and hydrophobic interaction between the alkyl chains and the DNA bases. The electrostatic, π–π stacking, and hydrophobic interactions are essential in the binding ILs to DNA.

Supplementary Materials: The following supporting information can be downloaded, Figure S1: Structures of the imidazolium chloride ionic liquids, Figure S2: Steady-state emission spectra at various DAPI:DNA ratios, Figure S3: DAPI + [Im$_{16,1}$]Cl in 10 mM tris buffer at pH = 7.0. Figure S4: DAPI + DNA + [Im$_{16,1}$]Cl in 10 mM tris buffer at pH = 7.0., Figure S5: Excitation intensity ratios for DAPI and DAPI + DNA in 10 mM tris buffer at pH = 7.0 as a function of IL concentration, Figure S6: Center-of-mass (COM) radial distribution functions (RDF) for the [Im$_{4,1}$]+ and [Im$_{10,1}$]+ imidazolium rings around phosphate groups, minor, and major grooves of DNA duplex, Figure S7: Root-mean-square deviations from equilibration runs, Figure S8: Unsmoothed RDFs for tail-groove interactions in 20 mM [Im$_{16,1}$]Cl, Table S1: Intensity decay fits for solutions of DAPI + [Im$_{16,1}$]Cl, Table S2: Intensity decay fits for solutions of DAPI + DNA + [Im$_{16,1}$]Cl.

Author Contributions: Conceptualization, M.P.H., B.M; methodology, M.P.H., B.M; validation, M.P.H., B.M; formal analysis, M.P.H., M.S., J.R.R., F.F., D.Ř.; investigation, M.P.H., M.S., J.R.R., F.F., N.K.; resources, M.P.H., B.M.; data curation, M.S., J.R.R., F.F., D.Ř., N.K; writing—original draft preparation, M.P.H., M.S.; writing—review and editing, M.P.H.; supervision, M.P.H., B.M.; project administration, M.P.H., B.M.; funding acquisition, M.P.H., B.M. All authors have read and agreed to the published version of the manuscript.

References

1. LaBean, T.H.; Li, H. Constructing novel materials with DNA. *Nano Today* **2007**, *2*, 26–35. [CrossRef]
2. Vijayaraghavan, R.; Izgorodin, A.; Ganesh, V.; Surianarayanan, M.; MacFarlane, D.R. Long-Term Structural and Chemical Stability of DNA in Hydrated Ionic Liquids. *Angew. Chemie Int. Ed.* **2010**, *49*, 1631–1633. [CrossRef]
3. Heller, M.J. DNA Microarray Technology: Devices, Systems, and Applications. *Ann. Rev. Biomed. Engineer.* **2002**, *4*, 129–153. [CrossRef] [PubMed]
4. Rezki, N.; Al-blewi, F.F.; Al-Sodies, S.A.; Alnuzha, A.K.; Messali, M.; Ali, I.; Aouad, M.R. Synthesis, Characterization, DNA Binding, Anticancer, and Molecular Docking Studies of Novel Imidazolium-Based Ionic Liquids with Fluorinated Phenylacetamide Tethers. *ACS Omega* **2020**, *5*, 4807–4815. [CrossRef]
5. Al-Sodies, S.A.; Aouad, M.R.; Ihmaid, S.; Aljuhani, A.; Messali, M.; Ali, I.; Rezki, N. Microwave and conventional synthesis of ester based dicationic pyridinium ionic liquids carrying hydrazone linkage: DNA binding, anticancer and docking studies. *J. Mol. Struct.* **2020**, *1207*, 127756. [CrossRef]
6. Revathi, N.; Sankarganesh, M.; Dhaveethu Raja, J.; Vinoth Kumar, G.G.; Sakthivel, A.; Rajasekaran, R. Bio-active mixed ligand Cu(II) and Zn(II) complexes of pyrimidine derivative Schiff base: DFT calculation, antimicrobial, antioxidant, DNA binding, anticancer and molecular docking studies. *J. Biomolec. Struct. Dyn.* **2021**, *39*, 3012–3024. [CrossRef] [PubMed]
7. Alraqa, S.Y.; Alharbi, K.; Aljuhani, A.; Rezki, N.; Aouad, M.R.; Ali, I. Design, click conventional and microwave syntheses, DNA binding, docking and anticancer studies of benzotriazole-1,2,3-triazole molecular hybrids with different pharmacophores. *J. Mol. Struct.* **2021**, *1225*, 129192. [CrossRef]
8. Walden, P. Ueber die Molekulargrösse und elektrieshe Leitfähigkeit einiger gazehmolzenen Salze. *Bull. Acad. Imper. Sci. St. Petersbg.* **1914**, *8*, 405–422.
9. Benedetto, A.; Ballone, P. Room-Temperature Ionic Liquids and Biomembranes: Setting the Stage for Applications in Pharmacology, Biomedicine, and Bionanotechnology. *Langmuir* **2018**, *34*, 9579–9597. [CrossRef]
10. Somers, A.E.; Howlett, P.C.; MacFarlane, D.R.; Forsyth, M. A Review of Ionic Liquid Lubricants. *Lubricants* **2013**, *1*, 3–21. [CrossRef]
11. Lei, Z.; Chen, B.; Koo, Y.-M.; MacFarlane, D.R. Introduction: Ionic Liquids. *Chem. Rev.* **2017**, *117*, 6633–6635. [CrossRef]
12. Weingärtner, H. Understanding Ionic Liquids at the Molecular Level: Facts, Problems, and Controversies. *Angew. Chem. Int. Ed.* **2008**, *47*, 654–670. [CrossRef] [PubMed]
13. Rogers, R.D.; Seddon, K.R. Ionic Liquids–Solvents of the Future? *Science* **2003**, *302*, 792–793. [CrossRef] [PubMed]
14. Xu, W.; Angell, C.A. Solvent-Free Electrolytes with Aqueous Solution-Like Conductivities. *Science* **2003**, *302*, 422–425. [CrossRef]
15. Seddon, K.R. A taste of the future. *Nat. Mater.* **2003**, *2*, 363–365. [CrossRef] [PubMed]
16. Uddin, M.N.; Basak, D.; Hopefl, R.; Minofar, B. Potential Application of Ionic Liquids in Pharmaceutical Dosage Forms for Small Molecule Drug and Vaccine Delivery System. *J. Pharm. Pharm. Sci.* **2020**, *23*, 158–176. [CrossRef] [PubMed]
17. He, Y.; Shang, Y.; Liu, Z.; Shao, S.; Liu, H.; Hu, Y. Interactions between ionic liquid surfactant [C12mim]Br and DNA in dilute brine. *Colloid Surf. B Biointerfaces* **2013**, *101*, 398–404. [CrossRef]
18. Jumbri, K.; Abdul Rahman, M.B.; Abdulmalek, E.; Ahmad, H.; Micaelo, N.M. An insight into structure and stability of DNA in ionic liquids from molecular dynamics simulation and experimental studies. *Phys. Chem. Chem. Phys.* **2014**, *16*, 14036–14046. [CrossRef]
19. Wang, X.; Cui, F. Binding characteristics of imidazolium-based ionic liquids with calf thymus DNA: Spectroscopy studies. *J. Fluorine Chem.* **2018**, *213*, 68–73. [CrossRef]
20. Chandran, A.; Ghoshdastidar, D.; Senapati, S. Groove Binding Mechanism of Ionic Liquids: A Key Factor in Long-Term Stability of DNA in Hydrated Ionic Liquids? *J. Am. Chem. Soc.* **2012**, *134*, 20330–20339. [CrossRef]
21. Khadieva, A.; Mostovaya, O.; Padnya, P.; Kalinin, V.; Grishaev, D.; Tumakov, D.; Stoikov, I. Arylamine Analogs of Methylene Blue: Substituent Effect on Aggregation Behavior and DNA Binding. *Int. J. Molec. Sci.* **2021**, *22*, 5847. [CrossRef]
22. Mostovaya, O.; Padnya, P.; Shiabiev, I.; Mukhametzyanov, T.; Stoikov, I. PAMAM-calix-dendrimers: Synthesis and Thiacalixarene Conformation Effect on DNA Binding. *Int. J. Molec. Sci.* **2021**, *22*, 11901. [CrossRef] [PubMed]
23. Kapuściński, J.; Szer, W. Interactions of 4′, 6-diamidine-2-phenylindole with synthetic polynucleotides. *Nucleic Acids Res.* **1979**, *6*, 3519–3534. [CrossRef] [PubMed]

24. Eriksson, S.; Kim, S.K.; Kubista, M.; Norden, B. Binding of 4′,6-diamidino-2-phenylindole (DAPI) to AT regions of DNA: Evidence for an allosteric conformational change. *Biochemistry* **1993**, *32*, 2987–2998. [CrossRef]

25. Barcellona, M.L.; Favilla, R.; Von Berger, J.; Avitabile, M.; Ragusa, N.; Masotti, L. DNA-4′-6-diamidine-2-phenylindole interactions: A comparative study employing fluorescence and ultraviolet spectroscopy. *Arch. Biochem. Biophys.* **1986**, *250*, 48–53. [CrossRef]

26. Kapuscinski, J. DAPI: A DNA-Specific Fluorescent Probe. *Biotechnic Histochem.* **1995**, *70*, 220–233. [CrossRef] [PubMed]

27. Larsen, T.A.; Goodsell, D.S.; Cascio, D.; Grzeskowiak, K.; Dickerson, R.E. The Structure of DAPI Bound to DNA. *J. Biomol. Struct. Dyn.* **1989**, *7*, 477–491. [CrossRef]

28. Kapuściński, J.; Skoczylas, B. Fluorescent complexes of DNA with DAPI 4′,6-diamidine-2-phenyl indole 2HCl or DCI 4′,6-dicarboxyamide-2-pnenyl indole. *Nucleic Acids Res.* **1978**, *5*, 3775–3800. [CrossRef] [PubMed]

29. Lin, M.S.; Comings, D.E.; Alfi, O.S. Optical studies of the interaction of 4′-6-diamidino-2-phenylindole with DNA and metaphase chromosomes. *Chromsoma* **1977**, *60*, 15–25. [CrossRef]

30. Barcellona, M.L.; Gratton, E. The fluorescence properties of a DNA probe. *Euro. Biophys. J.* **1990**, *17*, 315–323. [CrossRef]

31. Barcellona, M.L.; Cardiel, G.; Gratton, E. Time-resolved fluorescence of DAPI in solution and bound to polydeoxynucleotides. *Biochem. Biophys. Res. Commun.* **1990**, *170*, 270–280. [CrossRef]

32. Barcellona, M.L.; Gratton, E. Fluorescence lifetime distributions of DNA-4′,6-diamidino-2-phenylindole complex. *Biochim. Biophys Acta* **1989**, *993*, 174–178. [CrossRef]

33. Boger, D.L.; Fink, B.E.; Brunette, S.R.; Tse, W.C.; Hedrick, M.P. A Simple, High-Resolution Method for Establishing DNA Binding Affinity and Sequence Selectivity. *J. Am. Chem. Soc.* **2001**, *123*, 5878–5891. [CrossRef] [PubMed]

34. Ding, Y.; Zhang, L.; Xie, J.; Guo, R. Binding Characteristics and Molecular Mechanism of Interaction between Ionic Liquid and DNA. *J. Phys. Chem. B* **2010**, *114*, 2033–2043. [CrossRef]

35. Reis, L.A.; Rocha, M.S. DNA interaction with DAPI fluorescent dye: Force spectroscopy decouples two different binding modes. *Biopolymers* **2017**, *107*, e23015. [CrossRef] [PubMed]

36. Keppeler, N.; Galgano, P.D.; da Silva Santos, S.; Malek, N.I.; El Seoud, O.A. On the effects of head-group volume on the adsorption and aggregation of 1-(n-hexadecyl)-3-Cm-imidazolium bromide and chloride surfactants in aqueous solutions. *J. Mol. Liq.* **2021**, *328*, 115478. [CrossRef]

37. El Seoud, O.A.; Pires, P.A.R.; Abdel-Moghny, T.; Bastos, E.L. Synthesis and micellar properties of surface-active ionic liquids: 1-Alkyl-3-methylimidazolium chlorides. *J. Colloid. Int. Sci.* **2007**, *313*, 296–304. [CrossRef] [PubMed]

38. LaRocca, M.M.; Baker, G.A.; Heitz, M.P. Assessing rotation and solvation dynamics in ethaline deep eutectic solvent and its solutions with methanol. *J. Chem. Phys.* **2021**, *155*, 034505. [CrossRef]

39. Barra, K.M.; Sabatini, R.P.; McAtee, Z.P.; Heitz, M.P. Solvation and Rotation Dynamics in the Trihexyl(tetradecyl)phosphonium Chloride Ionic Liquid/Methanol Cosolvent System. *J. Phys. Chem. B* **2014**, *118*, 12979–12992. [CrossRef]

40. Case, D.A.; Darden, T.A.; Cheatham, T.E.; Simmerling, C.L.; Wang, J.; Duke, R.E.; Luo, R.; Crowley, M.R.; Walker, R.C.; Zhang, W.; et al. *Amber 10*; University of California: San Francisco, CA, USA, 2008.

41. Lindorff-Larsen, K.; Piana, S.; Palmo, K.; Maragakis, P.; Klepeis, J.L.; Dror, R.O.; Shaw, D.E. Improved side-chain torsion potentials for the Amber ff99SB protein force field. *Proteins* **2010**, *78*, 1950–1958. [CrossRef]

42. Martínez, J.M.; Martínez, L. Packing optimization for automated generation of complex system's initial configurations for molecular dynamics and docking. *J. Comput. Chem.* **2003**, *24*, 819–825. [CrossRef]

43. Martínez, L.; Andrade, R.; Birgin, E.G.; Martínez, J.M. PACKMOL: A package for building initial configurations for molecular dynamics simulations. *J. Comput. Chem.* **2009**, *30*, 2157–2164. [CrossRef]

44. Jorgensen, W.L.; Chandrasekhar, J.; Madura, J.D.; Impey, R.W.; Klein, M.L. Comparison of simple potential functions for simulating liquid water. *J. Chem. Phys.* **1983**, *79*, 926–935. [CrossRef]

45. Hess, B.; Bekker, H.; Berendsen, H.J.C.; Fraaije, J.G.E.M. LINCS: A linear constraint solver for molecular simulations. *J. Comput. Chem.* **1997**, *18*, 1463–1472. [CrossRef]

46. Darden, T.; York, D.; Pedersen, L. Particle mesh Ewald: An N·log(N) method for Ewald sums in large systems. *J. Chem. Phys.* **1993**, *98*, 10089–10092. [CrossRef]

47. Bussi, G.; Donadio, D.; Parrinello, M. Canonical sampling through velocity rescaling. *J. Chem. Phys.* **2007**, *126*, 014101. [CrossRef] [PubMed]

48. Abraham, M.J.; Murtola, T.; Schulz, R.; Páll, S.; Smith, J.C.; Hess, B.; Lindahl, E. GROMACS: High performance molecular simulations through multi-level parallelism from laptops to supercomputers. *SoftwareX* **2015**, *1–2*, 19–25. [CrossRef]

49. Páll, S.; Abraham, M.J.; Kutzner, C.; Hess, B.; Lindahl, E. *Solving Software Challenges for Exascale*, 1st ed.; Markidis, S., Laure, E., Eds.; Springer International Publishing: Cham, Switzerland, 2015.

50. Pronk, S.; Páll, S.; Schulz, R.; Larsson, P.; Bjelkmar, P.; Apostolov, R.; Shirts, M.R.; Smith, J.C.; Kasson, P.M.; van der Spoel, D.; et al. GROMACS 4.5: A high-throughput and highly parallel open-source molecular simulation toolkit. *Bioinfomatics* **2013**, *29*, 845–854. [CrossRef] [PubMed]

51. Hess, B.; Kutzner, C.; van der Spoel, D.; Lindahl, E. GROMACS 4: Algorithms for Highly Efficient, Load-Balanced, and Scalable Molecular Simulation. *J. Chem. Theory Comput.* **2008**, *4*, 435–447. [CrossRef]

52. Van Der Spoel, D.; Lindahl, E.; Hess, B.; Groenhof, G.; Mark, A.E.; Berendsen, H.J.C. GROMACS: Fast, flexible, and free. *J. Comput. Chem.* **2005**, *26*, 1701–1718. [CrossRef]

53. Humphrey, W.; Dalke, A.; Schulten, K. VMD: Visual molecular dynamics. *J. Mol. Graphics* **1996**, *14*, 33–38. [CrossRef]

CHAPTER 4

Surface Interaction of Ionic Liquids: Stabilization of Polyethylene Terephthalate-Degrading Enzymes in Solution

Zara, Z., Mishra, D., Pandey, S. K., Csefalvay, E., Fadaei, F., Minofar, B., & Řeha, D. (2022). Surface Interaction of Ionic Liquids: Stabilization of Polyethylene Terephthalate-Degrading Enzymes in Solution. *Molecules*, *27*(1), 119. https://doi.org/10.3390/molecules27010119

molecules

MDPI

Article

Surface Interaction of Ionic Liquids: Stabilization of Polyethylene Terephthalate-Degrading Enzymes in Solution

Zeenat Zara [1,2], **Deepti Mishra** [2], **Saurabh Kumar Pandey** [2,3], **Eva Csefalvay** [2], **Fatemeh Fadaei** [1,2], **Babak Minofar** [2,*] **and David Řeha** [2,*]

[1] Faculty of Science, University of South Bohemia in Ceske Budejovice, Branišovská 1760,
370 05 České Budějovice, Czech Republic; zeenaz00@prf.jcu.cz (Z.Z.); fadaei@nh.cas.cz (F.F.)
[2] Laboratory of Structural Biology and Bioinformatics, Institute of Microbiology of the Czech Academy of
Sciences, Zamek 136, 373 33 Nove Hrady, Czech Republic; deepti.bioinfo@gmail.com (D.M.);
saurabhkpandey@gmail.com (S.K.P.); csefalvay@nh.cas.cz (E.C.)
[3] Institute of Photonics and Electronics of the Czech Academy of Sciences, Chaberská 1014/57,
182 00 Praha 8-Kobylisy, Czech Republic
* Correspondence: minofar@nh.cas.cz (B.M.); reha@nh.cas.cz (D.Ř.)

Abstract: The effect of aqueous solutions of selected ionic liquids solutions on *Ideonella sakaiensis* PETase with bis(2-hydroxyethyl) terephthalate (BHET) substrate were studied by means of molecular dynamics simulations in order to identify the possible effect of ionic liquids on the structure and dynamics of enzymatic Polyethylene terephthalate (PET) hydrolysis. The use of specific ionic liquids can potentially enhance the enzymatic hydrolyses of PET where these ionic liquids are known to partially dissolve PET. The aqueous solution of cholinium phosphate were found to have the smallest effect of the structure of PETase, and its interaction with (BHET) as substrate was comparable to that with the pure water. Thus, the cholinium phosphate was identified as possible candidate as ionic liquid co-solvent to study the enzymatic hydrolyses of PET.

Keywords: molecular dynamics (MD) simulations; PETase; BHET; PET; ionic liquids (ILs)

check for
updates

1. Introduction

Due to the major concern on the global environmental crisis, research on how to recycle synthetic polymers has been promoted extensively for the last two decades. Among various synthetic polymers, the polyethylene terephthalate (PET), with its simple synthesis, robustness, and durability, led to a drastic increase in its industrial production; therefore, by the year 2020, production has reached more than 70 million metric tons [1–3]. Different chemical degradation approaches, e.g., hydrolysis, ammonolysis, aminolysis, methanolysis, and glycolysis have been introduced to recycle and remove the plastics. Nevertheless, these techniques need high temperatures and produce other environmental pollutants as byproducts.

The high solubility of PET in solvents, as the first step of recycling, is difficult; therefore, finding proper solvents for recycling and degrading is challenging. There are few solvents that were commonly used for PET solubilization, such as dichloroacetic acid [4,5] trifluoroacetic acid [6], phenol/1,1,2,2-tetrachloroethane solution [7], and chlorophenol [8]. Nonetheless, these solvents are not only costly but also toxic; therefore, it is desirable to use pretreated PET to avoid any secondary pollution in the environment.

The hydrophobic nature and crystallinity of PET are two major issues on dissolution and recycling of PET; therefore, finding environmentally friendly solvents is needed. Herein, ionic liquids (ILs) can be used to overcome this problem, as some ILs can partially change the crystalline structure of PET to an amorphous structure [9,10]. Moreover, as an alternative to traditionally used volatile organic compounds, many ionic liquids are environmentally friendly and some of them can enhance the stability and catalytic activity of certain enzymes [11,12]. ILs in general have unique features, such as strong solvent

power for dissolution of organic and inorganic compounds, thermal stability, non-volatility, electrochemical stability, and low flammability [13,14]. Ionic liquids can be mixed with water at various concentrations, forming so-called hydrated ionic liquids, and hence, water and ILs act as co-solvents in the solution [15–21]. At the present time, ionic liquids have attracted enormous research interest due to their specific advantages and variability, which can be achieved by optimization of the choice of cation and anion combinations, influencing thermal stability, non-volatility, and many other properties [22,23]. Ionic liquids can be used for degradation of complex polymers, as was shown for cellulose, which can be utilized by ILs [24,25]. Degradation of PET in the presence of several ILs has been reported experimentally, and the results show that ILs have increased the degradation ability of PET [4,7]. The advantage of using ILs as a co-solvent over conventional catalysts, such as metal acetates, to recycle PET is that the purification of the glycolysis products is simpler. The mechanism of action of ILs is based on the changes of the highly crystalline structure of PET film into an amorphous structure (lost crystalline structure), which can be easily attacked by PETase during catalytic degradation.

One of the methods for disposal of plastic waste is biodegradation of plastic materials by enzymes [26]. Development of these environmentally friendly methods is desirable. In the case of PET, the terephthalic (TPA) moiety present in PET is hydrophobic, which makes it resistant to the bio-degradation process. In view of this, industries are focusing more on synthesizing bio-based—rather than oil-based—polymers. Herein, microorganisms play important roles in the clean-up of pollutants released by humans within the ecosystem. The process of enzymatic hydrolysis of PET films was first reported by Müller et al. (2005). The hydrolytic enzyme was purified from the culture supernatant of *T. fusca* [27]. Recently, the bacterial strain *Ideonella sakaiensis* was discovered and shown to grow on low-crystallinity PET films while using PET as a carbon source [28–33]. The enzyme, known as PETase, showed much higher depolymerization activity against PET films at the mesophilic temperature, unlike thermophilic PET-degrading enzymes tested to date. PETase works with a two-step process of degradation, at the first step, it degrades the PET into Mono-(2-hydroxyethyl) terephthalate (MHET) and then the different enzyme MHETase degrades the MHET into TPA and ethylene glycol [34]. The unique feature of PETase from *Ideonella sakaiensis* is the fact that it degrades PET film at room temperature, unlike other hydrolases, which function only at high temperatures [35,36]. This confirms the unique structural and sequence features of *Ideonella sakaiensis* PETase. Additionally, experiments reveal that *Ideonella sakaiensis* PETase exhibits the highest activity among the other thermophilic PET degrading enzymes [4,37].

Here, we report molecular dynamics (MD) simulations of *Ideonella sakaiensis* PETase with various ionic liquids in order to understand the effect of aqueous solutions of ILs on the structure of PETase and the catalytic/active site of PETase in the presence of ILs. For MD simulations, the wild-type of *Ideonella sakaiensis* PETase with ligand (bis(2-hydroxyethyl) terephthalate (BHET)) have been simulated in pure water and in different concentrations of three different ionic liquids, which were used as a solvent for dissolution of PET.

2. Results and Discussion

2.1. Root Mean Square Deviation (RMSD)

In order to investigate the effect of non-aqueous solvent on the complex structure of *Ideonella sakaiensis* PETase with ligand (BHET), we performed here MD simulations with three different ionic liquids (Figure 1) in three different concentrations (20%, 30%, 40%) by mass.
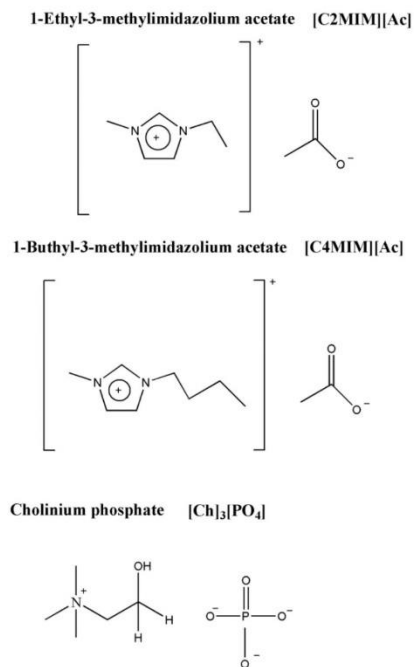
1-Ethyl-3-methylimidazolium acetate   [C2MIM][Ac]

1-Buthyl-3-methylimidazolium acetate   [C4MIM][Ac]

Cholinium phosphate   [Ch]₃[PO₄]

Figure 1. Chemical structures of 1-Ethyl-3-methylimidazolium acetate [C2MIM][Ac], 1-Butyl-3-methylimidazolium acetate [C4MIM][Ac] and Cholinium phosphate [Ch]$_3$[PO$_4$].

The comparison of the wild-type *Ideonella sakaiensis* PETase structures in different solvents after 150 ns of MD simulation is shown in Figure 2, where the PETase backbone in different solvents was superimposed.
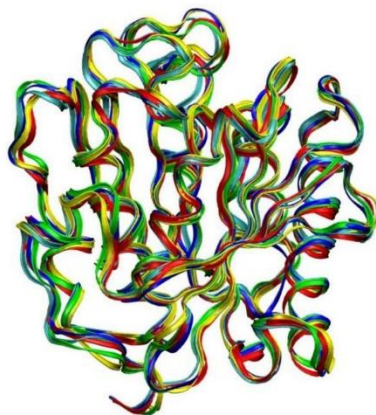

Figure 2. PETase backbone structure is superimposed with different solvents. The wild-type crystal structure is in blue. MD simulation for 150 ns with water as a solvent is in red. Simulation with [Ch]$_3$[PO$_4$], [C4MIM][Ac] and [C2MIM][Ac] is represented in yellow, green, and light blue, respectively.

Simulation of the PETase complex with the ligand in water was kept as a control. Calculating the root mean square deviation (RMSD) of proteins permits the quantification of the degree of stability of the enzyme during the MD simulations. Here, in Figure 3 we have shown RMSD of backbone atoms of PETase in three different ionic liquids and in water.
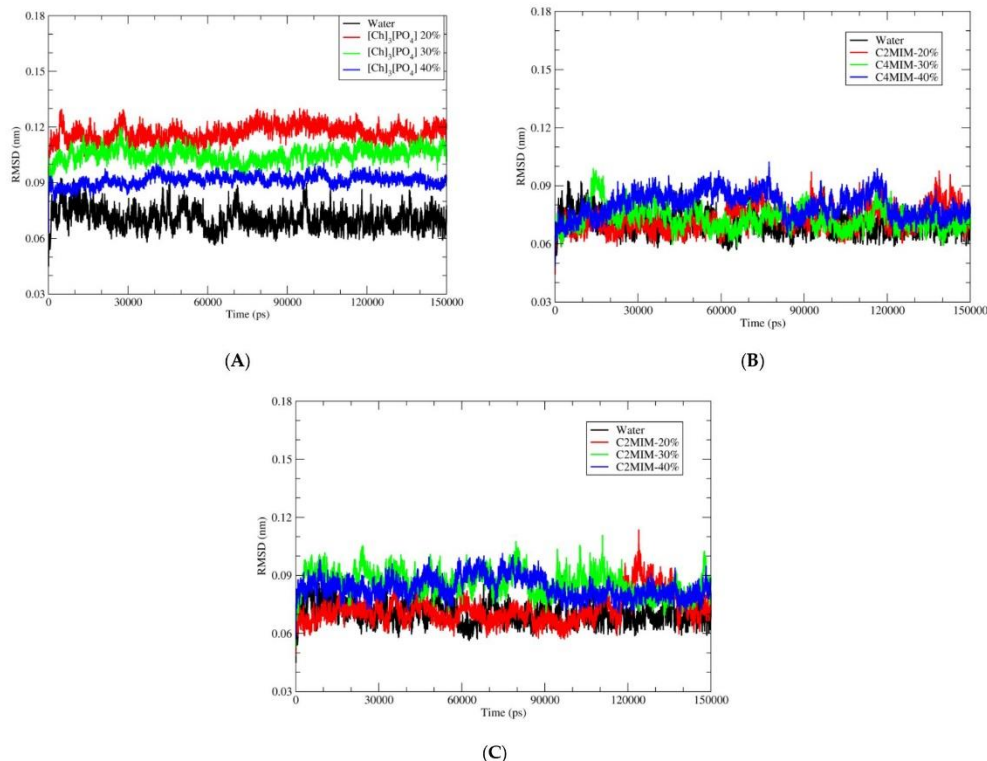

(A)

(B)

(C)

Figure 3. Root mean square deviation (RMSD) of Cα atoms of wild type of PETase with water and three different ionic liquids solutions. (**A**) Pure water in black; 20% of [Ch]$_3$[PO$_4$] in red; 30% of [Ch]$_3$[PO$_4$] in green and 40% of [Ch]$_3$[PO$_4$] in blue. (**B**) Pure water in black; 20% of [C4MIM][Ac] in red; 30% of [C4MIM][Ac] in green and 40% of [C4MIM][Ac] in blue. (**C**) Pure water in black; 20% of [C2MIM][Ac] in red; 30% of [C2MIM][Ac] in green and 40% of [C2MIM][Ac] in blue.

As depicted in Figure 3, RMSD values for PETase in water is lower than in ionic liquids during MD simulation of all systems, indicating that PEtase structure in water is closer to the crystal structure than the structures in ionic liquids. On the other hand, the fluctuation of RMSD decreases with increased concertation of ILs, indicating more stable structures with less thermal fluctuations. Figure 3A shows the deviation of backbone atoms with respect to the reference structure (PDB code 5XJH) when inserted in water and in [Ch]$_3$[PO$_4$] ionic liquid with 3 different percentages: 40%, 30%, and 20%. We observed that the overall structure of PETase is not deviating much from its starting structure which implies that the chosen ionic liquids [Ch]$_3$[PO$_4$] would not significantly alter the enzyme structure and it is suitable for further studies on the reaction mechanism of BHET hydrolysis. We further investigate two other ionic liquids, [C4MIM][Ac] and [C2MIM][Ac]. In both [C4MIM][Ac] and [C2MIM][Ac] ionic liquids, we have not observed significant deviation of backbone

atom of PETase with the addition of these ILs. The RMSD graphs for [C4MIM][Ac] and [C2MIM][Ac] is shown in Figure 3B,C, respectively.

2.2. Ligand RMSD

Analysis in the previous section showed that the enzyme structure is quite stable and not deviated much from the crystal structure after immersing into three different ionic liquid solutions. Now, the next main step is to see the reaction site of PETase, where catalytic triad (facilitating the BHET hydrolysis) is present on the active site of the enzyme. The ligand BHET is surrounded by three catalytic amino acids, which will help BHET hydrolysis through SN-2 reaction mechanism. For this purpose, the position of the BHET ligand should be stable during MD simulations in the presence of different solvents. Therefore, we have plotted the RMSD of BHET atoms during the simulation in order to identify the stability of BHET atoms. The RMSD of the ligand, with respect to the PETase, was calculated during the simulation time of 150 ns. Here, as depicted in Figure 4A, the BHET atoms are not deviating much from their starting structure in the presence of $[Ch]_3[PO_4]$.
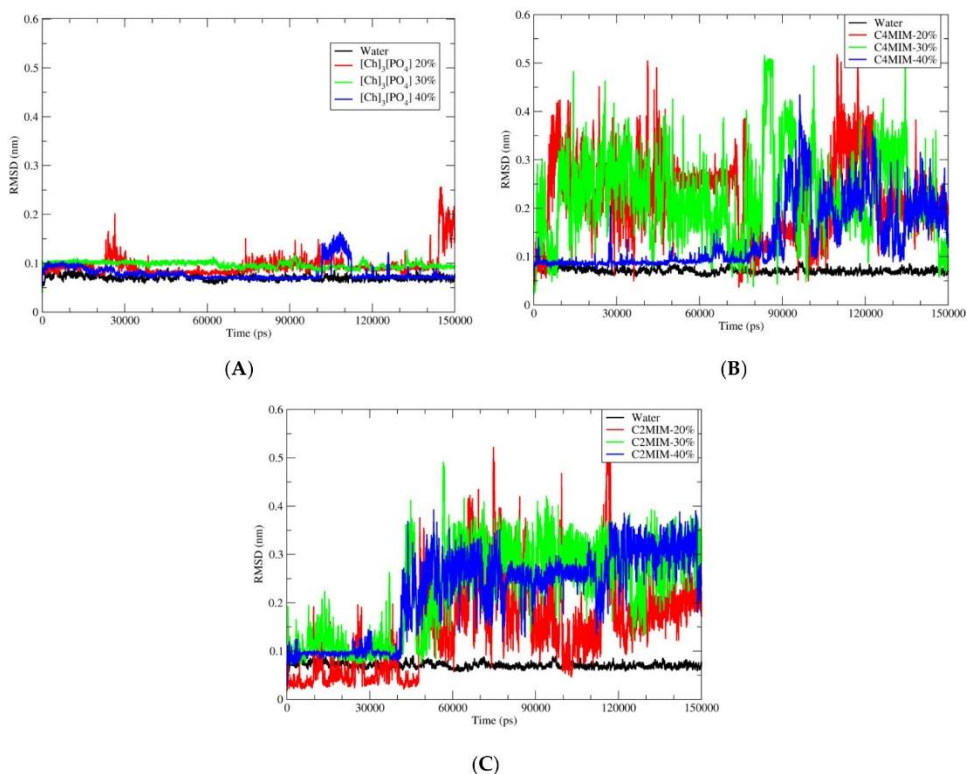

(**A**)   (**B**)

(**C**)

Figure 4. Root mean square deviation (RMSD) of BHET with respect to PETase in water and three different ionic liquids solutions. (**A**) Pure water in black; 20% of $[Ch]_3[PO_4]$ in red; 30% of $[Ch]_3[PO_4]$ in green and 40% of $[Ch]_3[PO_4]$ in blue. (**B**) Pure water in black; 20% of [C4MIM][Ac] in red; 30% of [C4MIM][Ac] in green and 40% of [C4MIM][Ac] in blue. (**C**) Pure water in black; 20% of [C2MIM][Ac] in red; 30% of [C2MIM][Ac] in green and 40% of [C2MIM][Ac] in blue.

As shown in graph Figure 4A, the ligand is quite stable in pure aqueous media and in the presence of $[Ch]_3[PO_4]$ ionic liquid. However, the same stability trend has not

been observed in the case of [C4MIM][Ac] or [C2MIM][Ac] ionic liquids, as shown in Figure 4B,C, respectively. A detailed inspection of the trajectory revealed that after 40 ns, the BHET molecule starts moving away from catalytic triad residue ser-131 and the BHET molecule starts bending from the central carbonyl carbon due to non-bonding interaction between two sites of BHET rings. The same trend of instability of BHET was observed for [C4MIM][Ac] after 40 ns of MD simulation, whereas the stabilization in the presence of [Ch]$_3$[PO$_4$] and pure water for the entire simulation indicated no significant deviation of the geometry and position of BHET molecule within PETase. Furthermore, when the concentration of ionic liquids decreased to 30% and 20%, the instability of BHET increased for [C2MIM][Ac] and [C4MIM][Ac]. Again, the molecule started to bend from the carbonyl carbon and this might be due to electrostatic interaction between two sites of BHET. The BHET structure was quite stable for the whole simulation time of 150 ns in the presence of [Ch]$_3$[PO$_4$] and pure water.

2.3. Root Mean Square Fluctuation (RMSF)

In order to have a deep insight into structural stability, one can analyze the stability of each residue over the simulation time. The flexibility and stability of each residue is investigated by RMSF. As shown in Figure 5, the RMSF values of PETase in 40% [Ch]$_3$[PO$_4$] are lower than in water, which is consistent with RMSD fluctuation in Figure 3.
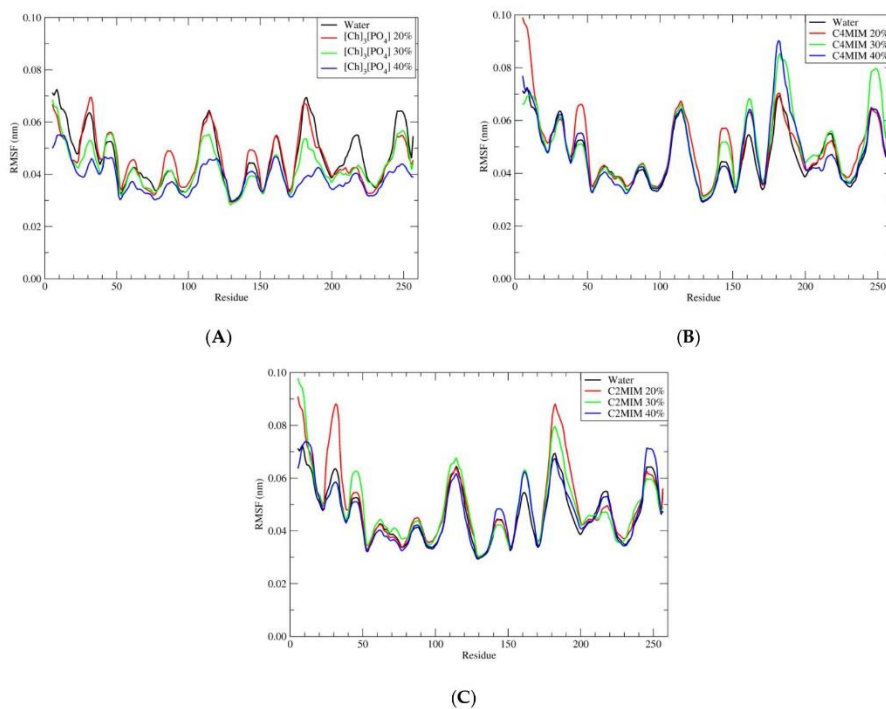

(**A**)

(**B**)

(**C**)

Figure 5. Root mean square fluctuation (RMSF) of wild-type of PETase with water and three different ionic liquids solutions in the presence of ligand BHET. (**A**) Pure water in black; 20% of [Ch]$_3$[PO$_4$] in red; 30% of [Ch]$_3$[PO$_4$] in green and 40% of [Ch]$_3$[PO$_4$] in blue. (**B**) Pure water in black; 20% of [C4MIM][Ac] in red; 30% of [C4MIM][Ac] in green and 40% of [C4MIM][Ac] in blue. (**C**) Pure water in black; 20% of [C2MIM][Ac] in red; 30% of [C2MIM][Ac] in green and 40% of [C2MIM][Ac] in blue.

The residues which are fluctuating more are at residue positions 100–120 and 170–180. Among these two domains, we have found that the residue Asn-183 has the highest value of RMSF and it is the most unstable one. The same residue has the highest RMSF also in the presence of [C4MIM][Ac] and [C2MIM][Ac] ionic liquid.

To understand this further, we performed a detailed inspection of the simulations and found that [Ch]$_3$[PO$_4$] with 40% concentration has a strong hydrogen bond interaction between the residue Asn-183 and PO$_4^{3-}$. One hydrogen bond interaction between the hydrogen atom of residue Asn-183 of the PETase enzyme with the oxygen of phosphate group PO$_4^{3-}$ was observed. This hydrogen bond interaction was with the bond distance of 1.8 Å to 3 Å. However, we noticed that it was not stable enough over the simulation. This makes the residue Asn-183 stable relatively when we have [C4MIM][Ac] and [C2MIM][Ac] as solvents. There was no eligible entity in [C4MIM][Ac] and [C2MIM][Ac] to have an interaction with residue Asn183 and, as a result, the residue was unstable in the presence of both [C4MIM][Ac] and [C2MIM][Ac]ionic liquids; therefore, producing the higher root mean square fluctuation value.

2.4. Radius of Gyration

Calculating the radius of gyration of a protein is a measurement of its compactness. Thus, if a protein is stably compact, it will maintain a relatively stable value of R$_g$ over the simulation of time. However, if a protein unfolds during the simulation of time, the R$_g$ value will fluctuate. Therefore, the measurement of the compactness of protein is investigated by the radius of gyration function. The radius of gyration of each simulated system is calculated and compared between simulations in water and simulations in ionic liquid. There were no structural distortions or unfolding of the secondary structure during 150 ns simulations. However, PETase in water possesses a low radius of gyration relatively with simulated ionic liquid systems. As shown in Figure 6, the protein in ionic liquids have a radius of gyration from 1.66 to 1.68 nm, which is larger than in water, where the radius of gyration was around 1.64 nm. This indicates that the protein has a slightly less compact structure in ILs than in water. This can be explained by interactions of the IL's ions with protein instead of the water molecules. The protein radius of gyration in ILs at different concentrations is comparable, except the [Ch]$_3$[PO$_4$] at 40%, where R$_g$ is slightly lower at 1.66 compared with 1.67 in [C2MIM][Ac] and [C4MIM][Ac]. This is most likely due to local higher concentration of the [PO$_4$], which (in comparison to then [CXMIM] and [Ac]) is less likely to disrupt local geometry of the water molecules in the vicinity of the protein (see Hofmeister series [38]).

After analyzing the overall structure of PETase, we focused on the active site of PETase, where BHET ligand binds and is degraded into smaller units through the catalytic reaction. The catalytic triad is present on the protein surface. The triad is composed of Serine 131, Histidine 208, and Aspartic acid 177. We investigated the distance between our ligand (BHET) carbonyl carbon and oxygen of Ser-131. In order to understand the stability of the interaction between ligand and catalytic residue, the distance between the ligand and Ser-131 in the presence of water and all ionic liquids in all three ionic concentrations was calculated over the whole duration of MD simulation. As depicted in Figure 7, the distance between these two residues is stable over the simulation in water and in [Ch]$_3$[PO$_4$] as shown in Figure 7A.
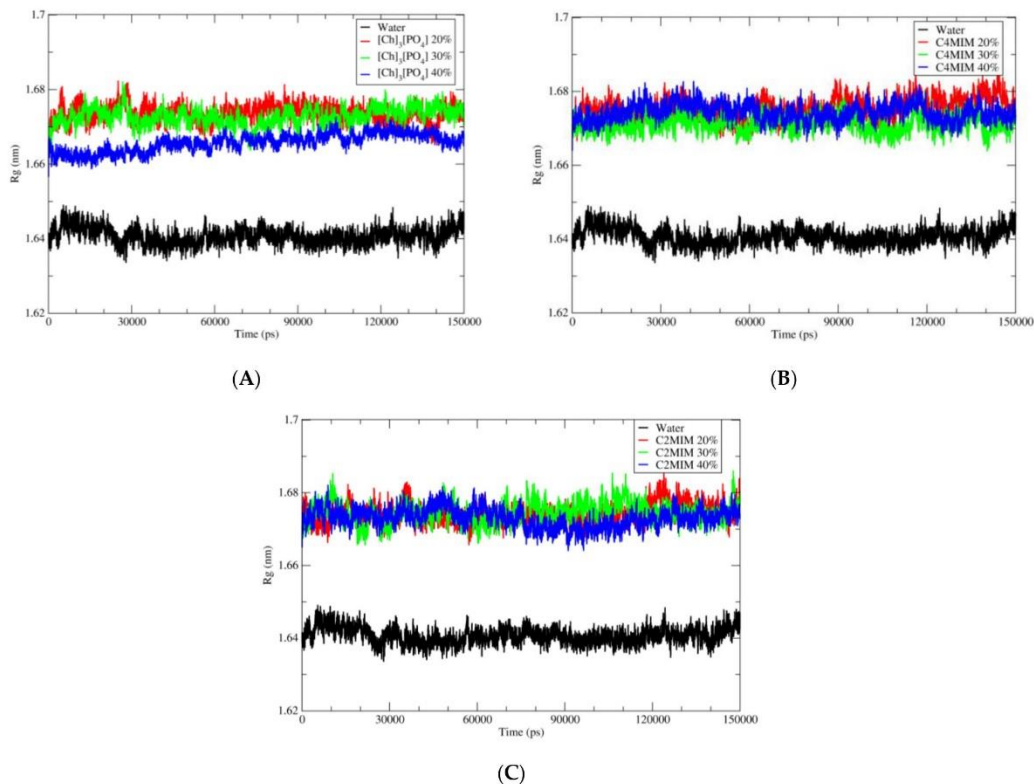
(**A**)

(**B**)

(**C**)

Figure 6. Radius of gyration (Rg) graph of wild-type PETase in complex with BHET ligand in the presence of different solvents. (**A**) Pure water in black; 20% of $[Ch]_3[PO_4]$ in red; 30% of $[Ch]_3[PO_4]$ in green and 40% of $[Ch]_3[PO_4]$ in blue. (**B**) Pure water in black; 20% of [C4MIM][Ac] in red; 30% of [C4MIM][Ac] in green and 40% of [C4MIM][Ac] in blue. (**C**) Pure water in black; 20% of [C2MIM][Ac] in red; 30% of [C2MIM][Ac] in green and 40% of [C2MIM][Ac] in blue.

The black curve shows the distance in the water and the blue one with $[Ch]_3[PO_4]$ at 40% concentration. This shows the stability of ligand during the simulation; hence the condition that is favorable for the reaction is maintained. Therefore, one can consider $[Ch]_3[PO_4]$ ionic liquid as a possible medium for BHET hydrolysis. However, in the case of [C4MIM][Ac] and [C2MIM][Ac], the distance fluctuates significantly during the simulation, which implies the instability of ligand on the active site of PETase. Among the ionic liquids, $[Ch]_3[PO_4]$ illustrated the best result for maintaining ligand stability at the catalytic site.
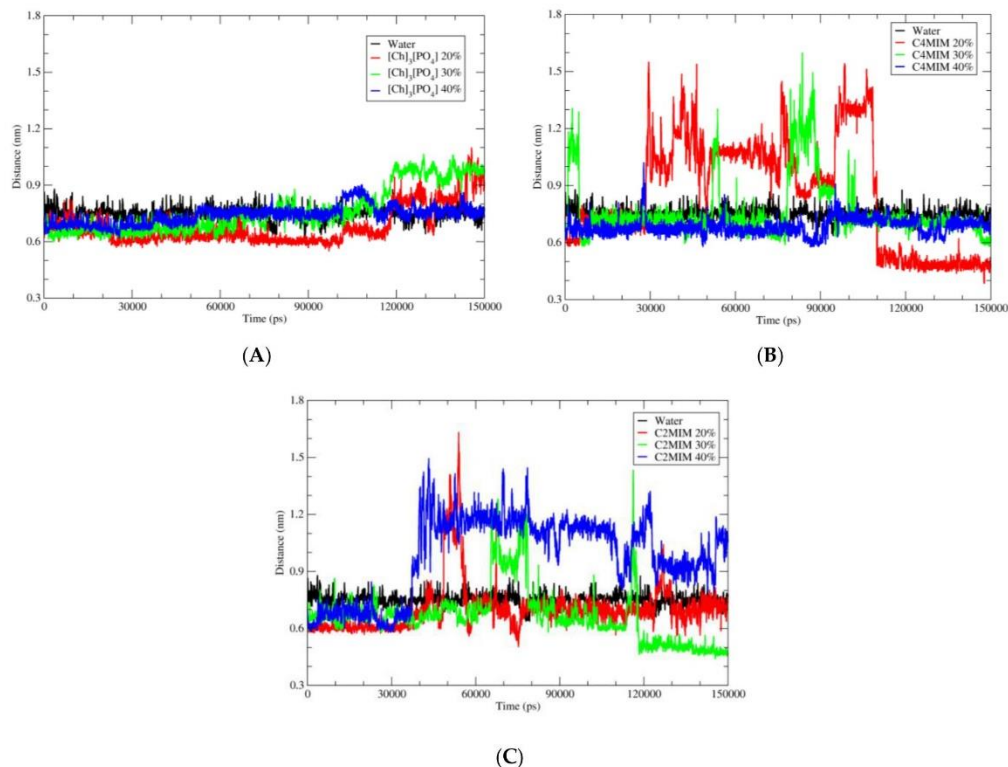
(A)

(B)

(C)

Figure 7. Distance between the C of carbonyl group of BHET with the O of Ser-131 in water and different ionic liquids solutions. (**A**) Pure water in black; 20% of [Ch]$_3$[PO$_4$] in red; 30% of [Ch]$_3$[PO$_4$] in green and 40% of [Ch]$_3$[PO$_4$] in blue. (**B**) Pure water in black; 20% of [C4MIM][Ac] in red; 30% of [C4MIM][Ac] in green and 40% of [C4MIM][Ac] in blue. (**C**) Pure water in black; 20% of [C2MIM][Ac] in red; 30% of [C2MIM][Ac] in green and 40% of [C2MIM][Ac] in blue.

2.5. Hydrogen Bonds and Hydrophobic Interaction

The solubility and stability of a protein are also dependent on its solvent interaction. The solvent interaction can stabilize or destabilize the amino acids of the protein. Moreover, the hydrogen bond interaction plays an important role in the overall stability of the protein structure. Thus, the number of H bonds with the protein demonstrates its structural stability.

As shown in Figure 8, the number of H bonds of water molecules, cholinium, and phosphate ions with protein residues were calculated in different ionic liquid concentrations. Here, 40%, 30%, and 20% concentrations of each system were calculated by adding the solvent values for a separate system.

Figure 8 illustrated that, when pure water was replaced with aqueous solutions of ionic liquids, the number of hydrogen bonds decreased, probably due to the bigger size of cation and anions. Furthermore, the number of H bonds in the 20% solution is higher than the one in the 40% solution. However, in the case of water-[C4MIM][Ac] and water-[C2MIM][Ac] (Supplementary data Figure S1A,B), the [C4MIM] and [C2MIM] cations do not play important role for H bonding with the PETase, as they do not have groups that promote H bonds. However, there is no significant change in H bonds for different concentrations of [C4MIM][Ac] and [C2MIM][Ac].
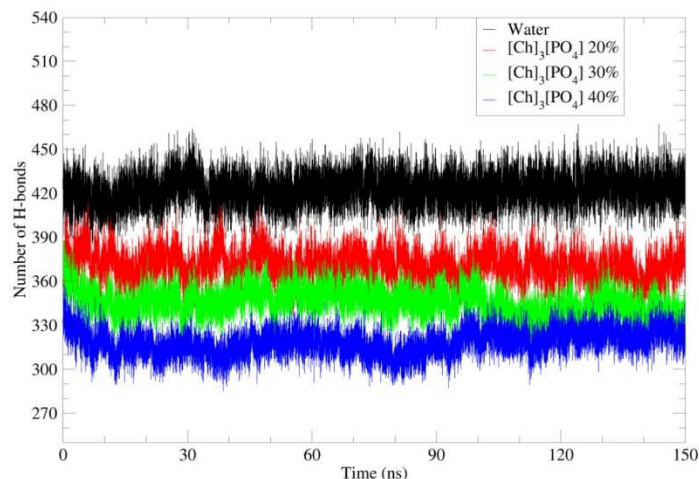
Figure 8. Number of hydrogen bonds of water and cholinium phosphate with amino acids of PETase in 40%, 30%, and 20% IL solutions. Pure water in black; 20% of [Ch]$_3$[PO$_4$] in red; 30% of [Ch]$_3$[PO$_4$] in green and 40% of [Ch]$_3$[PO$_4$] in blue.

Furthermore, the hydrophobic amino acids are also located at the surface of PETase, which are not solvated by water molecules. Therefore, they interact more with the hydrophobic part of [C4MIM], [C2MIM], and cholinium cations. The hydrophobic interaction took place between hydrophobic amino acids, such as A123, F26, P145, A197, P9, A11, F232, and F162, and methyl groups of cholinium, hydrocarbon (-CH$_2$-CH$_3$), or the imidazolium ring of [C4MIM] and [C2MIM] cation. Hence, cholinium cations (Figure 9), [C4MIM] and [C2MIM] (Supplementary data Figure S2A,B) are mainly distributed over the hydrophobic surface of PETase.
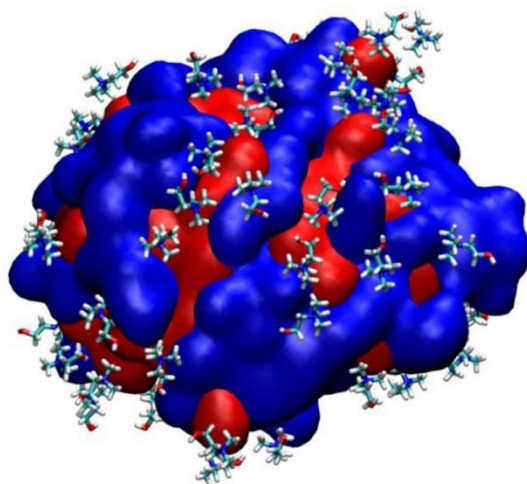

Figure 9. The interaction of cholinium cations with hydrophobic surface of PETase. The hydrophobic surface is colored in red and the hydrophilic surface is colored in blue.

2.6. Radial Distribution Function

The radial distribution function (RDF)—the probability of finding a particle from a reference particle over distance—is a powerful tool in MD simulations for understanding how the $(CH3)_3N^+$ group of cholinium cation, the ring of imidazolium [C4MIM], and [C2MIM] are distributed around the side chain of the hydrophobic surface amino acids.

The RDF of the $(CH_3)_3N^+$ group of cholinium cation around the side chain of hydrophobic amino acids at the protein surface (such as A_123, F_26, P_145, A_197, and P_9), the RDF of the ring of [C4MIM] around the side chain of hydrophobic amino acids at the protein surface (such as A_123, A1_1, F_232, P_9, and F_162), and the RDF of the ring of [C2MIM] around side chain of hydrophobic amino acids at the protein surface (such as A_123, A_11, F_232, P_9, and F_162), were calculated, and the results are shown in Figure 10, Supplementary data Figure S3, and Supplementary data Figure S4, respectively.
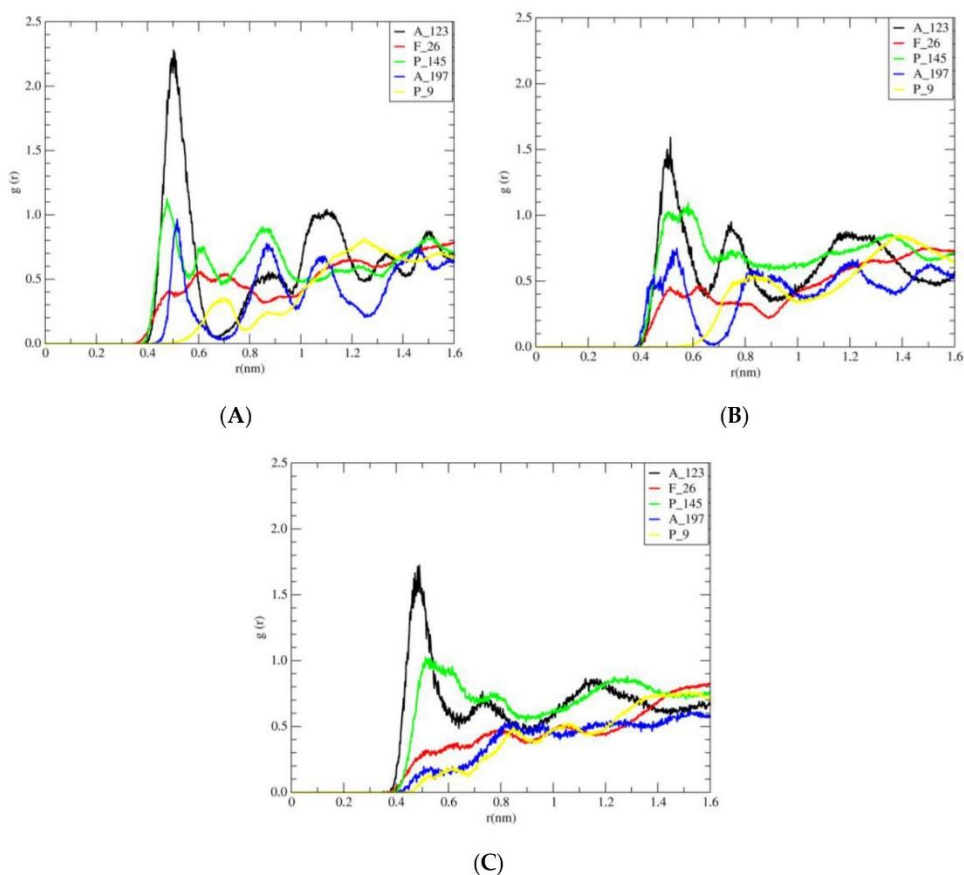

(A)

(B)

(C)

Figure 10. Radial distribution functions (RDFs) for atoms with (**A**) side chain of amino acids A_123 (in black), F_26 (in red), P_145 (in green), A_197 (in blue), and P_9 (in yellow) of the hydrophobic surface and nitrogen of cholinium cations in 40% of [Ch]$_3$[PO$_4$]. (**B**) Side chain of amino acids A_123, F_26, P_145, A_197, and P_9 of the hydrophobic surface and nitrogen of cholinium cations in 30% of [Ch]$_3$[PO$_4$]. (**C**) Side chain of amino acids A_123, F_26, P_145, A_197, and P_9 of the hydrophobic surface and nitrogen of cholinium cations in 20% of [Ch]$_3$[PO$_4$].

As shown in Figure 10, in different concentrations (40%, 30%, and 20%), the height of the first peak (A_123) of the distribution function is larger than the rest of the amino acids. According to Figure S3, in different concentrations (40%, 30%, and 20% of [C4MIM][Ac]), the height of the first peak (A_123) in the radial distribution function is greater. As shown in Figure S4, in all designed systems of [C2MIM][Ac] in different concentrations 40%, 30%, and 20%, the height of the first peak (A_123) of the RDF is larger than the rest. Thus, in accordance with Figure 10 through Figure S4, the height of the first peak (A_123) for different ionic liquids is as follows:

Alkyl groups of [C2MIM] cation < Alkyl groups of [C4MIM] cation < methyl groups of cholinium cation.

On the other hand, the highest peak in RDF corresponds to the probability of methyl groups of cholinium cation around the methyl group of A_123 (Figure 10). From Figure 10, can be seen that methyl groups of cation showed insignificant differences of probability density around the rings of F_26 and P_9. As it was expected from A_123 and P145, the probability density of methyl groups of cholinium cation was more for the methyl group (side chain) of A_123 than for the ring of P_145.

Furthermore, by decreasing the concentration of $[Ch]_3[PO_4]$, the density of cations around A_123 is also decreased. It can be also concluded that with the increase in the length of the alkyl chain from [C2MIM] to [C4MIM], the density of the cations around A_123 increased, but by increasing the concentration (from 20% to 40%) of [C2MIM][Ac] and [C4MIM][Ac], the change in the density of these cations is not significant. Thus, the effect of crowding on the stability of the hydrophobic surface is more pronounced in the presence of $[Ch]_3[PO_4]$ than other ionic liquids.

3. Materials and Methods

Several different model systems were set up to perform molecular dynamics simulations of wild-type *Ideonella sakaiensis* PETase enzyme with the PDB code of 5XJH [39]. The simulation systems with three different concentration of three ILs of 1-ethyl-3-methylimidazolium acetate [C2MIM][Ac], 1-butyl-3-methylimidazolium acetate [C4MIM][Ac], and cholinium phosphate (choline phosphate) $[Ch]_3[PO_4]$ were prepared. Recent studies reveal that $[Ch]_3[PO_4]$ is a bi-functional media, capable of both high solubilization (solvent) and effective depolymerization (catalyst) of PET [4]. Furthermore, $[Ch]_3[PO_4]$ is also an effective depolymerizer (catalysts). Furthermore, the lower cost of cholinium phosphate $[Ch]_3[PO_4]$ ionic liquid has quite a good ability to dissolve PET (10 wt%) [4]. Hence, the initial structures with these ionic liquids were setup using PACKMOL [40]. As a control, the PETase enzyme was also simulated in pure aqueous media. The ligand presented in our study has two TPA rings, which are called BHET. Parametrization of the ligand and ILs were carried out using general amber force field GAFF [41], as this forcefield can accurately predict thermodynamic and transport properties of various ionic liquids [42], and we have successfully used it in our previous calculations with ILs [43,44]. Each system was placed in a cubic box, sized 12 nm, using PACKMOL program package. Each model system has been neutralized by counterions. The system was first equilibrated in canonical ensemble (NVT) for 500 ps at 300 K temperature followed by the NPT—the isothermal isobaric ensemble. The temperature was maintained at 300 K and the pressure was maintained at 1bar with compressibility of 4.6×10^{-5}/bar by weak coupling to temperature and pressure baths using the Berendsen method [45] with relaxation times of 0.1 ps. Van der Waals forces were evaluated with a Lennard-Jones potential, having 10 Å cut-off, and long-range electrostatic contributions were evaluated using the particle mesh Ewald method [46] with a direct interaction cut-off of 10.0 Å. A time step of 2 fs was employed. Lengths of all covalent bonds were constrained by the linear constraint solver algorithm (LINCS) [47]. All simulations were run with periodic boundary conditions for 150 ns. The MD simulations and related analyses were performed using the GROMACS program package [48–50]. Molecular graphics images were produced using VMD [51] software and all the graphs were prepared using xmgrace program.

4. Conclusions

In the current study, the structural basis of the possible co-solvent candidates for the stability of PETase were analyzed and their interaction patterns were compared. The in silico-based investigation, using MD simulations, provides new insights into the interacting residues of the protein with the ionic liquids and water. The effect of ionic liquids cholinium phosphate [Ch]$_3$[PO$_4$], 1-butyl-3-methyl- imidazolium acetate [C4MIM][Ac], 1-ethyl-3-methyl-imidazolium acetate [C2MIM][Ac], and their water solutions on *Ideonella sakaiensis* PETase with BHET substrate were investigated. Moreover, after the careful structural and interactive analyses of the ligand with the PETase, it is concluded that among all the above mentioned ionic liquids, [Ch]$_3$[PO$_4$] has the smallest effect of the structure of PETase and its interaction with the BHET substrate, which is comparable to the pure water solvent. This makes the water solution with [Ch]$_3$[PO$_4$] a good candidate for the solvent used during BHET hydrolysis, which can be used for future investigation.

References

1. Cimpan, C.; Bjelle, E.L.; Stromman, A.H. Plastic packaging flows in Europe: A hybrid input-output approach. *J. Ind. Ecol.* **2021**, *25*, 1572–1587. [CrossRef]
2. Rochman, C.M.; Browne, M.A.; Halpern, B.S.; Hentschel, B.T.; Hoh, E.; Karapanagioti, H.K.; Rios-Mendoza, L.M.; Takada, H.; Teh, S.; Thompson, R.C. Classify plastic waste as hazardous. *Nature* **2013**, *494*, 169–171. [CrossRef]
3. Geyer, R.; Jambeck, J.R.; Law, K.L. Production, use, and fate of all plastics ever made. *Sci. Adv.* **2017**, *3*, e1700782. [CrossRef] [PubMed]
4. Sun, J.; Liu, D.; Young, R.P.; Cruz, A.G.; Isern, N.G.; Schuerg, T.; Cort, J.R.; Simmons, B.A.; Singh, S. Solubilization and Upgrading of High Polyethylene Terephthalate Loadings in a Low-Costing Bifunctional Ionic Liquid. *ChemSusChem* **2018**, *11*, 781–792. [CrossRef] [PubMed]
5. Todd, A.D.; McEneany, R.J.; Topolkaraev, V.A.; Macosko, C.W.; Hillmyer, M.A. Reactive compatibilization of poly (ethylene terephthalate) and high-density polyethylene using amino-telechelic polyethylene. *Macromolecules* **2016**, *49*, 8988–8994. [CrossRef]

6. Shi, H.; Tang, A.; Liang, Q.; Jiang, Y. Synthesis and hydrophobic properties of F & Si containing poly (ethylene terephthalate). *RSC Adv.* **2016**, *6*, 106540–106546.
7. Wang, H.; Li, Z.; Liu, Y.; Zhang, X.; Zhang, S. Degradation of poly (ethylene terephthalate) using ionic liquids. *Green Chem.* **2009**, *11*, 1568–1575. [CrossRef]
8. Chaudhary, N.; Koiry, S.; Singh, A.; Tillu, A.; Jha, P.; Samanta, S.; Debnath, A.; Aswal, D.; Mondal, R.; Acharya, S. Electron beam induced modifications in flexible biaxially oriented polyethylene terephthalate sheets: Improved mechanical and electrical properties. *Mater. Chem. Phys.* **2017**, *189*, 237–244. [CrossRef]
9. Samak, N.A.; Jia, Y.; Sharshar, M.M.; Mu, T.; Yang, M.; Peh, S.; Xing, J. Recent advances in biocatalysts engineering for polyethylene terephthalate plastic waste green recycling. *Environ. Int.* **2020**, *145*, 106144. [CrossRef]
10. Wallace, N.E.; Adams, M.C.; Chafin, A.C.; Jones, D.D.; Tsui, C.L.; Gruber, T.D. The highly crystalline PET found in plastic water bottles does not support the growth of the PETase-producing bacterium Ideonella sakaiensis. *Environ. Microbiol. Rep.* **2020**, *12*, 578–582. [CrossRef]
11. Olivier-Bourbigou, H.; Magna, L.; Morvan, D. Ionic liquids and catalysis: Recent progress from knowledge to applications. *Appl. Catal. A Gen.* **2010**, *373*, 1–56. [CrossRef]
12. Moniruzzaman, M.; Nakashima, K.; Kamiya, N.; Goto, M. Recent advances of enzymatic reactions in ionic liquids. *Biochem. Eng. J.* **2010**, *48*, 295–314. [CrossRef]
13. Hadad, C.; Husson, E.; Van Nhien, A.N. Conversion of Chitin in Ionic Liquids. In *Encyclopedia of Ionic Liquids*; Springer: Singapore, 2020; pp. 1–6.
14. Bubalo, M.C.; Radošević, K.; Redovniković, I.R.; Slivac, I.; Srček, V.G. Toxicity mechanisms of ionic liquids. *Arch. Ind. Hyg. Toxicol.* **2017**, *68*, 171–179. [CrossRef] [PubMed]
15. Roosen, C.; Müller, P.; Greiner, L. Ionic liquids in biotechnology: Applications and perspectives for biotransformations. *Appl. Microbiol. Biotechnol.* **2008**, *81*, 607–614. [CrossRef] [PubMed]
16. Gorke, J.; Srienc, F.; Kazlauskas, R. Toward advanced ionic liquids. Polar, enzyme-friendly solvents for biocatalysis. *Biotechnol. Bioprocess Eng.* **2010**, *15*, 40–53. [CrossRef] [PubMed]
17. Halle, B. Protein hydration dynamics in solution: A critical survey. *Philos. Trans. R. Soc. Lond. Ser. B Biol. Sci.* **2004**, *359*, 1207–1224. [CrossRef] [PubMed]
18. Klibanov, A.M. Improving enzymes by using them in organic solvents. *Nature* **2001**, *409*, 241–246. [CrossRef]
19. Constatinescu, D.; Herrmann, C.; Weingärtner, H. Patterns of protein unfolding and protein aggregation in ionic liquids. *PCCP* **2010**, *12*, 1756–1763. [CrossRef] [PubMed]
20. Page, T.A.; Kraut, N.D.; Page, P.M.; Baker, G.A.; Bright, F.V. Dynamics of loop 1 of domain I in human serum albumin when dissolved in ionic liquids. *J. Phys. Chem. B* **2009**, *113*, 12825–12830. [CrossRef] [PubMed]
21. Akdogan, Y.; Junk, M.J.; Hinderberger, D. Effect of ionic liquids on the solution structure of human serum albumin. *Biomacromolecules* **2011**, *12*, 1072–1079. [CrossRef]
22. Micaelo, N.M.; Soares, C.M. Protein structure and dynamics in ionic liquids. Insights from molecular dynamics simulation studies. *J. Phys. Chem. B* **2008**, *112*, 2566–2572.
23. Klähn, M.; Lim, G.S.; Seduraman, A.; Wu, P. On the different roles of anions and cations in the solvation of enzymes in ionic liquids. *PCCP* **2011**, *13*, 1649–1662. [CrossRef] [PubMed]
24. Wang, H.; Gurau, G.; Rogers, R.D. Ionic liquid processing of cellulose. *Chem. Soc. Rev.* **2012**, *41*, 1519–1537. [CrossRef]
25. Xu, A.R.; Wang, F. Carboxylate ionic liquid solvent systems from 2006 to 2020: Thermal properties and application in cellulose processing. *Green Chem.* **2020**, *22*, 7622–7664. [CrossRef]
26. Tournier, V.; Topham, C.; Gilles, A.; David, B.; Folgoas, C.; Moya-Leclair, E.; Kamionka, E.; Desrousseaux, M.-L.; Texier, H.; Gavalda, S. An engineered PET depolymerase to break down and recycle plastic bottles. *Nature* **2020**, *580*, 216–219. [CrossRef]
27. Müller, R.J.; Schrader, H.; Profe, J.; Dresler, K.; Deckwer, W.D. Enzymatic degradation of poly (ethylene terephthalate): Rapid hydrolyse using a hydrolase from T. fusca. *Macromol. Rapid Commun.* **2005**, *26*, 1400–1405. [CrossRef]
28. Sinha, V.; Patel, M.R.; Patel, J.V. PET waste management by chemical recycling: A review. *J. Polym. Environ.* **2010**, *18*, 8–25. [CrossRef]
29. Liu, B.; He, L.; Wang, L.; Li, T.; Li, C.; Liu, H.; Luo, Y.; Bao, R. Protein crystallography and site-direct mutagenesis analysis of the poly (ethylene terephthalate) hydrolase PETase from Ideonella sakaiensis. *ChemBioChem* **2018**, *19*, 1471–1475. [CrossRef]
30. Yang, Y.; Yang, J.; Jiang, L. Comment on "A bacterium that degrades and assimilates poly (ethylene terephthalate)". *Science* **2016**, *353*, 759. [CrossRef] [PubMed]
31. Yoshida, S.; Hiraga, K.; Takehana, T.; Taniguchi, I.; Yamaji, H.; Maeda, Y.; Toyohara, K.; Miyamoto, K.; Kimura, Y.; Oda, K. A bacterium that degrades and assimilates poly (ethylene terephthalate). *Science* **2016**, *351*, 1196–1199. [CrossRef]
32. Bornscheuer, U.T. Feeding on plastic. *Science* **2016**, *351*, 1154–1155. [CrossRef]
33. Han, X.; Liu, W.; Huang, J.-W.; Ma, J.; Zheng, Y.; Ko, T.-P.; Xu, L.; Cheng, Y.-S.; Chen, C.-C.; Guo, R.-T. Structural insight into catalytic mechanism of PET hydrolase. *Nat. Commun.* **2017**, *8*, 1–6. [CrossRef]
34. Palm, G.J.; Reisky, L.; Böttcher, D.; Müller, H.; Michels, E.A.; Walczak, M.C.; Berndt, L.; Weiss, M.S.; Bornscheuer, U.T.; Weber, G. Structure of the plastic-degrading Ideonella sakaiensis MHETase bound to a substrate. *Nat. Commun.* **2019**, *10*, 1–10. [CrossRef]
35. Marshall, I.; Todd, A. The thermal degradation of polyethylene terephthalate. *Trans. Faraday Soc.* **1953**, *49*, 67–78. [CrossRef]
36. Tokiwa, Y.; Calabia, B.P.; Ugwu, C.U.; Aiba, S. Biodegradability of plastics. *Int. J. Mol. Sci.* **2009**, *10*, 3722–3742. [CrossRef]

37. Austin, H.P.; Allen, M.D.; Donohoe, B.S.; Rorrer, N.A.; Kearns, F.L.; Silveira, R.L.; Pollard, B.C.; Dominick, G.; Duman, R.; El Omari, K. Characterization and engineering of a plastic-degrading aromatic polyesterase. *Proc. Natl. Acad. Sci. USA* **2018**, *115*, E4350–E4357. [CrossRef]

38. Baldwin, R.L. How Hofmeister ion interactions affect protein stability. *Biophys. J.* **1996**, *71*, 2056–2063. [CrossRef]

39. Joo, S.; Cho, I.J.; Seo, H.; Son, H.F.; Sagong, H.-Y.; Shin, T.J.; Choi, S.Y.; Lee, S.Y.; Kim, K.-J. Structural insight into molecular mechanism of poly (ethylene terephthalate) degradation. *Nat. Commun.* **2018**, *9*, 1–12. [CrossRef] [PubMed]

40. Martínez, L.; Andrade, R.; Birgin, E.G.; Martínez, J.M. PACKMOL: A package for building initial configurations for molecular dynamics simulations. *J. Comput. Chem.* **2009**, *30*, 2157–2164. [CrossRef]

41. Dickson, C.J.; Madej, B.D.; Skjevik, Å.A.; Betz, R.M.; Teigen, K.; Gould, I.R.; Walker, R.C. Lipid14: The amber lipid force field. *J. Chem. Theory Comput.* **2014**, *10*, 865–879. [CrossRef] [PubMed]

42. Sprenger, K.G.; Jaeger, V.W.; Pfaendtner, J. The General AMBER Force Field (GAFF) Can Accurately Predict Thermodynamic and Transport Properties of Many Ionic Liquids. *J. Phys. Chem. B* **2015**, *119*, 5882–5895.

43. D'Oronzo, E.; Secundo, F.; Minofar, B.; Kulik, N.; Pometun, A.A.; Tishkov, V.I. Activation/Inactivation Role of Ionic Liquids on Formate Dehydrogenase from Pseudomonas sp 101 and Its Mutated Thermostable Form. *Chemcatchem* **2018**, *10*, 3247–3259.

44. Shaposhnikova, A.; Kuty, M.; Chaloupkova, R.; Damborsky, J.; Smatanova, I.K.; Minofar, B.; Prudnikova, T. Stabilization of Haloalkane Dehalogenase Structure by Interfacial Interaction with Ionic Liquids. *Crystals* **2021**, *11*, 1052. [CrossRef]

45. Ryckaert, J.-P.; Ciccotti, G.; Berendsen, H.J. Numerical integration of the cartesian equations of motion of a system with constraints: Molecular dynamics of n-alkanes. *J. Comput. Phys.* **1977**, *23*, 327–341. [CrossRef]

46. Essmann, U.; Perera, L.; Berkowitz, M.L.; Darden, T.; Lee, H.; Pedersen, L.G. A smooth particle mesh Ewald method. *J. Chem. Phys.* **1995**, *103*, 8577–8593. [CrossRef]

47. Hess, B. P-LINCS: A parallel linear constraint solver for molecular simulation. *J. Chem. Theory Comput.* **2008**, *4*, 116–122. [CrossRef]

48. Berendsen, H.J.C.; Vanderspoel, D.; Vandrunen, R. GROMACS—A message-passing parallel molecular-dynamics implementation. *Comput. Phys. Commun.* **1995**, *91*, 43–56.

49. Pronk, S.; Pall, S.; Schulz, R.; Larsson, P.; Bjelkmar, P.; Apostolov, R.; Shirts, M.R.; Smith, J.C.; Kasson, P.M.; van der Spoel, D.; et al. GROMACS 4.5: A high-throughput and highly parallel open source molecular simulation toolkit. *Bioinformatics* **2013**, *29*, 845–854. [CrossRef]

50. Van der Spoel, D.; Lindahl, E.; Hess, B.; Groenhof, G.; Mark, A.E.; Berendsen, H.J.C. GROMACS: Fast, flexible, and free. *J. Comput. Chem.* **2005**, *26*, 1701–1718. [CrossRef]

51. Humphrey, W.; Dalke, A.; Schulten, K. VMD: Visual molecular dynamics. *J. Mol. Graph.* **1996**, *14*, 33–38. [CrossRef]

CHAPTER 5

Conclusions

The presence of additional components, such as salts and co-solvents, might affect the interaction of water molecules with biomolecules in the solution. Indeed, salts and co-solvents can alter the structure stability, conformational flexibility, and functionality of biomolecules either directly (by binding to proteins) or indirectly (by modifying the water network). During my Ph.D., molecular dynamics (MD) simulations were used to reveal the influence of salts and co-solvent on the structural properties of biomolecules (DNA and enzymes) and provide more details about the solvation, interaction, stability, and flexibility of them in the solution. Because of this effort, two articles reveal the influence of imidazolium-based ionic liquids on the structural properties of DNA, and one article investigates the effect of aqueous solutions of selected ILs on an enzyme, which are included in this thesis. In addition, two articles on the influence of the Hofmeister series on two different enzymes were investigated. Furthermore, one article regarding the investigation of the effect of hydrated deep eutectic solvents on the structural properties of DNA is going to be submitted.

In the first work, MD simulations were implemented for deepening insight into the sequence and structural specificity of the binding interactions between imidazolium-based ILs and both the phosphate groups and nucleobases in the minor and major grooves of double-strand DNA. A 30-base pair double-strand DNA structure was chosen as a model of natural DNA. The simulation results showed the predominance of a groove binding mechanism between ILs cations and DNA, with a preferential interaction between guanine residues and the shorter alkyl-chain length of the imidazolium cation. Furthermore, according to the MD simulation analysis, a combination of electrostatic and hydrophobic interactions derived the shorter alkyl-chain length of imidazolium cations to have a stronger interaction with the DNA major groove.

In the second study, MD simulations were used to report on interactions between imidazolium-based ILs and a synthetic DNA oligonucleotide made entirely of T/A bases (7(TA)) to understand the effects of ILs on a model DNA duplex. MD radial distribution functions revealed that hydrophobic interactions became more prominent as IL concentrations increased. Alkyl chain alignment with DNA and IL-IL interactions also varied with IL. Collectively, our data showed that, at low IL concentrations, IL was primarily bound to the DNA minor groove, and with increased IL concentration, the phosphate regions and major groove binding sites were also important contributors to the complete set of IL-DNA duplex interactions.

Another study used MD simulations to investigate the effect of aqueous solutions of selected ILs on Ideonella sakaiensis PETase with bis(2-hydroxyethyl) terephthalate (BHET) substrate to identify the possible effect of ILs on the structure and dynamics of enzymatic Polyethylene Terephthalate (PET) hydrolysis. The use of specific ILs, which are known to partially dissolve PET, has the potential to improve the enzymatic hydrolyses of PET. The aqueous solution of cholinium phosphate was found to have the smallest effect on the structure of PETase, and its interaction with (BHET) as a substrate was comparable to that with pure water. As a result, cholinium phosphate was identified as a potential co-solvent candidate for studying the enzymatic hydrolysis of PET.

It must be mentioned that all MD simulations were implemented by the Gromacs program package. Also, Visual Molecular Dynamics (VMD) was used for visualizations and the preparation of snapshots. After the simulation, some strategies, including the radial distribution function (RDF) and root mean square deviation (RMSD), were applied to extract relevant information.

PERSONAL INFORMATION:

Name: Fatemeh Fadaei	**Sex**: Female
Date of birth: 21.Sep.1990	**Phone**: +420723966972
E-mail:fadaef00@prf.jcu.cz	**Marital status:** Married
Fadaeifatemeh1@gmail.com	

EDUCATION:

2020-Present   PhD student in Biophysics (University of South Bohemia, Czech Republic)
Thesis Title: Biomolecular Simulations in Non-aqueous Media.

2012-2014   M.Sc in Analytical Chemistry (University of Mazandaran, Iran) GPA: 16.68/20
Thesis Title: Quantitative Structure Activity Relationship Prediction of Oral Bioavailability.

2009-2012   B.Sc in Applied Chemistry (Islamic Azad University, Iran) GPA: 17.11/20

SKILLS:

- ❖ Linux
- ❖ GROMACS
- ❖ Visual Molecular Dynamics
- ❖ Origin
- ❖ IBM SPSS Statistics

- ❖ Python
- ❖ HyperChem
- ❖ MOPACK
- ❖ STATISCA
- ❖ Minitab

PAPER PUBLICATIONS:

❖ Fatemi, M.H. and Fadaei, F., 2014. Quantitative Structure Activity Relationship Prediction of Oral Bioavailabilies Using Support Vector Machine. *Journal of the Korean Chemical Society*, *58*(6), pp.543-552.

❖ Fadaei, F., Tortora, M., Gessini, A., Masciovecchio, C., Catalini, S., Vigna, J., Mancini, I., Mele, A., Vacek, J., Reha, D. and Minofar, B., 2022. Structural specificity of groove binding mechanism between imidazolium-based ionic liquids and DNA revealed by synchrotron-UV Resonance Raman spectroscopy and molecular dynamics simulations. *Journal of Molecular Liquids*, *347*, p.118350.

❖ Fadaei, F., Seifert, M., Raymond, J.R., Řeha, D., Kulik, N., Minofar, B. and Heitz, M.P., 2021. Interactions between a dsDNA Oligonucleotide and Imidazolium Chloride Ionic Liquids: Effect of Alkyl Chain Length, Part I. *Molecules*, *27*(1), p.116.

❖ Zara, Z., Mishra, D., Pandey, S.K., Csefalvay, E., Fadaei, F., Minofar, B. and Řeha, D., 2021. Surface Interaction of Ionic Liquids: Stabilization of Polyethylene Terephthalate-Degrading Enzymes in Solution. *Molecules*, *27*(1), p.119.

❖ Dušeková, E., Berta, M., Sedláková, D., Řeha, D., Dzurillová, V., Shaposhnikova, A., Fadaei, F., Tomková, M., Minofar, B. and Sedlák, E., 2022. Specific anion effect on properties of HRV 3C protease. *Biophysical Chemistry*, p.106825.

❖ Dušeková, E., Garajová, K., Yavaşer, R., Tomková, M., Sedláková, D., Dzurillová, V., Kulik, N., Fadaei, F., Shaposhnikova, A., Minofar, B. and Sedlák, E., 2022. Modulation of global stability, ligand binding and catalytic properties of trypsin by anions. *Biophysical Chemistry*, *288*, p.106856.